1-1-2016

Electronic Transport In Two-Dimensional Systems In The Quantum Hall Regime

Vinicio Tarquini
Wayne State University,

ELECTRONIC TRANSPORT IN TWO-DIMENSIONAL SYSTEMS IN THE QUANTUM HALL REGIME

by

VINICIO TARQUINI

DISSERTATION

Submitted to the Graduate School

of Wayne State University

Detroit, Michigan

in partial fulfillment of the requirements

for the degree of

DOCTOR OF PHILOSOPHY

2016

MAJOR: Physics

Approved By:

_____

Advisor

_____

_____

_____

DEDICATION

I dedicate my dissertation work to my family and friends. A special feeling of gratitude to my loving parents and parents-in-law, for their words of encouragement and push for tenacity that still ring in my ears. My wife Elisa has been a constant source of support and encouragement during the challenges of graduate school and life. I am truly thankful for having you and Francesco in my life. I also dedicate this dissertation to my group mates who have supported me throughout the process. I will always appreciate all they have done.

ACKNOWLEDGEMENTS

I wish to thank my committee members who were more than generous with their expertise and precious time. A special thanks to Dr. Jian Huang, my committee chairman and advisor for his countless hours of reflecting, reading, encouraging, and most of all patience throughout the entire process. Thank you Dr. Boris Nadgorny, Dr. Zhi-Feng Huang, and Dr. Mark Cheng for agreeing to serve on my committee. Special thanks goes to the members of the Quantum Transport Group, Talbot Knighton, Wu Zhe, and Parisa Bashiri for their continued support and discussion.

Finally I would like to acknowledge the support of this work from NSF under No. DMR-1105183 and No. DMR-1410302. The work at Princeton was partially funded by the Gordon and Betty Moore Foundation through Grant GBMF2719, and by the National Science Foundation MRSEC-DMR-0819860 at the Princeton Center for Complex Materials.

TABLE OF CONTENTS

LIST OF FIGURES

CHAPTER 1 INTRODUCTION AND MOTIVATIONS

The Fermi-Liquid theory describes the metallic electron states with only weak electron-electron interaction limited by the kinetic energy and the Pauli Principle. On the other hand, it is well known that non-Fermi-Liquid ground states, such as the superconducting state and the Anderson insulator, exist as a result of substantial interaction between charges and interaction with disorder. But what happens to the ground state when dominating Coulomb interaction is present? The Fermi-Liquid theory is expected to breakdown and new physics manifests. In this work I will describe our approach to explore this new area of physics where exotic insulating states such as quantum Hall states and topological insulating states manifest themselves. The theoretical challenges to quantitatively describe multi-body phenomena have pushed the experimental research, and recent breakthroughs in the fabrication of dilute high mobility systems have made possible to explore widen our horizons and search for new fascinating phenomena. We focus on the fabrication of the devices that will help us to realize ideal systems for probing interaction-driven phenomena.

1.1 Motivations

The focus of this work will be the study of two-dimensional hole (2DH) systems confined in GaAs quantum wells (QWs) is of fundamental importance for the investigation of strongly correlated phenomena [1–3] as well as for spintronics [4] and device applications.

The choice of investigating holes systems is dictated by the fact that 2DH systems are characterized by a much larger effective mass (m^*) than electrons which leads to an enhanced interaction effect as shown through the interaction parameter $r_s = (m^* e^2)/(4\pi\hbar^2\epsilon)(p\pi)^{-1/2}$, that is the ratio of Coulomb and Fermi energy [3]. Determining the exact value of m^* is always been a challenge especially in the diluted regime, where strongly-correlated regime where

splitting and mixing of the bands and interaction effects yield a complex band structure with non-parabolic dispersion [5]. Furthermore the shape and relative location of the sub-bands is very sensitive to the characteristics of the individual system and confinement technique, such as the width, depth, lattice direction and symmetry of the quantum well. To the investigation of correlation effects it is necessary to explore more low-density systems. For many years, this was impossible: the level of disorder was too high and the deriving localization effects where dominating the electron-electron interactions, so that only the high density regime was available for investigation [6, 7]. Recent breakthroughs in semiconductor technology and sample fabrication have made it possible to decrease the disorder enough to allow us to enter the low-density regime 4.3×10^{10} cm^{-2} $\leq$ p $\leq$$4.8\times10^{10}$ cm^{-2} and realize a high purity 2DH system maintaining a very high carrier mobility, $\mu \sim 2\times10^{6}$ cm^2/(V·s). In this conditions we can utilize the Shubnikov-de Haas (SdH) oscillations to gain insights on the m^* and the band structure of the valence band populated by the 2DHS. The results complement previous studies of low density m^* measured via cyclotron resonance method in magnetic fields around $\sim$ 0.5T [8].

With a clear picture on the band structure of our samples we can approach the study of more fundamental phenomena. The integer and the fractional quantum Hall effects (IQHE [6] and FQHE [7]) are essential to the exploration of quantum matters characterized by topological phases. A quantum Hall (QH) system manifest zero magnetoresistance, due to one-dimensional (1D) chiral edge channels maintained dissipationless via the broken time reversal symmetry, and quantized Hall resistance $\nu h/e^2$ with ν being the topological invariant (or Chern number) [9]. The 1-1 correspondence between the conducting gapless edge channels to the gapped incompressible bulk states is a defining character of a topological insulator (TI).

Understanding this correspondence in real systems, especially the origin of its robustness (in terms of the limit of breakdown), is important both fundamentally and practically (i.e. in relation to spintronics [4]). However, the breakdown mechanism, especially in light of the edge-bulk correlation, is still an open question.

Experimental probes to the breakdowns usually rely on the onset of the non-zero magnetoresistance (MR) and distorted Hall resistance [10], measured via electrical probes located on the same physical edge, when a Hall bar system is subjected to sufficiently large bias. However, the results are inconsistent with the theoretical models based on mixing of the Landau levels (LLs), i.e. through Umklapp scatterings either via phonons or impurities [11–18]. These criteria may not be rigorous since the complete picture requires also the dynamical information of the bulk. The edge dynamics, including the important edge reconstruction [19, 20], has been extensively studied through experiments on edge-edge equilibration [21, 22], scattering in quantum point contact [23], and edge channel reflection [24, 25]. On the other hand, the results on the bulk dynamics, such as those obtained with the Corbino geometries [26, 27], are still insufficient addressing the dynamical correspondence [28, 29].

We propose an ultrahigh quality 2D holes systems patterned into an anti-Hall bar geometry where, analogous to the Corbino geometry, an extra set of edge, referred to as inner edge, is formed. In this way we are capable to probe the transport across the sample simultaneously observing the bulk and edge dynamics.

Alongside to these projects on GaAs-based devices, we have analyzed the quantum transport of the 2D material par excellence, graphene and prepared the ground for its application as a ultra-high gain and quantum efficiency hybrid graphene-quantum dots phototransistors.

CHAPTER 2 THEORETICAL BACKGROUND

In this chapter I will introduce the main theoretical aspects on which we base our research, showing how important and critical is to reach the right experimental conditions to observe these kind of phenomena.

2.1 Electrons in Solids

We know that in solids, to a good approximation, lattice and electronic degrees of freedom are independent or uncoupled. The main reason is the big difference between the masses of ions and electrons, that leads to a different time scale involved in the systems.

$$\tau_{ion} \sim \frac{1}{\omega_D} \gg \tau_{e^-} \sim \frac{\hbar}{\mathcal{E}_F} \tag{2.1}$$

This equation is purely qualitative and considers that in the great part of solids the ions can vibrate with a frequency up to the Debye frequency, $10^{13}s^{-1} \lesssim \omega_D \lesssim 5 \times 10^{13}s^{-1}$, and the energy corresponding to the conducting electrons is the Fermi energy, 1 eV $\lesssim \mathcal{E}_F \lesssim$15 eV [30]. This leads to a characteristic time for the ions $\tau_{ion} \approx 10^{-12}s$ and for the electrons $\tau_{e^-} \approx 10^{-15}s$. So, to a good approximation, the electronic and lattice degrees of freedom are separated and every kind of interaction between the two systems can be treated as a perturbation with a relative magnitude of $\omega_D/\mathcal{E}_F$ (Born-Oppenheimer Approximation). Then we can concentrate on the electronic system. In general, the electrons (ignoring for the moment the electron-electron interaction and the electron-lattice interaction) can be classified in two main classes: core electrons (strongly localized around the atomic core) and valence electrons that interact with the entire environment consisting in the potential $V(\bar{r})$ due to the ions and the core electrons. This potential is periodic so $V(\bar{r} + \bar{R}) = V(\bar{r})$, with

$\bar{R}$ being the lattice constant, I consider only the valence electrons described by plane waves functions and we see the $V(\bar{r})$ as a periodic perturbation we will get that the electrons will be strongly affected by the periodicity of the lattice. From the Block Theorem: the eigenstates of a one-electron Hamiltonian with a periodic potential with periodicity $\bar{R}$ can be chosen to have the form of a plane wave times a function with the same periodicity of the potential. And applying the Born-Von Karman boundary conditions we get:

$$\Psi_{\bar{k}}(\bar{r}) = e^{i\bar{k}\cdot\bar{r}} \sum_{\bar{K}} c_{\bar{k}-\bar{K}} e^{-i\bar{K}\cdot\bar{r}} \tag{2.2}$$

where $\bar{K}$ is the reciprocal lattice vector chosen so that the wave vector $\bar{k}$ lives in the first Brillouin zone. Now the ground state of N "free" electrons[1] can be described as the state in which all the electrons occupy the energies $\mathcal{E}(\bar{k}) = \frac{\hbar^2 k^2}{2m}$ up to the Fermi energy $\mathcal{E}_{\mathcal{F}}$, that can be found equating the total number of energy levels to the total number of electrons:

$$\mathcal{E}_F = \frac{\hbar^2 (3\pi^2 n)^{2/3}}{2m} \tag{2.3}$$

with $n = N/V = 3/(4\pi r_s^3)$ so we can rewrite the Fermi energy as a function of r_s, the radius of a one-electron sphere: INTERACTION PARAMETER R_S:

$$\frac{m^\star e^2}{(4\pi\hbar^2\epsilon)\,(p\pi)^{\frac{1}{2}}} \tag{2.4}$$

$$\mathcal{E}_F \approx \frac{50.1}{(r_s/a_0)^2} eV \tag{2.5}$$

[1] we are considering monoatomic monovalent Bravais lattice, the theory can be easily adapted to more complicated situations.

where $a_0 = \hbar^2/(me^2) = 0.529\ \mathring{A}$ is the Bohr radius. Now for the Block electrons the difference from the free ones is that they are in a periodic potential and $\bar{k}$ must be confined in the Brillouin zone. Analyzing the ground state we could find:

- A certain number of bands are completely filled and the others are empty, so the energy difference between the highest occupied level and the lowest unoccupied one is the *band gap* $\mathcal{E}_g$ and according to the size of this gap we can distinguish between insulators $\mathcal{E}_g \gtrapprox 3\text{eV}$, and semiconductors $\mathcal{E}_g \lesssim 3\text{eV}$. Because the number of levels in a band is equal to the number of primitive cells in the crystal and because each level can accommodate two electrons with opposite spin (fermions), a configuration with a band gap can arise (though it need not) only if the number of electrons per primitive cell is even.
- With partially filled bands the energy of the highest occupied level is the Fermi energy and it lies between the range of one or more bands. For each partially filled band there will be a surface in $\bar{k}$-space separating the occupied from the unoccupied levels. The set of all such surfaces is known as the Fermi surface and it is the generalization of the Fermi sphere for Block electrons.

Now two different situations can be encountered studying the electronic structure of solids: *nearly free electrons* and *tight bounded electrons*. Theoretical and experimental studies of metals of the I, II, III and IV group of the periodic table proved that the electrons behave as moving in an almost constant potential. So to describe them we can use a Sommerfield free electron gas modified by a weak periodic potential. This approach could be useful because the ion-electron interaction is stronger at small separations, but the conduction electrons, because of the Pauli principle, cannot enter the neighborhood of the ions that are already occupied by the core electrons. Also the mobility of the conduction electrons diminishes the

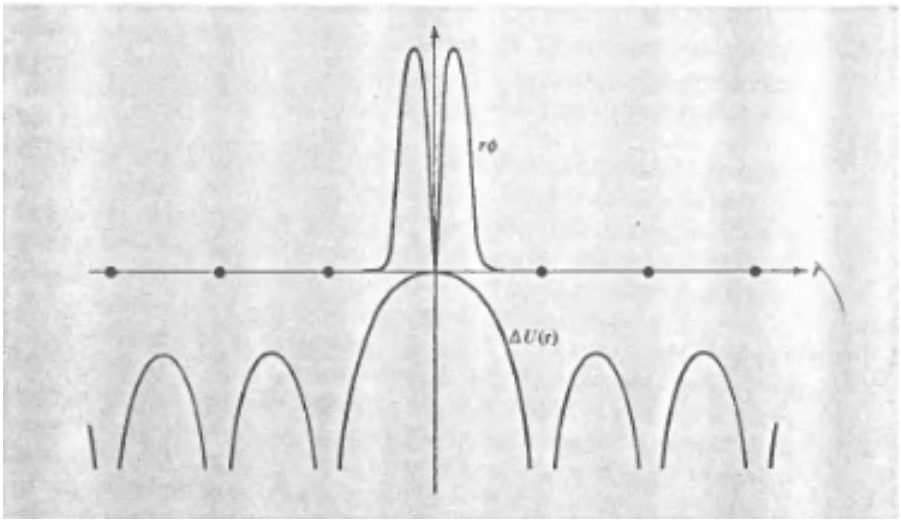

Figure 2.1: The lower curve represents the periodic potential $\Delta U(\bar{r})$, while the $r\phi$ is the atomic wave function. We can see that when $r\phi$ is small $\Delta U(\bar{r})$ is large and viceversa [30].

net potential because they screen the positively charged ions. So if we study the energy bands we find out that the weak periodic potential induces an energy gap at the Bragg planes: as $\bar{k}$ crosses the Bragg plane when the perturbation potential $U_{\bar{k}}$ is not zero we will see a gap $\approx 2U_{\bar{k}}$. The second situation occurs for materials that present an interatomic distance comparable to the spatial extend of the electron wave function. In this case we can use the *Tight-Binding method*: the overlap of the atomic wave functions is enough to require corrections to the isolated atom model, but not so much to change it drastically. This method is usually adopted to describe the energy bands of partially filled d-shells of transition metals atoms and the electronic structure of insulators. So we will assume that the periodic crystal Hamiltonian is approximately the atomic Hamiltonian $\mathcal{H}_{at}$ and that the bounded levels are well localized. In this way when the atomic wave function is large the potential is small and viceversa. This situation makes possible to look at the electron wave function as a superposition of wave function for isolated atoms in each atomic site (Linear Combination of Atomic Orbitals, LCAO).

2.2 Interacting Electrons

Up to this point we described where there is no electron interaction: we worked in the independent electrons approximation. But is this interaction really negligible? The answer is **NO!!**

The Hartree Equations Set describes the interaction between electrons. This Schrödinger Equations are solvable by numerical iteration, but we cannot obtain all the information we want from them. For example we cannot study the particular configuration of the $N-1$ electrons that built the average field in which the single electron lives. Then other features of the electron-electron interaction must be treated separately:

1. *Exchange*
2. *Screening*
3. *Phenomenological way to predict the effects of the electron-electron interactions on the electronic properties of metals*

2.2.1 Exchange: Slater Determinant in the Hartree-Fock Approximation

If we try to solve the Hartree equations with the variational method we will find that the ground state wave function that minimizes $\langle H \rangle_\Psi$ is given by the product of the one-electron levels:

$$\Psi(\bar{r}_1\bar{s}_1, ..., \bar{r}_N\bar{s}_N) = \psi_1(\bar{r}_1\bar{s}_1)\psi_2(\bar{r}_2\bar{s}_2)...\psi_N(\bar{r}_N\bar{s}_N) \tag{2.6}$$

Evidently this result is in strong contrast with the Pauli Principle, which requires the antisymmetry of the N-electron wave function and consequently the sign of Ψ has to change when any two of its arguments are interchanged. Now the easiest way to solve this problem is to replace the trial wave function in Eq. 2.6 by a *Slater determinant* of one-electron wave

functions:

$$\Psi(\bar{r}_1\bar{s}_1, ..., \bar{r}_N\bar{s}_N) = \begin{vmatrix} \psi_1(\bar{r}_1, \bar{s}_1) & \psi_1(\bar{r}_2, \bar{s}_2) & ... & \psi_1(\bar{r}_N, \bar{s}_N) \\ \psi_2(\bar{r}_1, \bar{s}_1) & \psi_2(\bar{r}_2, \bar{s}_2) & ... & \psi_2(\bar{r}_N, \bar{s}_N) \\ ... & ... & ... & ... \\ \psi_N(\bar{r}_1, \bar{s}_1) & \psi_N(\bar{r}_2, \bar{s}_2) & ... & \psi_N(\bar{r}_N, \bar{s}_N) \end{vmatrix} \tag{2.7}$$

After some simplification if we evaluate the $\langle H \rangle_\Psi$ in the new antisymmetric state and we minimize it we get the generalized Hartree equations also known as *Hartree-Fock equations*. The difference between this equation and the simple Hartree equation is the additional negative term on the left side: the *exchange term*. This is a non linear term and introduces great complexity to the problem because it is an integral operator. The only exact solution can be found if we consider a zero or constant periodic potential (Free Electrons Hartree-Fock Theory). Using plane waves as wave functions of the one-electron states we find that the electronic density has to be constant so U^{ele} is uniform. Also in this approximation the ions are represented as a uniform distribution of positive charge with the same density of the negative. So all this leads to $U^{ions} + U^{ele} = 0$. Only the exchange term survives. Now evaluating this integral in terms of its Fourier transform and summing over all the states and take into account that two spin levels are occupied for each $\bar{k}$. Finally we get that the total energy of the system will be:

$$E = N\left[\frac{3}{5}\mathcal{E}_F - \frac{3e^2k_F}{4\pi}\right] \tag{2.8}$$

So writing the result in eV

$$\frac{E}{N} = 13.6 \left[\frac{2.21}{(r_s/a_0)^2} - \frac{0.916}{(r_s/a_0)} \right] eV \tag{2.9}$$

The average change in energy is not negligible in metals.

2.2.2 Screening: Thomas-Fermi Theory

Screening is sn intrinsic property of metallic gasses, and often an important question rises: if we add a charge inside a metallic system, what is the net electrostatic potential felt at some distance r away? To find the charge density in presence of a total potential $\phi = \phi^{ext} + \phi^{ind}$ we will need to solve the one-electron Schrödinger equation:

$$-\frac{\hbar^2}{2m}\nabla^2\psi_i(\bar{r}) - e\phi(\bar{r})\psi_i(\bar{r}) = \mathcal{E}_i\psi_i(\bar{r}) \tag{2.10}$$

Now this procedure can be simplified if we consider the total potential ϕ slowly spatially varying (almost constant at interatomic distance scale), so we can write the energy dispersion relation of an electron at position $\bar{r}$

$$\mathcal{E}(\bar{k}) = \frac{\hbar^2}{2m} - e\phi(\bar{r}) \tag{2.11}$$

Now because the wave packet is typically spread in position at least of order of $1/k_F$ the calculation will be valid only for $\phi(\bar{r})$ varying slowly on the scale of a Fermi wavelength ($2 \leq \lambda_F \leq 10$ $\mathring{A}$ for most of the metals). Once we accept these limitations we can calculate

the electronic number density and therefore the induced density:

$$\rho^{ind}(\bar{r}) = -e[n_0(\mu + e\phi(\bar{r})) - n_0(\mu)] \tag{2.12}$$

so if $\phi(\bar{r})$ is small enough

$$\rho^{ind}(\bar{r}) = -e^2 \frac{\partial n_0}{\partial \mu} \phi(\bar{r}) \tag{2.13}$$

Given that the susceptibility $\chi(\bar{q})$ is the ratio of the induced density and the potential that induces it we can find the Thomas-Fermi dielectric constant:

$$\epsilon(\bar{q}) = 1 + \frac{k_0^2}{q^2} \qquad \text{where} k_0^2 = 4\pi e^2 \frac{\partial n_0}{\partial \mu} \tag{2.14}$$

For example if we have an external potential given by a point charge we will have:

$$\phi(\bar{q}) = \frac{1}{\epsilon(\bar{q})} \phi^{ext}(\bar{q}) = \frac{4\pi Q}{q^2 + k_0^2} \tag{2.15}$$

that has $\phi(\bar{r})$ as Fourier inverse transform:

$$\phi(\bar{r}) = \frac{Q}{r} e^{-k_0 r} \tag{2.16}$$

So we get an exponentially damped Coulomb potential, its strength becomes negligible for distances greater than $1/k_0$: *Coulomb Screening Potential*. We can estimate k_0 if we say

that $\partial n_0/\partial\mu \approx g(\mathcal{E}_F)$:

$$k_0 = 0.815 k_F \left(\frac{r_s}{a_0}\right)^{1/2} = \frac{2.95}{(r_s/a_0)^{1/2}} \mathring{A}^{-1} \tag{2.17}$$

Since (r_s/a_0) is usually between 2 and 6 $k_0 \approx k_F$ the changes in electric charge are screened in a distance similar to the interparticle spacing.

2.2.3 Lindhard Screening

The strength of the Lindhard Theory is that it's very useful to study the $q \approx k_F$. At $T = 0$ the integral is exactly solvable:

$$\chi(\bar{q}) = -e^2 \left(\frac{m k_F}{\hbar^2 \pi^2}\right) \left[\frac{1}{2} + \frac{1-x^2}{4x} \ln\left|\frac{1+x}{1-x}\right|\right], \qquad x = \frac{q}{2k_F} \tag{2.18}$$

We can also show that at very large distances the screened potential goes like:

$$\phi(\bar{r}) \sim \frac{1}{r^3} \cos(2k_F r) \tag{2.19}$$

So we get an oscillatory term with a much more weaker decay respect to the OrnsteinZernike potential of the Thomas-Fermi. Finally if our external charge density as a time dependence $(e^{-i\omega t})$ we will have a dielectric constant q and ω dependent:

$$\epsilon(\bar{q}, \omega) = 1 + \frac{4\pi e^2}{q^2} \int \frac{d\bar{k}}{4\pi^3} \frac{f_{\bar{k}-\frac{1}{2}\bar{q}} - f_{\bar{k}+\frac{1}{2}\bar{q}}}{\hbar^2 \bar{k} \cdot \bar{q}/m + \hbar\omega} \tag{2.20}$$

2.2.4 The Fermi Liquid Theory

Up to this point we treated the electron-electron interaction without substantially change the basic structure of the independent one-electron model. Even in the Hartree-Fock approximation we continue to describe the stationary electronic states by specifying which one-electron levels ψ_i are present in the Slater determinant. This leads us to find a substantially modified energy vs. wave vector relation for the one-electron levels. Landau, developing the Fermi Liquid Theory, tried to answer to the following questions:

- why in spite of the strength of the electron-electron interaction the independent electron approximation is so successful?
- how should we take in to account the consequences of the electron-electron interaction expecially in the calculation of transport properties?

The theory is based on the assumption that the N-electron wave function with the same structure of one for non interacting electrons could no more adequately describe metals with strong interactions like superconductors where pair of electrons are bounded in stationary states by a net attractive interaction, Landau questioned that this kind of approach could fail even for normal metals where the interactions are not so drastically strong [31].

Now we can start to follow the path that Landau proposed. Let's consider a set of non interacting electrons, if we gradually turn on the interaction between electrons, we will have to kinds of effects:

1. The energies of each one-electron level will be modified, Hartree-Fock approximation.
2. The one-electron levels cease to be stationary: the electrons will scatter in and out the levels. This effect was not contemplated in the Hartree-Fock approximation, according

to which one-electron levels are still a valid set of stationary states for the interacting system. Now we have another problem: does this scattering invalidate the independent electrons model? The answer is: it depends on *the rate of scattering*, if the electron-electron relaxation time τ^{ee} is much larger than the other relaxation times, than we can ignore it and use the independent electron model, with the modified dispersion relation.

So now the problem is to estimate the real weight of the electron-electron scattering near the Fermi energy, because only the electrons with a wavelength around the k_F will participate to the transport.

2.2.5 Electron-Electron Scattering near the Fermi energy

The interaction between the electrons is due to the strong screened Coulomb potential that we discussed before, so we should expect a strong scattering. But because of the Pauli Exclusion Principle we assist to a dramatically reduction of the rate. So is the instability introduced by the interaction real? We can answer to this question by appealing to the Fermi Liquid theory. It is well accepted that the normal state of a metal is well described by this theory. In this theory is claimed that the dominant effect of electron interaction is to renormalize the effective mass of the electron and the observed shift is of the order of 10 to 50%. Let's suppose to have Fermi sphere at $T = 0$ plus a single excited electron in a level $\mathcal{E}_1 > \mathcal{E}_F$, now, in order to scatter, this electron must interact with another electron of energy $\mathcal{E}_2 < \mathcal{E}_F$ (only states with energy less than the Fermi energy are occupied). The Pauli principle that the electrons can only scatter in unoccupied levels. If this states have energies of $\mathcal{E}_3$ and $\mathcal{E}_4$ it must be that $\mathcal{E}_3 > \mathcal{E}_F$ and $\mathcal{E}_4 > \mathcal{E}_F$ because all the other states are already occupied, and to conserve the energy we also require that $\mathcal{E}_1 + \mathcal{E}_2 = \mathcal{E}_3 + \mathcal{E}_4$. When $\mathcal{E}_1 = \mathcal{E}_F$ we will must have $\mathcal{E}_2 = \mathcal{E}_3 = \mathcal{E}_4 = \mathcal{E}_F$, so this means that the scattering rate of the

process, which is proportional to the density of scattering states is zero and that the state at the Fermi energy at $T = 0$ is stationary. As soon as $\mathcal{E}_1$ differs from $\mathcal{E}_F$ some phase space becomes available for the process and the other three energies can vary in a shell of thickness $|\mathcal{E}_1 - \mathcal{E}_F|$, but the energy $\mathcal{E}_4$ cannot be chosen freely as a result of the energy conservation.

If we consider the temperature dependence of the scattering rate we will have that *at a temperature T, an electron of energy $\mathcal{E}_1$ near the Fermi surface has a scattering rate $1/\tau$ that depends on its energy and the temperature in the form* [31]:

$$\frac{1}{\tau} = a\left(\mathcal{E}_1 - \mathcal{E}_F\right)^2 + b(k_B T)^2 \tag{2.21}$$

While the electron-phonon scattering goes like T^3 for $T \ll \Theta_D$ and like T for $T \gg \Theta_D$, where Θ_D is between 100 and $1000K$. So the electron lifetime due to the electron-electron scattering can be made as large as we want going to sufficiently low temperatures and considering electrons sufficiently close to the Fermi surface. Because only electrons within $K_B T$ of the Fermi energy affect most of the low-energy metallic properties and we can approximate the scattering rate to:

$$\frac{1}{\tau} \propto (k_B T)^2 \left(\frac{4\pi e^2}{k_0^2}\right)^2 \tag{2.22}$$

and using the definition of the Thomas-Fermi wavelength and some dimensional analysis we get:

$$\frac{1}{\tau} = A\frac{1}{\hbar}\frac{(k_B T)^2}{\mathcal{E}_F} \tag{2.23}$$

At room temperature we get that $(k_B T)^2/\mathcal{E}_F$ is of the order of 10^{-4} eV, that gives a lifetime of the order of 10^{-10} seconds. From the observation of the resistivity of different metals we

find a metallic relaxation time $\tau = m/(\rho n e^2)$ of the order of 10^{-14} seconds. So at room temperature, the electron-electron scattering proceeds at a rate 10^4 time slower than the dominant scattering mechanism [30]. So there is no doubt that the electron-electron scattering is of little consequence in a metal at room temperature and it is for this reason that the non interacting picture works so well and is a good approximation for the normal state properties of a metal at room temperature. It's certainly necessary to go to *very low temperature* (to eliminate thermal scattering by the ionic vibrations) in very pure samples (to eliminate impurity scattering) to see effects of the electron-electron interaction and its characteristic T^2 dependence. But there is a serious gap in this argument: if the electron-electron interactions are strong it is not at all likely that the independent electron approximation will be a good first approximation.

Landau claimed that this approximation was not a good starting point but at the same time he called the elementary excitations in Fermi Liquid theory *quasielectrons*, saying that all the considerations about the electron-electron scattering were still valid if translated in the quasielectrons world, being this quasiparticles fermions obeying to the Pauli principle. For completeness we need to introduce the term "normal Fermi system" that is used to refer to those systems of interacting particles obeying to the Fermi-Dirac statistic. Landau in his paper showed that to all orders of perturbation theory, every interacting Fermi system is normal, but this does not mean that all electronic systems in metals are normal, in fact the superconducting ground state as well as several magnetically ordered ground states cannot be constructed in a perturbative way from the free electron ground state. Now the energy of a particular quasiparticle is the energy to add or subtract that particle from a state in the system. If we consider an interacting system with a distribution function $n^0_{\bar{p}\sigma}$, generally

taken to be the Fermi-Dirac. If we change adiabatically the number of particles, adding or subtracting a particle from the system so slowly so that the system remains in the ground state. This process will change the particle distribution of $\delta n_{\bar{p}\sigma}$ to a one slightly different $n_{\bar{p}\sigma}$ changing also the energy of the system of δE:

$$\delta E = \frac{1}{V}\sum_{\bar{p}\sigma} \mathcal{E}_{p\sigma}\delta n_{\bar{p}\sigma} + \frac{1}{2V^2}\sum_{\bar{p}\sigma,\bar{p}'\sigma'} f_{\bar{p}\sigma,\bar{p}'\sigma'}\delta n_{\bar{p}\sigma}\delta n_{\bar{p}'\sigma'} + ... \tag{2.24}$$

where we defined $f_{\bar{p}\sigma,\bar{p}'\sigma'}$ as the *Landau f-function* that describes the exchange and correlation effects, so how quasiparticles interact, [31]. Now we can can calculate the energy of the quasiparticle ${\mathcal{E}^*}_{\bar{p}\sigma}$ taking the variation of the new ground state with respect of $\delta n_{\bar{p}\sigma}$ and getting:

$${\mathcal{E}^*}_{\bar{p}\sigma} = \mathcal{E}_{\bar{p}\sigma} + \frac{1}{V}\sum_{\bar{p}'\sigma'} f_{\bar{p}\sigma,\bar{p}'\sigma'}\delta n_{\bar{p}'\sigma'} + ... \tag{2.25}$$

Then we see that quasiparticles obey to a Fermi-Dirac distribution function with ${\mathcal{E}^*}_{\bar{p}\sigma} - \mu$ instead of $\mathcal{E}_{\bar{p}} - \mu$. This consideration leads to an effective mass for the quasiparticle m^* defined as

$$\frac{1}{m^*} = \frac{v_F}{p_F} = \frac{1}{p_F}\left(\frac{\partial \mathcal{E}_{\bar{p}\sigma}}{\partial \bar{p}}\right)_{p=p_F} \tag{2.26}$$

Consequently in the vicinity of the Fermi surface, the quasiparticle energy can be consider as linear in the displacement momentum:

$$\mathcal{E}_{\bar{p}\sigma} = \mathcal{E}_F + v_F(p - p_F) \tag{2.27}$$

2.3 Metal Insulator Transition (MIT)

The metal-insulator transition (MIT) has always been one of the central problems in condensed matter physics and there are still questions waiting for an answer. This problem is so important because close to the MIT the physical properties change dramatically with the variation of a control parameter. This parameter can be the carrier concentration, the temperature or the external magnetic field. A metal-insulator transition can be triggered by: electron-electron interactions (*Mott transition*), disorder (*Anderson Localization*) and frustration (*Glassy Freezing*). To study experimentally this phase transition we need to use materials with a very dilute carriers density that is also easy to manipulate, so very interesting materials are those that are intrinsically insulating but that can easily accept charge carriers. Examples of these systems are the MOSFETs (metal-oxide-semiconductor field-effect transistors) or even better the high purity HIGFETs[2] (heterojunction-insulator-gate field-effect-transistors). The main reason the MIT is so difficult to understand is that the metal and the insulator state are fundamentally different: the first one is characterized by fermionic quasiparticles[3] that extend all over the system, instead the second state is characterized by collective bosonic excitations like phonons and spin waves. So as all the phase transitions in the intermediate regime of the MIT both types of excitation coexist.

Nowadays using theoretical methods we can determine very accurately the electronic band structure of a material, so we can find all the electronic levels that are accessible to the valence electrons and populate them according to the Pauli principle [32]. So, as we already discussed, if the highest occupied electronic state (Fermi energy) is within a band gap then

[2] Devices that we are using in our current experiment

[3] This fermionic quasiparticle are the electrons excited above the Fermi sea discussed in the Fermi Liquid Theary

the material is an insulator: it takes a finite energy to excite the electron to the lowest accessible state in order to carry electrical current, in contrast if the bands are partially filled we can expect a metal.

We already studied the consequences of the electron-electron interaction and we found that we need to go to very low temperature and very diluted system to experience its effect. But in materials close to the MIT the Fermi energy is small and the restriction brought by the exclusion principle becomes weaker. This happens for example in:

- Narrow band materials such as transition-metal oxide V_2O_3
- Doped semiconductors such as Si:P or diluted two-dimensional electron gases
- Doped magnetic (Mott) insulators such as the famous high-T_c cuprate $La_{2-x}2Sr_xCuO_4$ [32]

The common feature in all these cases is that the interaction potential (electron-electron or electron-impurity) becomes comparable to the Fermi energy and the electrons can suddenly become localized. Now even if the band structure does not present a gap the material ceased to conduct because the electron are bounded to very specific positions.

2.3.1 Mott Transition

From the band theory we have that if a crystal has an odd number of electrons per unit cell, it will be a metal. But many materials with this characteristic have been experimentally proved to be insulating. These kinds of materials, for example transition metal oxides, often present antiferromagnetic ground states. Slater tried to explain this phenomenon as a formation of a spin density wave, but his prediction of the critical temperature for the phase transition failed. Mott [33] in 1949 and Hubbard in 1963 [34] explained the what leads to the transition: it's the strong Coulomb repulsion between electrons occupying the same orbital. In the Hubbard Model the vast set of bound and continuum electron levels of each ion is

reduced to a single localized orbital level. The states of the system is specified by giving the four possible configuration for each ion: empty, contains an electron with either spin up or down or two electrons with opposite spin. The Hamiltonian for the Hubbard Model contains a term diagonal in the states that is just a positive energy U that describes the on-site Coulomb repulsion, a term off-diagonal that describes the inter-orbital hybridization without change of spin and a term corresponding to the site energy, also $c_{j\sigma}$ and $c^{\dagger}_{j\sigma}$ are respectively the destruction and creation operators, they destruct or create an electron of spin σ in the $j-th$ orbital:

$$H_{Hub} = -\sum_{\langle i,j\rangle,\sigma}\left(tc^{\dagger}_{i\sigma}c_{j\sigma} + h.c.\right) + \sum_{j\sigma}\epsilon_j c^{\dagger}_{j\sigma}c_{j\sigma} + U\sum_{j} c^{\dagger}_{j\uparrow}c_{j\uparrow}c^{\dagger}_{j\downarrow}c_{j\downarrow} \tag{2.28}$$

Ones we have the Hamiltonian is pretty straight forward to proceed to a qualitative analysis of the Mott transition.

Let's start with the assumption that the lattice has an integer filling per unit cell, because of the Coulomb potential the electrons can jump from an orbital to the other only if they have a kinetic energy high enough to overcome the coulomb barrier. So if $U \gg t \sim \mathcal{E}_K$ we will see an insulating behaviour: a band gap ($\mathcal{E}_g \approx U - 2zt$, where z is the lattice coordination number) will open leading to the Mott insulator [32]. So in each site we will have a spin 1/2 magnetic moment, the interact with each other through superexchange interactions[4] of the order of $J \sim U/t^2_{ij}$ leading to a magnetic ordering (usually antiferromagnetic) temperature $T_j \sim J$ [35]. As we can see the insulating behaviour is not caused by magnetic order, in fact

[4] Superexchange is a strong magnetic coupling, usually antiferromagnetic, between two next-to-nearest neighbor cations through a non-magnetic anion. In this way, it differs from direct exchange in which there is coupling between nearest neighbor cations not involving an intermediary anion.

the band gap arose from Coulomb repulsive potential. The experiments prove this hypothesi: has been observed that the critical temperature for the MIT is:

$$T_{Mott} \sim \mathcal{E}_g \sim 10^3 - 10^4 K \gg T_j \sim 100 - 300K \tag{2.29}$$

There is a very subtle peculiarity of this kind of transition: the gap is due mainly to the nearest-neighbor interactions, it measures how easy is for an electron to jump from one site to the other; so a Mott transition can take place in doped semiconductors, that can be viewed as very disordered Mott insulators [36].

2.3.2 Wigner Crystal

A very important question is: *what happens when the carrier density is so low that the Fermi wavelength is much bigger than the lattice spacing?*

In the 1934 Eugene Wigner [37] tried to answer to this question. His crucial observation was that in a low density electron gas in a uniform ion background the electrons should form an ordered array. We already introduced r_s in Eq. 2.5 and we can easily see that, by definition, if the density becomes very low, $n_e \to 0$, the region available to each electron becomes very big $r_s \to \infty$. In this limit the kinetic energy energy of the electrons is proportional to the inverse square of r_s, $\mathcal{E}_k \propto 1/r_s^2$, while the Coulomb repulsion is proportional to the inverse of r_s, $\mathcal{E}_{Coul} \propto 1/r_s$; so there will be a critical density for which the energy of the ground state will be dominated by the Coulomb interactions, $\mathcal{E}_{Coul} \gg \mathcal{E}_F$. Inside the Coulomb potential the electron will organize in an ordered array called the Wigner Crystal lattice to minimize the repulsion. In this situation the electron is not confined by the ionic potential but by the repulsion from other electrons. The three dimensional Wigner crystal is a b.c.c. (base

centered cubic) and in 2 dimensions is a triangular. Fig. 2.2[5]. The same Coulomb repulsion prevents double occupations so we will get a magnetic insulator that looks very similar to a Mott insulator. From relatively modern studies we find that to get an antiferromagnetic

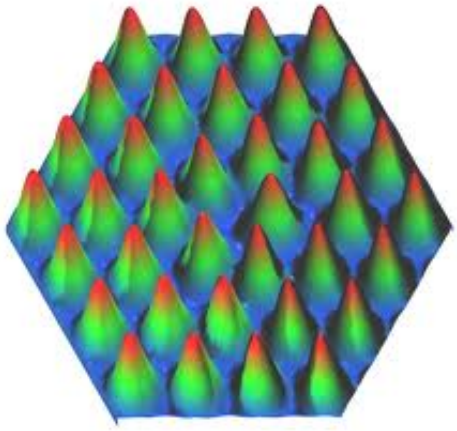

Figure 2.2: A two dimensional Wigner crystal presenting a triangular lattice [38].

stable b.c.c. we need $r_s > 93$ [39] and we will see a transition to a ferromagnet for $r_s \approx 65$ [40]. Now to have an idea of the energy associated to a Wigner solid we can use the Wigner-Seitz cell method [41]: we divide the crystal into Wigner-Seitz cells each containing an electron in its center with a uniform ion background, because each cell is neutral the interaction between the single cells is an higher order correction. After a careful calculation of the electron-background energy, the direct Coulomb interaction energy and the correlation energy we get in perturbation theory that the cohesive energy is of the order of $1eV$. So at sufficient low densities an order electron lattice minimizes the energy of the electron gas.

2.3.3 Anderson Localization

For ordinary metals small concentrations of impurities and defects just produce a random scattering that, because the kinetic energy of the electrons is so large, can be treated as a

[5] Figure from: http://www.tcm.phy.cam.ac.uk/ mdt26/qmc-projects2/wigner-crystals.html

small perturbation. So the Drude theory applies to the transport giving:

$$\sigma = \frac{ne^2\tau_{tra}}{m} \tag{2.30}$$

where n is the carrier concentration, e the electron charge, m is the mass and τ_{tra}^{-1} is the total scattering rate in the transport. Inside τ_{tra} there are contributions from all different kinds of scattering such as impurity scattering (τ_{imp}^{-1}), electron-electron scattering ($\tau_{ee}^{-1}(T)$), electron-phonon scattering ($\tau_{ep}^{-1}(T)$) and etc... But what happens when the disorder grows and the density decreases?

In the 1958 Philip Anderson proposed electron localization due to disorder as the mechanism leading to a phase transition between extended and localized states with a consequent metal-insulator transition [42].This phenomenon occurs in 1D, 2D and 3D systems, but since is much more likely to find self-crossing trajectories in low dimensional ones this effect manifests itself much stronger in low dimensional systems. He claimed that the wave function of the electron will be profoundly modified if the potential due to the disorder is random and strong enough. In fact when the density of the impurities is very high and the temperature is very low:

- The wavelength of the conduction electrons (λ_F) is of the same order of magnitude of their mean free paths,
- Quantum effects become dominant and electrons behave more as waves,
- The inelastic lifetime of an electron is several orders of magnitude longer than the elastic, so electrons can be scattered by impurities without losing their phase coherence.

This leads to a quantum interference of the conduction electrons at the defects of the system

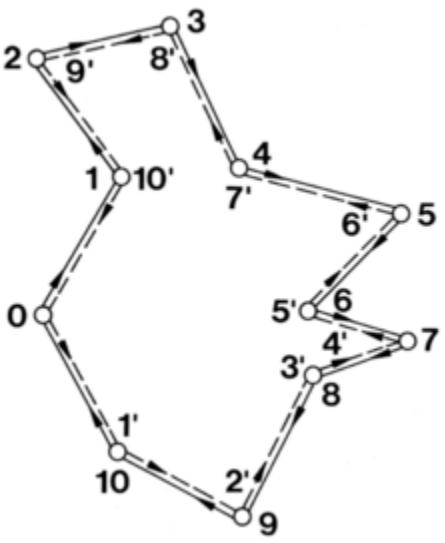

Figure 2.3: Coherent electron scattering from two impurities [43].

(QUIAD): a coherent superposition of the scattered partial electron waves which results in a Back-Scattering of the electron wave and last as long as its coherence is not destroyed[6]. So if we see for example the scattering of an electron from two scattering sites, Fig. 2.3. We have that the intensity of the wave function after the scattering is qualitatively the interference from the incident wave function and its time reversal:

$$|\psi|^2 = |\psi_\alpha|^2 + |\psi_\beta|^2 + \psi_\alpha \psi_\beta^* + \psi_\alpha^* \psi_\beta \tag{2.31}$$

So due to the identical length of the paths we have an increase of the probability that the electron will *wonder around the impurity* in circle decreasing its mobility/increasing the resistivity. An "easy" way to prove experimentally the weak localization is to measure the oscillations of the conductivity while varying a perpendicular magnetic field. The field changes the phase difference between the two partial waves and shows all the spectrum of

[6] This theory is not restricted to electrons only. But could apply to any kind of wave

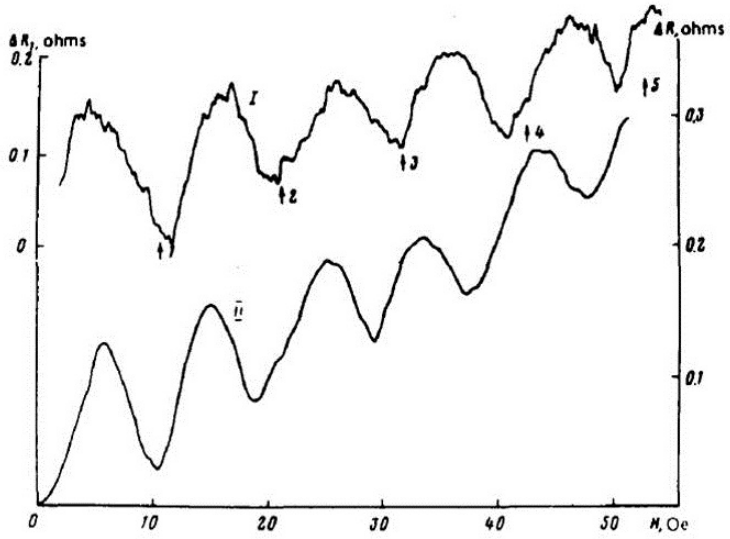

Figure 2.4: Resistance oscillation as a function of the applied magnetic field on a cylindrical Mg-film [44].

the interference, from constructive to destructive [43]. Fig. 2.4 In systems with Spin-Orbit Coupling the spin of the carriers rotates as it goes around a self-interacting path, this leads to a reduction of the probability to return at the origin: weak anti-localization. At very low temperature the magneto-resistance changes sign and reflects the strength of the spin-orbit interaction. A measure of this effect is probably the most sensitive method to measure the spin-orbit scattering.Fig. 2.5 [43] So summarizing while the localization is due to the constructive interference, the anti-localization is an effect of the destructive interference of the back-scattered partial electronic waves. This change of phase is due to the spin-orbit interaction that induces a stochastic rotation of the spin to succession of infinitesimal rotations.

We need to distinguish between the weak localization and the strong one: The Strong Localization Theory predicts that at the strong scattering limit and high degree of disorder the interference can completely localize the electrons so the envelope of the wave packet may

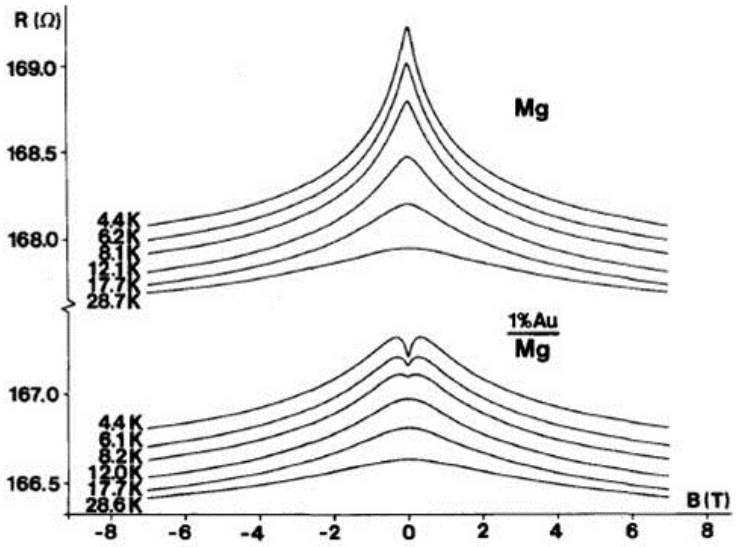

Figure 2.5: Magneto-resistance of a Mg-film, after the deposition of a thin layer of gold the magneto-resistance changes drastically. The gold introduces a non negligible spin-orbit scattering which rotates the spin of the scattered waves, changing the interference from constructive to destructive [43].

exponentially decay [45]:

$$|\psi(\bar{r})| \propto e^{(|\bar{r}-\bar{r}_0|/\xi)} \tag{2.32}$$

where ξ is the localization length. This phenomenon completely stops the waves propagation inside the system leading to a infinite resistivity. So in the presence of sufficiently strong random potential, we can consider the weak localization as a precursor of the strong one.

CHAPTER 3 THE QUANTUM HALL EFFECT

We now introduce the Hall Effect and the Quantum Hall Effect (QHE). They are at the base of our experimental investigation. The QHE in particular is the perfect laboratory to study a great variety of phenomena in both 1D and 2D systems.

3.1 Hall Effect

Let's refresh the basis of the ordinary Hall Effect. The semi-classical theory of conductivity is based on the concept of the *mean free path*, l_0, the electron can travel an average distance l_0 in a time $\tau_0 = l_0/v_F$ before experience scattering and start over its trip with an average velocity zero. Now if we apply a weak electric field $\bar{E}$ the electron will gain a velocity $\Delta\bar{v} = -e\bar{E}\tau_0/m$ between each collision. So we will have a current density $\bar{j} = \sigma_0\bar{E}$ where σ_0 is the conductivity:

$$\sigma_0 = \frac{ne^2\tau_0}{m} \tag{3.1}$$

where n is the number density and the quantum effects from the band structure change enter in m or m^* that now is the effective mass of the electron and in τ_0. Also the Pauli principle restricts the contribution to the current to only the electrons very close to the Fermi surface. When we introduce a magnetic field, in Fig. 3.1, $\bar{B}$ the electron path is curved by the Lorentz force $F_L = -e\bar{v} \times \bar{B}/c$. So we get an additional contribution to the current density:

$$\bar{j} = \sigma_0\bar{E} - \sigma_0\bar{j} \times \frac{\bar{B}}{nec} \tag{3.2}$$

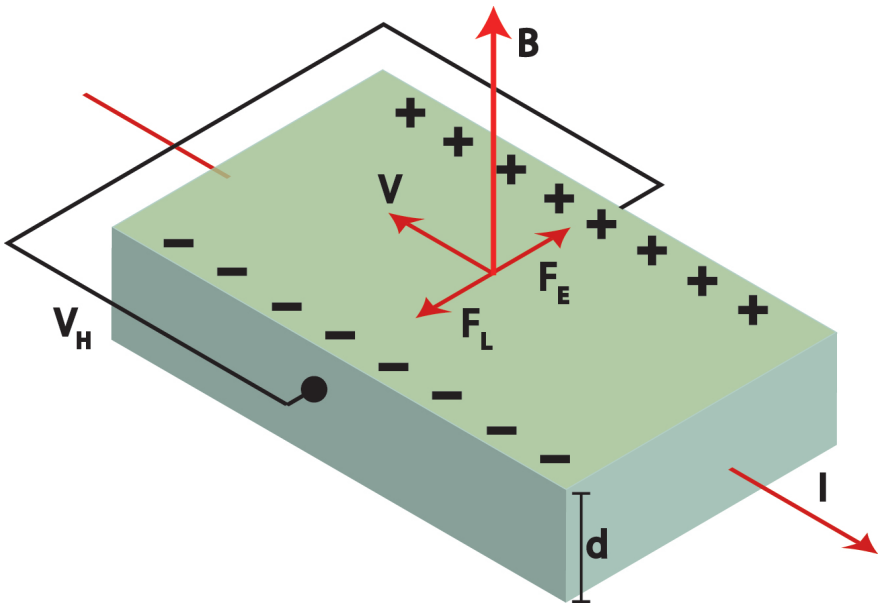

Figure 3.1: Schematic representation of the Hall effect. A current is injected and because of the Lorentz force the electrons' trajectory is deviated. This causes an excess of electrons on one side of the sample inducing a net voltage between the boundaries of the system.

We can work in two dimension if we set the magnetic field in the z-direction ($\bar{B} = B_z$). The resistivity tensor can be easily read from Eq. 3.2 and it is:

$$\bar{\bar{\rho}} = \begin{pmatrix} \rho_0 & B/(nec) \\ -B/(nec) & \rho_0 \end{pmatrix} \tag{3.3}$$

with $\rho_0 = 1/\sigma_0$, and the terms off diagonal ρ_H are independent from the scattering parameters, (in reality they are weakly dependent); now we derive the conductivity tensor $\bar{\bar{\sigma}}$ that is the inverse of the tensor $\bar{\bar{\rho}}$ and we obtain the components:

$$\sigma_{xx} = \frac{\sigma_0}{1 + \omega_C^2 \tau_0^2}, \qquad \sigma_{xy} = \frac{1}{\omega_C \tau_0} \sigma_{xx} + \frac{nec}{B} \tag{3.4}$$

where we defined the cyclotron frequency as $\omega_C = eB/(mc)$ [46]. What we measure are not the resistivity or the conductivity, but the resistance and the conductance. I'll explain the method more in detail during the chapter dedicated to the experimental techniques, here I'm going to touch only the main ideas about the experiment.

A current I is created between the source S and the drain D along a sample of a rectangular shape and a magnetic field B perpendicular to the sample is turned on. We will measure the current, the longitudinal voltage difference V_L between the contacts A and B, and the Hall voltage difference V_H between A and C, furthermore we need to know the distance AB that we call L and the distance AC called W. A big assumption to make is that, if the width of the sample is much smaller than the length $W \ll L$ and the contacts are far form the end, then the current density is uniform and parallel to the long edge of the sample.

We can now compute the longitudinal resistance R_L: since I is fixed $R_L = V_L/I = \rho_{xx}L/W$. Measuring the transverse voltage we can also find the Hall resistance $R_H = V_H/I$. Experimentally we see that the theoretical prediction of an Hall resistance linearly proportional to the magnetic field, $R_H = \rho_H = B/nec$ is confirmed. In the ideal two-dimensional case that we are considering the hall resistivity and the Hall resistance have the same value.

3.2 Quantum Hall Effect

If we go to low temperatures in a two-dimensional metal or semiconductor the Hall effect is also observed, but a series of steps appear in the Hall resistance as a function of magnetic field instead of the monotonic increase. The standard geometry used in the experiments is called Hall bar, and allows the four terminal measurement of the voltage difference between two contacts while driving current between source and drain leads, Fig. 3.2. What is more,

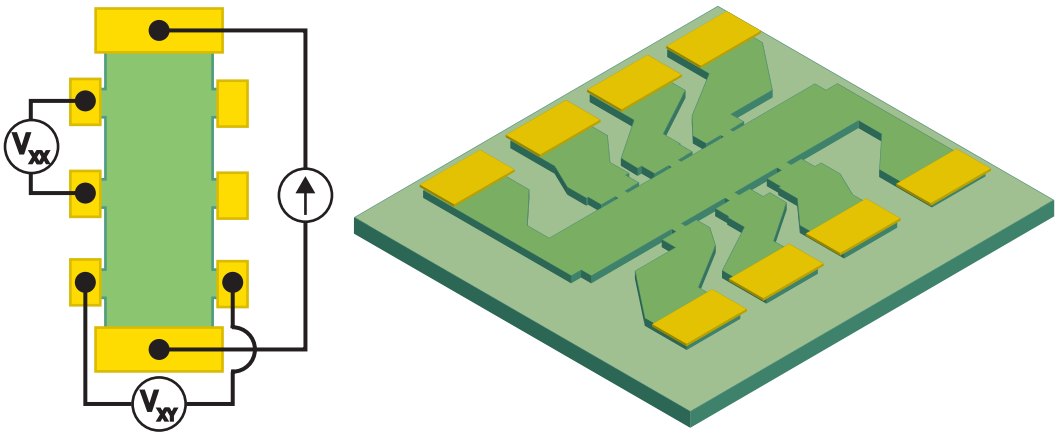

Figure 3.2: Hall bar schematic.

these steps occur at incredibly precise values of resistance which are the same no matter what sample is investigated. The Hall resistance is quantized in units of $h/e^2 \approx 25813\ \Omega$ divided by an integer and the magnetoresistance is zero. This is the *Quantum Hall Effect*. The first to observe Hall resistance plateau were Englert and von Klitzing in 1978 [47]. The idea of analysing the Hall plateaux in terms of the fundamental value h/e^2 emerged immediately. Deeper investigation from Von Klitzing, Dorda and Pepper [6] revealed that the quantization was accurate to a part in 10^5, (The modern accuracy is 8 parts 10^11 [48]). In 1985 Von Klitzing was awarded the Nobel prize for the discovery of the quantum Hall effect. Thanks to the continuous development of the semiconductor growth technology the purity of the two-dimensional systems increased and in 1982 using GaAs/AlGaAs heterostructures Tsui, Stormer and Gossard [7] discovered the Franctional Quantum Hall effect. Tsui, Stormer and Laughlin were awarded the Nobel prize for their discovery in 1999. Figure 3.3 shows the magnetorestance and Hall resistance for both IQHE and FQHE. Let's consider for simplicity independent and spinless electrons in a perpendicular magnetic field, the electron energy levels will be affected by the presence of B. If we consider the two-dimensional and we

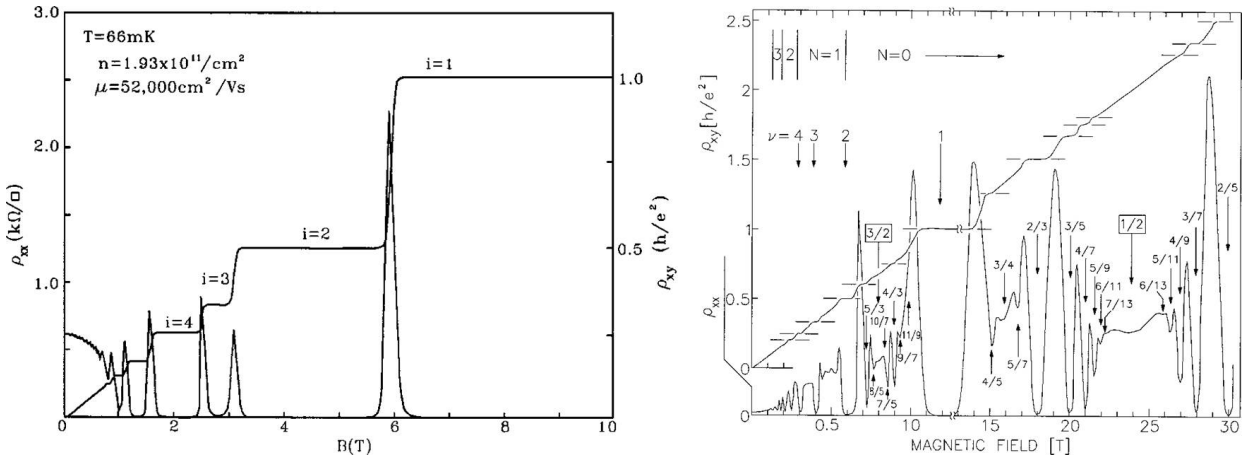

Figure 3.3: Magnitoresistance and Hall resistance are indicated as ρ_{xx} and ρ_{xy}. IQHE on the left [49] and FQHE on the right [50].

calculate the Hamiltonian's eigenvalues we will find that the energies are quantized:

$$\mathcal{E} = (n + \frac{1}{2})\hbar\omega_C \tag{3.5}$$

The cyclotron orbits in the plane perpendicular to the field cause a dramatic change in the x and y dependence of the wave functions of the electrons, the orbits are now localized on a length scale of the order of the cyclotron radius. The energy levels given by Eq. 3.5 are called the *Landau levels*, LLs. Now it is possible to see what happens in the momentum-space when the field is turned on, we can identify each LL with a set of cyclotron orbits that have the same energy [51]. If we compare the energy for free electrons with Eq. 3.5 we can immediately recognise the equation for concentric cylinders parallel to the field:

$$\frac{\hbar^2}{2m}(k_x^2 + k_y^2) = (n + \frac{1}{2})\hbar\omega_C \tag{3.6}$$

So the n-th cylinder that corresponds to the n-th Landau level has an area:

$$A_n = \pi(k_x^2 + k_y^2) = (n + \frac{1}{2})\frac{2\pi eB}{\hbar} \tag{3.7}$$

Because the orbits are quantized we have only certain combinations of k_x, k_y that are accessible, so that each state will collapse on the nearest Landau level, Fig. 3.4. Now we know that the area between successive cylinders is $2\pi eB/\hbar$ and the two-dimensional density of states per unit of area is $(L/2\pi)^2$, so the number of states associated to each LL is:

$$g_n = \left(\frac{L}{2\pi}\right)^2 \left(\frac{2\pi eB}{\hbar}\right) = \frac{eBL^2}{h} \tag{3.8}$$

Very important is that g_n does not depend on n. We calculated that the area of the LLs increases when we increase the field so that the Landau levels will move, Fig. 3.4. When the Fermi energy lies in a gap between LLs electrons can not move to new states and so there is no scattering. Thus the transport is dissipationless and the resistance falls to zero. The number of current carrying states in each LL is eB/h, so when there are ν LLs at energies below the Fermi energy completely filled with $\nu eB/h$ electrons, the Hall resistance is $h/(\nu e^2)$. Where ν is called filling factor. The difference in the QHE is that the Hall resistance can not change from the quantised value for the whole time the Fermi energy is in a gap and so a plateau results. Only when the Fermi energy intersects the LL, the Hall voltage can change and a finite value of magnetoresistance appears. This picture has assumed a fixed Fermi energy, i.e fixed carrier density, and a changing magnetic field. The QHE can also be observed by fixing the magnetic field and varying the carrier density, for

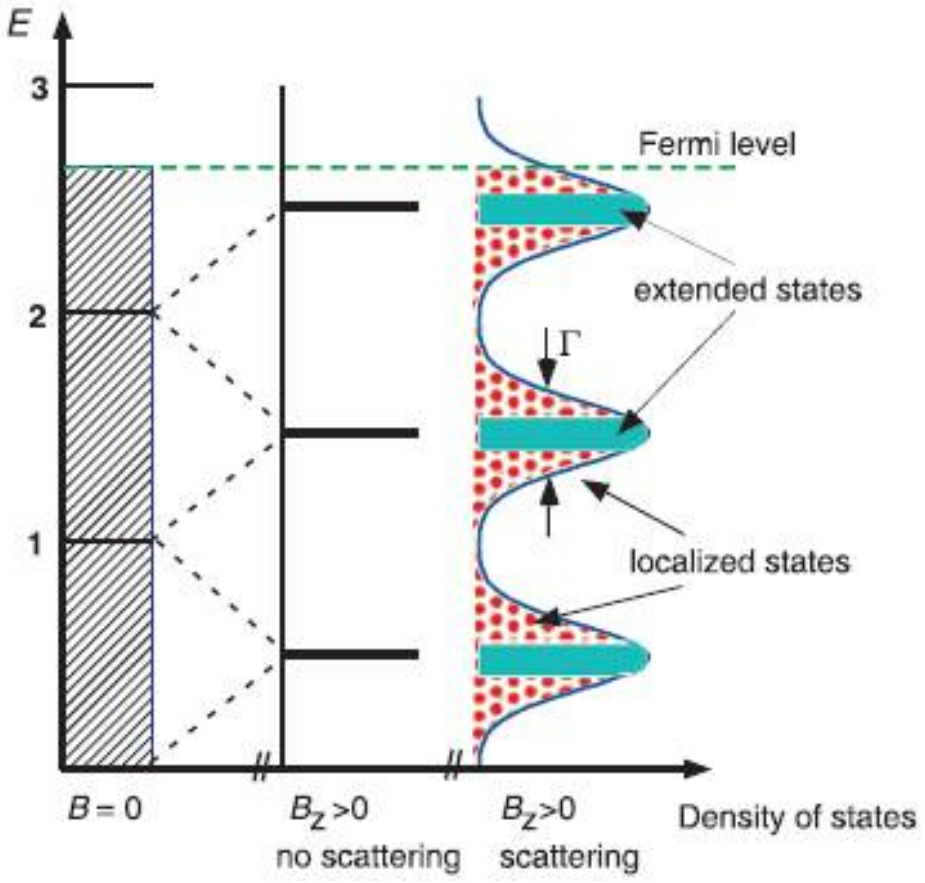

Figure 3.4: The increase of the magnetic field increases the energy of the Landau levels, that shift and pass through the Fermi energy [52].

instance by sweeping a surface gate [46]. In Fig. 3.3 the width of the flat part of the step varies according to the sample temperature, for very good samples at low temperatures the steps are wide and steep. Not only the temperature affects the width and shape of the LL. Even though huge technological progress is been achieved in crystal growth, the lattice is far from being perfect. Defects and impurities are always incorporated in the system and they behave as scattering centre for the electrons. This scattering adds up to the phonon scattering. However, given the temperature at which the QHE is observed, the impurity scattering largely dominates [52]. The impact of the impurity scattering on the LL can be estimated by the parameter $\Gamma = 2.3$ meV $T^{-1}\sqrt{B/\mu}$. For high-quality sample $\Gamma \ll \hbar\omega_c$ [53]. If we consider an impurity characterized by a δ-shaped potential (attractive or repulsive) we will have two kind of states resulting by the interaction of the carrier and the impurity: localized and extended, Fig. 3.4. Only delocalized states can carry current. Increasing the electron density (or equivalently rising the Fermi energy) the electronic states fill gradually. When the E_F is in the mobility gap, where only localized states are available, the population in the extended states does not change giving origin to the Hall plateau and to vanishing longitudinal resistance. Dissipation appears as soon as the extended states are approached by the E_F. From the Hall effect we know that:

$$R_H = R_{xy} = \frac{V_H}{I_x} = \frac{B}{en_s} \tag{3.9}$$

if we apply this formula at low field we can have a very good estimate of the density of the charge carriers in the field and subsequently of the mobility of the 2D system:

$$n_s = -\frac{1}{e}\left(\frac{\partial R_H}{\partial B}\right)^{-1} \qquad \text{and} \qquad \mu = \frac{1}{\rho_{xx}(B=0)en_s} \tag{3.10}$$

Because of the quantization of the Hall resistance we can describe the filling factor as the ratio between the number of electrons and the number of magnetic flux quanta penetrating the sample.

$$\nu = \frac{N}{(\phi/\phi_0)} \tag{3.11}$$

So that each electron is related to ν^{-1} magnetic flux quanta. The degeneracy of each LL is given by $n_L = eB/h$. The electrons only populate the LL with energy lower than E_F so that increasing the B-field increases the degeneracy following a saw-tooth behaviour. If we define the ratio $\nu_L = n_s/n_L$, the E_F is located between between two LL when ν_L is integer. It is evident that $\nu_L = An_s/AeBh^{-1} = N/(\phi/\phi_0) = \nu$ so the plateau appears for integer values of ν. In this situation the electronic system is incompressible: $\partial\mu_{ch}/\partial n_s \to \infty$.

3.3 Buttiker's Picture

In 1988 a cornerstone for the understanding of the electronic transport under quantum Hall effect was published by Mark Buttiker [54]. He formalized a model that explained in terms of reflection and transmission from the contacts the phenomena of absence of backscattering observed by the Nobel prize winner experiment by von Klitzing, Dorda, and Pepper [6]. Explains the QHE in terms of suppression of backscattering in high magnetic fields. Electrons elastically scattered by an impurity can at best be backscattered for a distance determined by the cyclotron orbit. Because of the force deriving from the confining potential the elec-

trons will continue to move along the edge of the system. The conditions for this description to be correct are that: the impurity potential varies smoother over a cyclotron orbit and at the same time rapidly compared to the sample dimensions. The inelastic length should exceed the magnetic length. If these conditions hold, than the electrons will move along the boundaries of the sample without effectively reverse direction. He considered the problem of both ideal and disordered contacts. In case of ideal contacts the edge states are immediately equally populated, whereas disordered contacts lead to an initial non-equilibrium population of the edge states that will be equilibrated after an average of one scattering length away from the contact. A good part of the considerations that I will introduce during the discussion of the our experimental results are based on the understanding of Buttiker's picture and formalism. For a more comprehensive knowledge of the subject I suggest to review the original paper, [54]. Supposing that all the conditions are met, there is at least one phase-

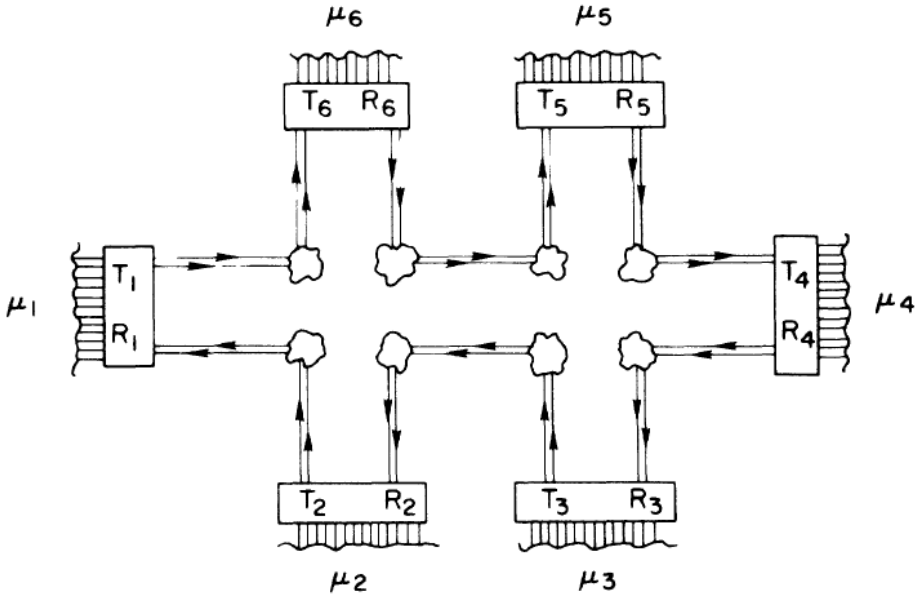

Figure 3.5: Hall bar geometry. The contacts reservoirs are characterized by the chemical potential μ, while the electrons have a probability T to be transmitted into a disordered contact and a probability R to be reflected away from it. Also phase-randomizing reservoir are shown [54].

randomizing reservoir (where the edges equilibrate) along the edge connecting two contacts. With the contacts 1 and 4 as respectively current source and current drain it is possible to demonstrate that the chemical potentials of the phase-randomizing reservoirs are given by μ_A and μ_B on each side of the sample. Once the carriers leave the reservoir there will not be any change in chemical potential. In fact voltage probes are in equilibrium with the sample so that there is no net current flow between the sample and the voltage contact. For example if we consider probe 6 at a chemical potential μ_6. The electronic current from the reservoir μ_A towards the contact 2 is:

$$I = ev\left(\frac{dn}{dE}\right)(\mu_A - \mu_2) \tag{3.12}$$

Now, in 2D systems,

$$\frac{dn}{dE} = \left(\frac{dn}{dk}\right)\left(\frac{dk}{dE}\right) = \left(\frac{1}{2\pi}\right)\left(\frac{1}{\hbar v}\right) \tag{3.13}$$

For this reason we can write

$$I = \frac{e}{h}\Delta\mu \qquad \text{and} \qquad \mathcal{R} = \frac{V_{xy}}{NI} = \left(\frac{\Delta\mu}{e}\right)\left(\frac{h}{Ne\Delta\mu}\right) = \frac{h}{Ne^2} \tag{3.14}$$

Where N is the number of Landau levels below the Fermi energy. So the electron flux toward the voltage contact is $\mathrm{N}(\mu_A - \mu_2)/\mathrm{h}$. Now if R and T are respectively the probability for the electron of being reflected or transmitted at the contact, earlier introduced by Landauer [55], we will have that the fraction of flux flowing into the contact is $T_6(\mu_A - \mu_2)/\mathrm{h}$. At the same time, the voltage lead injects into the sample a flux of electrons $T_6(\mu_6 - \mu_2)/h$. Because the two fluxes have to be equal we will have $\mu_6 = \mu_A$, showing that the chemical potential at the voltage contact is the same of the phase-randomizing reservoir. On the other hand, if we

consider the reflected flux we get that the total flux is $N(\mu_A - \mu_2)$. So, even if the presence of the contact modifies the geometry of the system, the value of the potential is unchanged. For the calculation of the value of μ_A and μ_B we refer to Buttiker original paper [54] where two-terminal conductance is calculated between non-ideal contacts. The result is:

$$\mu_A = \mu_4 + \left(\frac{NT_1}{N^2 - R_1R_4}\right)(\mu_1 - \mu_4) \qquad \text{and} \qquad \mu_B = \mu_4 + \left(\frac{T_1R_4}{N^2 - R_1R_4}\right)(\mu_1 - \mu_4) \quad (3.15)$$

If we use the formalism for which the first subscript represents the current leads and the second the voltage probes, we can write that $\mathcal{R}_{14,23} = \mathcal{R}_{14,65} = 0$ and $\mathcal{R}_{14,26} = \mathcal{R}_{14,35}$ equal the quantized resistance. The quantized resistance can be found by dividing the Hall voltage by the injected current. The total current in Buttiker picture is:

$$I = \left(\frac{e}{h}\right) T_4(\mu_A - \mu_4) = N\left(\frac{T_1T_4}{N^2 - R_1R_4}\right)(\mu_1 - \mu_4) \quad (3.16)$$

So that the quantized resistance is:

$$\mathcal{R}_H = \frac{eU_H}{I} = \frac{\mu_A - \mu_B}{I} = \frac{h}{Ne^2} \quad (3.17)$$

It is worth to remember that we could choose any combination of current and voltage leads and the result would be equivalent. The results just discussed are valid only for samples in which the distance between contacts is greater than the inelastic scattering length.

3.4 Edge channels: Electrostatics and Experiments

After the discovery of the QHE, advances in both experimental technology and material growth has made it possible to study electron transport in systems with different geometries

and reduced dimensionality. In the IQHE the Landau levels intersect the Fermi energy at the boundary of the 2DEG system and give rise to edge channels. Forward and backward moving states are spatially separated by the magnetic field, so that the edge channel can flow without dissipation [54]. Experimental investigation of the population of the edge channels in different geometries have paving the road for a more detailed microscopic theory of the effect. Some of this investigations use a gate voltage to change the carrier concentration in a region of the 2DEG [24, 56]. In this way it is possible to have regions with filling factor different from the bulk, Fig. 3.6. A potential difference develops along either edge across the gate

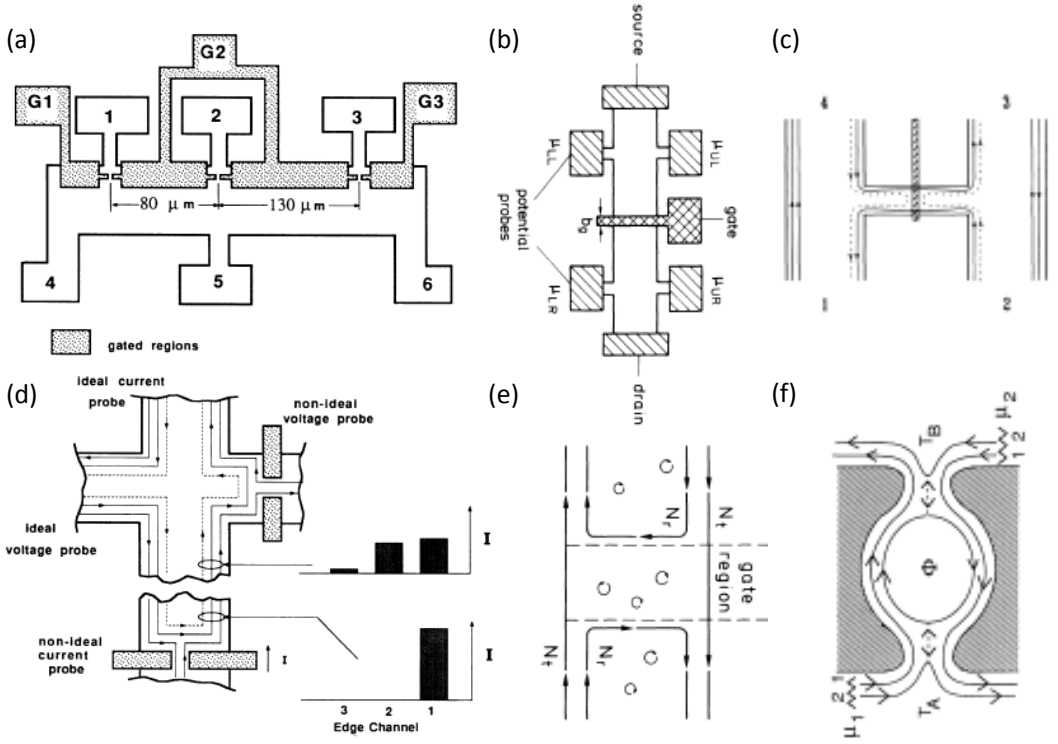

Figure 3.6: Geometries utilized in the different studies, respectively: (a) and (d) [21], (b) and (e) [24], (c) [56], (f) [57] .

section. The resulting resistance across the barrier shows a quantization, which is explainable

in terms of the Landauer formula [58]. This measurements suggest that several Landau levels are occupied and distinguishes dramatically between different multichannel generalizations of the Landauer formula. Another series of experiments explored the equilibration of the current carrying edge channels in the QHE [21, 59]. These investigations use "non-ideal" probes to inject current through a single edge channel and measure the distance necessary for the current to redistribute between all the available channels. The result is that each channel is spatially separated from the others by insulating regions. Current equilibration takes place via electron-scattering processes, the required potential being provided by disorder or phonons [21]. Furthermore, if N channels are available, the innermost spreads more into the sample and is the last to reach equilibrium, Fig. 3.6(d). Also, quantum point contacts, functioning as barriers with controllable transmission, have been used to build a zero-dimensional interferometer between the 1D edge channels [57]. The principal result of the experiment is that very pronounced discrete electronic state are reported.

Each one of the reported experiments suggested that the simplified one-electron picture based on the fact that the confinement potential bends the Landau levels and the edge states are given by their intersection with the Fermi energy was not complete. First, a qualitative theoretical explanation was proposed by Beenakker [60]. A more quantitative effort to explain the experimental results is represented by a study by Chklovskii [19] that is now considered a cornerstone of the modern QHE research.

In the following section I will touch the main aspects of the theory following the Chklovskii [19] original paper connecting the theoretical work with the experiments. The first assumption that is that the scale on which the confinement potential changes is much larger than the magnetic length, $\lambda = (c\hbar/eB)^{1/2}$. This condition is extremely important because the geom-

etry of the edge states is a crucial factor in the understanding the transport phenomena and is strongly dependent on the shape of the confining potential. The main drawback of the one-electron picture is that it does not account for screening and its modification at strong magnetic field that modulates the electron density of states. This translates in high dependence on the filling factor, that changes from its bulk value to zero at the boundary of the 2DEG. The theory presents a self-consistent calculation in case of gate-induced depletion region (generalizable to the etched boundaries) of the width of the measured alternating compressible and incompressible strips at the edges. The result is that the, if we call l the width of the depletion region, the compressible stripes have width l and the incompressible $(a_B l)^{1/2}$ where a_B is the Bohr radius $a_B = \hbar^2\epsilon/(m^\star e^2)$ for a semiconductor with dielectric constant ϵ and effective carrier mass $m^\star$. The value of l depends on V_g and it is usually on the scale of several thousands of Å. The theory develops on three steps: first, it approaches the electrostatic problem of gate-induced 2DEG edge, second a magnetic field is introduced, and last the tunneling through the incompressible stripes is discussed. In this model, far from the boundaries, the electron density is considered homogeneous (n_0) and the perfect screening condition $E_F/V_g \sim a_B/l << 1$ is considered valid. The boundaries are defined by a gate potential $-V_g$, so that the boundary conditions for the electrostatic potential across the sample are:

$$\phi(x, z=0) = \begin{cases} -V_g, & \text{if } x < -l \\ 0, & \text{if } x > l \end{cases} \tag{3.18}$$

$$\frac{d\phi(x,z)}{dz}\Big|_{z\to 0} = \frac{4\pi e n_0}{\epsilon}, \quad \text{if } |x| < l \tag{3.19}$$

The system resembles a capacitor, where the metal plates are on the same plane of the dielectric with width 2l, in Figure 3.7, with $\epsilon >> 1$, in our specific case $\epsilon_{GaAs} \sim 13$ and The

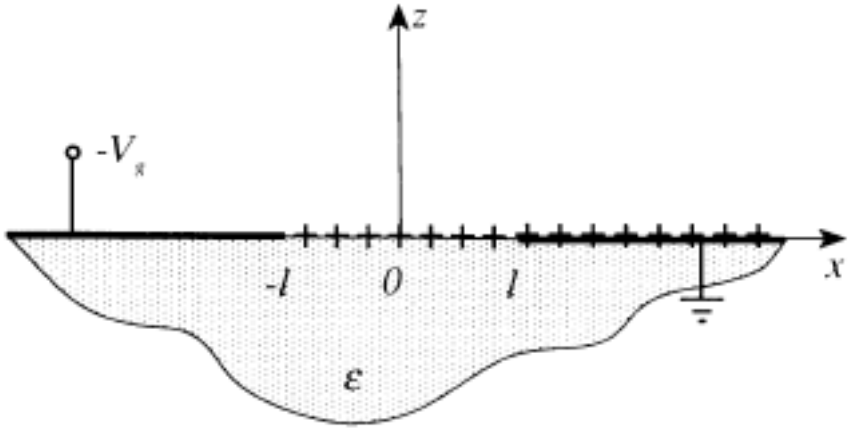

Figure 3.7: Capacitor with two conductive plates at potential $-V_g$ and ground, and the 2DEG as a dielectric. The systems is completely defined at z=0 and symmetric in y [19].

solution can be calculated as the sum two harmonic functions $\phi = \phi_1 + \phi_2$ and they can be found using the theory of complex variables. The solutions have a singularity in the electric field $E_x = -d\phi/dx$ at $x = l$ and the only way to get rid of the singularity is to have:

$$l = \frac{V_g \epsilon}{4\pi^2 n_0 e} \tag{3.20}$$

So that the density for the defined l is:

$$n(x) = \frac{d^2\phi}{dx^2} = \left(\frac{x-l}{x+l}\right)^{1/2} n_0, \quad \text{if } x > l \tag{3.21}$$

The only parameter that defines the electron density variation is l. For GaAs under a $V_g = 1$ V, density $n_0 = 10^{11}$ cm^{-2} and $\epsilon = 12.5$ we get for Eq. 3.20 l=2200 Å. The typical value for a_B is 100 Å, that satisfies the perfect screening condition. The same result can be

applied to etched samples substituting the half-width of the forbidden gap. Now that we have a clear electrostatic picture we can turn on a strong magnetic field H in the IQHE. The spin will be ignored from now on. Because the magnetic energy is much smaller than the electrostatic energy due to the gate ($\hbar\omega_c << eV_g$, with $\omega_c = eH/m^\star c$ cyclotron frequency), the with of the depletion region l will be unchanged. The only effect of the magnetic field from the electrostatic point of view is the periodic dependence of the screening properties of the 2DEG on the filling factor ν caused by the oscillations in density. In fact, at integer ν is completely absent while at non integer is very strong. This peculiar situation will lead to the formation of compressible and incompressible liquid regions, with the latter characterized by different integer fillings that will take the form of strips parallel to the edge.

The terms compressible and incompressible derive from the behaviour of density and potential in these regions. In compressible regions the Landau band is pinned at the Fermi level and screening is perfect, since electrons can easily be redistributed between available states so that the the density $n(r)$ can vary while V(r) is constant. On the other hand, in the incompressible regions the Fermi energy falls into a gap between (or below) the Landau bands and which do not contribute to screening since a redistribution of electrons is energetically impossible; the density is constant while V(r) varies. The chemical potential jumps with increasing density: $d\mu_{chem}/dn = \infty$. The new density of states is given by a series of delta functions centered at $\hbar\omega_c(k - 1/2)$ with k=(1,2,3,...) and the screening length:

$$r_S = \begin{cases} \infty, & \text{if } \nu = k \\ 0, & \text{if } \nu \neq k \end{cases} \tag{3.22}$$

In other words, the electrostatic potential is constant through anyone of the compressible strips and incompressible strips are formed at integer fillings. If we consider the example of $1 < \nu_0 < 2$, only one incompressible strip is formed. In Fig. 3.8 we show both the electrostatic energy and the charge density. The solution for the density found in Eq. 3.21 is

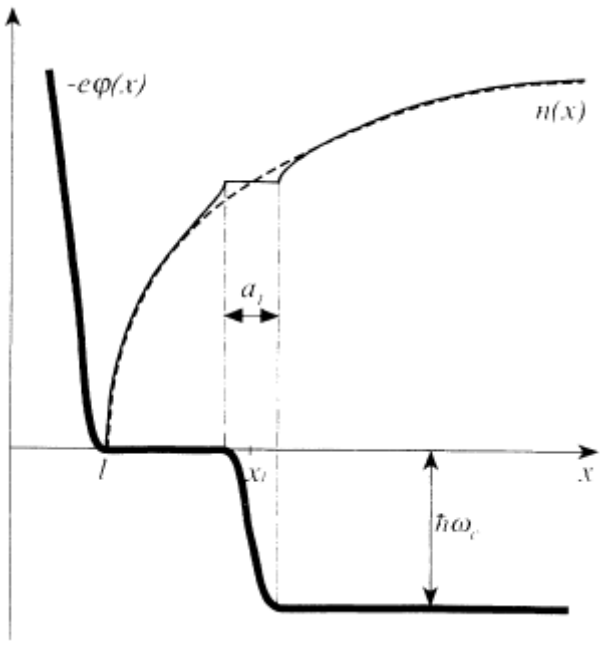

Figure 3.8: Electrostatic potential and density at $\nu = 1.5$ [19].

not the one that minimizes the energy anymore because of the additional magnetic energy cost $\hbar\omega_c$ involved in creating extra electron density at $\nu = 1$. If we call the location of the incompressible strip corresponding to $\nu = 1$ x_1 then the system will gain in energy if we relocate some of the electrons from the second LL to the first one in vicinity of x_1. During this process a drop in potential equal to $\hbar\omega_c/e$ between the edges of the incompressible strip is created, this is the reason why this strip is also called dipolar. On both sides of the strip we have compressible liquid where the electric field is completely screened. Solving the same electrostatic problem with an additional voltage drop of $\hbar\omega_c$ at the boundary of the stripes

of width a_1 gives the numerical result:

$$a_1^2 = \frac{2\epsilon\hbar\omega_c}{\pi^2 e^2 dn/dx|_{x=x_1}} \tag{3.23}$$

It is fundamental the existence of a finite concentration gradient in the zero-magnetic field solution. It is possible to generalize for the case of M Landau levels under the Fermi energy. The result is that the compressible strips b_k are much wider than the incompressible ones a_k, if we define the bulk filling factor $\nu_0 = n_0/n_L$:

$$a_k = \left(\frac{4}{\pi}\right)^{1/2} (a_B l)^{1/2} \frac{\nu_0^{1/2}}{\nu_0 - k} \tag{3.24}$$

$$b_k = \left(\frac{4}{\pi}\right)^{1/2} \left(\frac{a_B}{l}\right)^{1/2} \frac{\nu_0 - k}{\nu_0^{1/2}} \tag{3.25}$$

For an inner edge state $\nu_0 - k \sim 1$ the inequality $a_k << b_k$ still holds. A visual example for M=3 is provided in Figure 3.9 where the situation with screening and without screening effects are compared. Now that we have characterized the strips we can define a transport theory that involves redistribution of the current and can be compared with actual experiments. In the IQHE the experiment used as reference is the one produced by Alpheenaar et al. [21]. The current is injected only in outermost channel and after a certain distance is redistributed among the remaining channels. The proportion of the current flowing in the channels was measured. As already mentioned before, it was reported that in the vicinity of the integer bulk filling factor $N - 0.3 < \nu_0 < N + 0.3$ the equilibration length between the the Nth (innermost) channel and the rest $L_{N-1,N}$ grows rapidly and becomes to large to be measured at $\nu_0 \sim (N - 0.3)$. According to Chklovskii's theory [19] $L_{N-1,N}$ depends on

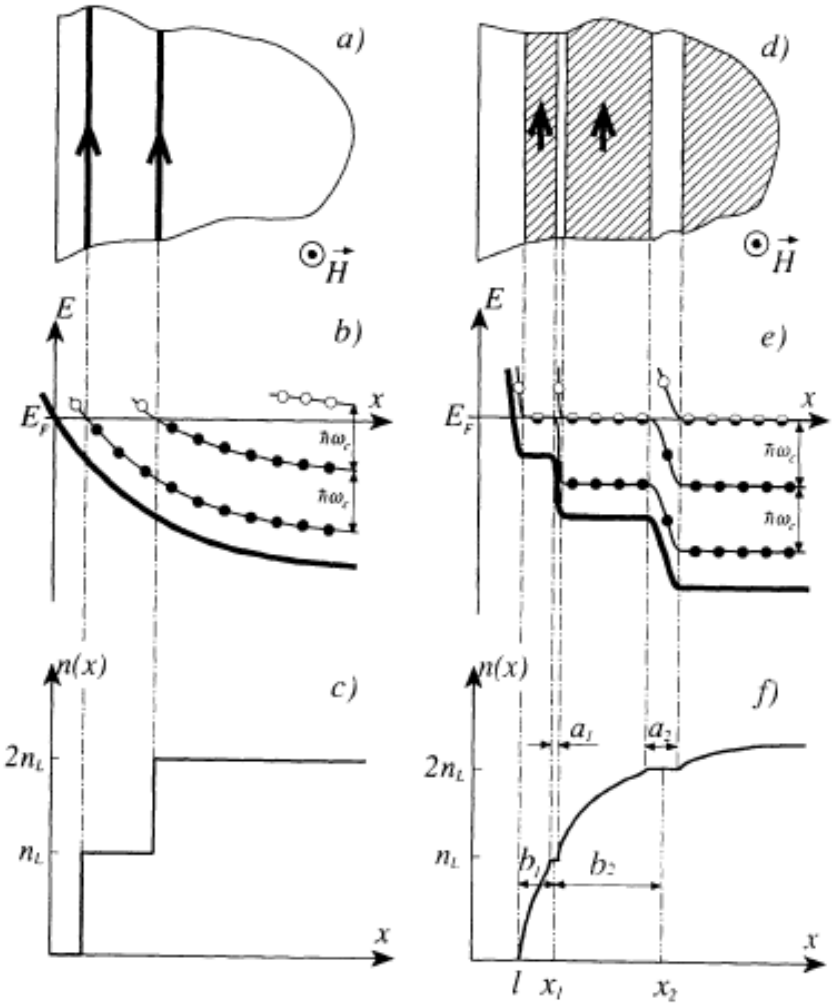

Figure 3.9: Edge channel configuration without (a-c) and with (d-f) screening effects. [19].

magnetic field only through $\Delta\nu = \nu_0 - N$ for $N >> 1$. The overlap between adjacent edge states determines the tunnelling between edge states so the equilibration length depends on a_{N-1}/λ. If $k = N - 1 = \nu_0 - \Delta\nu - 1 >> 1$ from Eq. 3.24 we get:

$$a_{N-1}/\lambda = \left(\frac{eV_g}{\pi^2 E_B}\right)^{1/2} \frac{1}{\Delta\nu + 1} \tag{3.26}$$

where $E_B \sim 6$ meV is the Bohr energy for an hydrogen-like impurity in GaAs. The equilibration length grows when we get close to ν_0 and increasing the disorder. In summary, there are N incompressible strips dividing the bulk into N channels and a compressible bulk region. The Nth incompressible strip is wide enough to prevent equilibration of the bulk. The resistance measured is $R = h/(e^2 N)$. Decreasing ν_0 we increase the width of the incompressible stripes, so the N-1 dipolar strip becomes wide enough to quench equilibration leading to gradual decoupling of the Nth edge channel.when ν_0 crosses N, the dipolar strip N becomes so wide to create a new bulk region. As we keep increasing the magnetic field, the (N-1) strip grows wider and wider making the equilibration into the Nth edge channel harder and harder, so that $R \sim h/[e^2(N-1)]$. Finally when $\Delta\nu = 0.3$, the (N-1)st dipolar strip becomes so wide that no measurable equilibration through it occurs and $R = h/[e^2(N-1)]$.

3.5 Breakdown of the QHE

Important for both metrology and fundamental investigation is the understanding of the physical mechanisms leading to the breakdown of the quantum Hall effect. Quantum Hall effect breakdown happens when suddenly the magnetoresistance becomes finite and a dissipation state is observed when the injected current exceeds some critical value. Even though a huge effort in understanding the phenomena is been produced in the last two

decades the debate on the subject is still wide open. Part of the experiments described in this thesis provide further insights on the breakdown process and together with the ones that I will soon present can help the scientific community to solve this longstanding puzzle. Many mechanisms have been suggested and I will provide a qualitative overview of the most cited ones.

3.5.1 Quasi-elastic inter Landau level scattering (QUILLS)

In the one-electron picture breakdown can happen when mixing of Landau levels is available. If we suppose that such a mechanism exists, we still need a momentum contribution to assist the transition to a spatially separated state, Figure 3.10. The source for this additional momentum can be found in acoustic phonons or impurities. So, the inter Landau level scattering can occur by emission of long-wavelength acoustic phonons whose momentum component must be high enough to take care of the spatial separation between wave functions. If for simplicity we only consider the acoustic phonons, we notice that the dissipative regime starts for electric fields that produce a drift velocity near the speed of sound in the material $v_s = Ec/B$. The phonon energy will be $E_q = \hbar v_s q \ll \hbar\omega_c$, for this reason the effect is called quasi-elastic [11, 12].

3.5.2 Super-heating process

The theory behind the heat instability if quantum Hall conductors has been developed in the late 90s by Komiyama and Kawaguchi [13, 14]. They base their discussion on the heat instability intrinsic to electron systems when they are influenced by electric fields. They predict a critical electric field for which the system becomes thermally unstable. At this field the dissipationless conductor transitions abruptly towards a resistive state through a bootstrap-type electron heating process. The reason for the breakdown is the fluctuation of

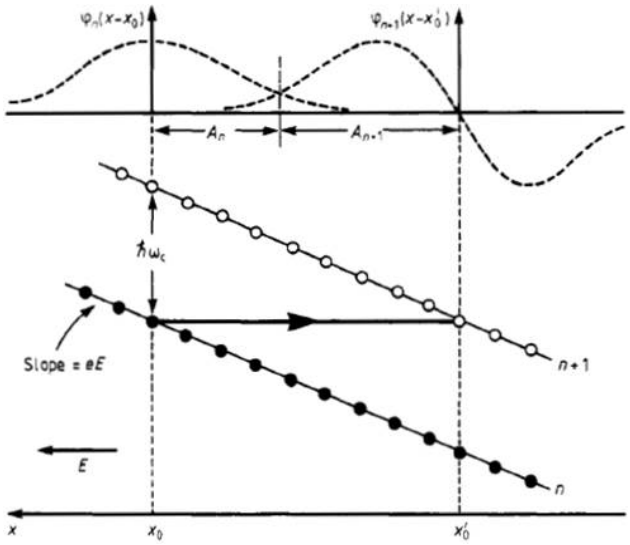

Figure 3.10: Schematic representation of the quasi-elastic scattering from filled Landau level n to empty level n + 1. The spatial overlap between the two the oscillator eigenfunctions is shown in terms of x_0 and x_0'. The wavefunctions shown correspond to the two lowest Landau levels. [12].

the electron distribution. The microscopic nature of the process can be described as follow. When the Hall electric field is greater than the critical field the electron system becomes thermally unstable. At non-equilibrium, a small number of electron-hole pairs is present in the system, because of the high field they increase their energy and create new pairs through the inter-Landau-level impact ionization. Electrons can only travel a small distance before a new pair is created so that an avalanche-type process is triggered, in Figure 3.11.

3.5.3 River formation model

As previously discussed, with increasing magnetic field the kinetic energy is frozen and the Coulomb interaction between electrons leads to the screening of the long-range potential fluctuations. Screening is perfect where the Landau level energy crosses the Fermi energy, while is absent in the rest of the system where LLs are either completely filled or empty. Only for filling factor very close to integer incompressible region percolate through the sample, leading to the QHE [19]. No matter how clean is the system, isolated compressible areas

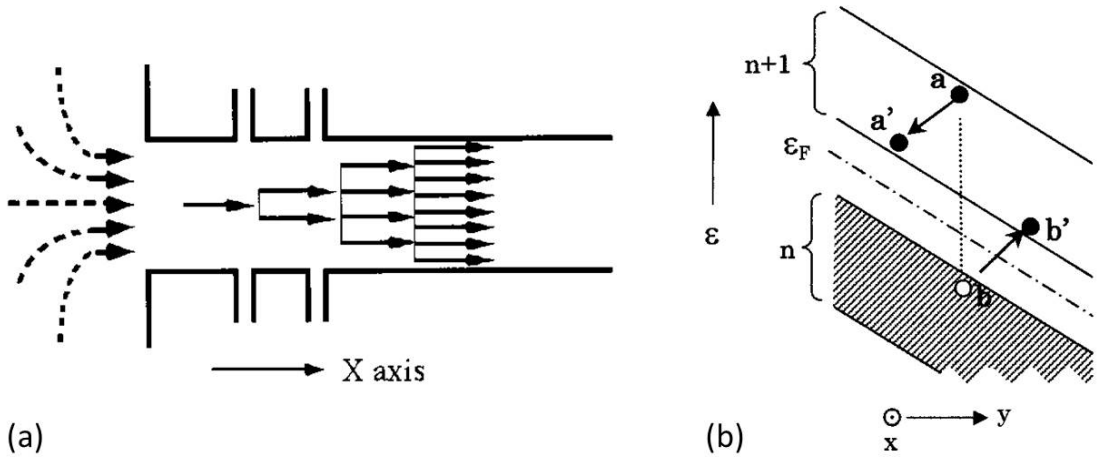

Figure 3.11: (a) Schematic representation of avalanche-type electron-hole pair multiplication generating on the left and exponentially increasing towards the right. (b) Schematic representation of the electron-hole pair excitation through impact ionization [14].

of perfectly screened disorder potential that behave like metallic liquids appear. In these regions the screened potential fluctuates around the Fermi level with an amplitude of the order of k_BT. The theory is based on the idea that there always exist an high enough critical current for which the incompressible region between two metallic bubbles breaks down and a conductive path can be established. As for the breakdown of any dielectric, this is due to the high electric field. When the connected regions form a percolating path between the opposite edges, a dissipative regime is suddenly observed [17]. The percolating path can be very complicated and the breakdown field depends on the density of metallic regions, Figure 3.12.

3.5.4 Magnetoexciton generation

The theory utilizes a hydrodynamic description of the breakdown. The presence of charge impurity-induced disorder makes the local quantum Hall fluid unstable when the charge velocity exceeds a critical value. When this happens, magnetoexcitons and electron-hole pair are created near the impurity. This theoretical model introduces a possible explanation

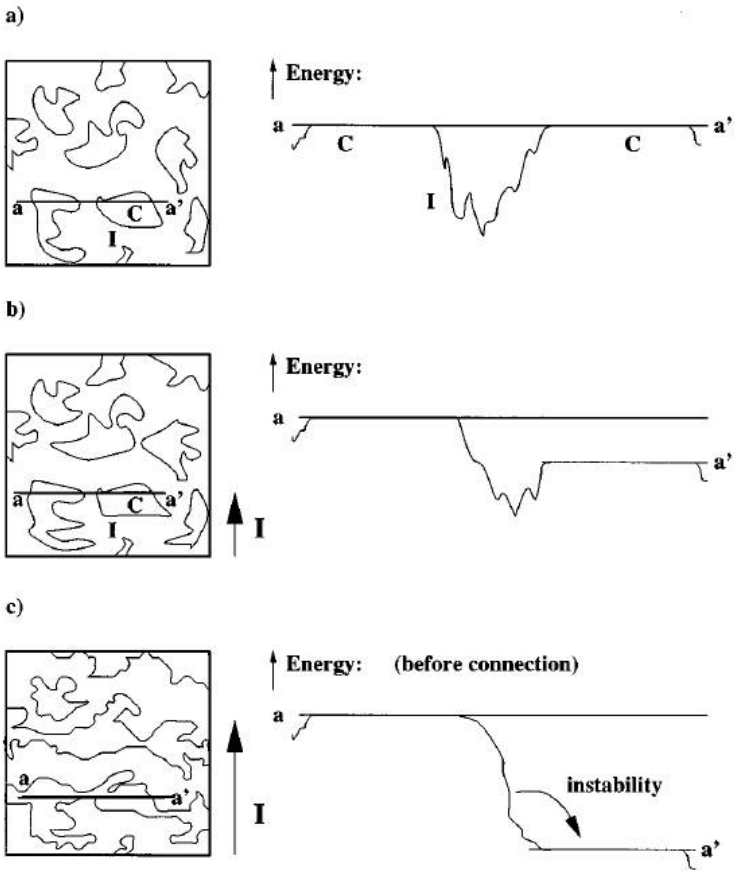

Figure 3.12: Distribution of metallic and incompressible regions in the QHE regime and energy diagrams. (a) When the system is at equilibrium all the regions are the same energy level. (b) Small electric field $E < E_c$ is applied, and no current flows between the edges. (c) The breakdown is reached by increasing the field over the critical value opening a current path between metallic regions [17].

for the presence of finite steps in the breakdown. The step height is related to the rate at which the pairs form. There is a critical electric field for which the electrostatic energy is equal to the excitation interaction energy and it costs no energy to generate pairs given a fixed wave vector. Ones the pairs are created they drift along the Hall bar and eventually ionize creating a dissipative current flowing across the equipotential edges. This is because the excited electrons have no states to relax [18].

3.6 Topological Insulator

The QH state can be considered the first example of a quantum state which is topologically distinct from all states of matter known before (first 2D topological order). The precise quantization of the Hall conductance is explained by the fact that it is a topological invariant, which can only take integer values in units of e^2/h, independent of the material details [26, 61]. The state responsible for the quantum Hall effect breaks time-reversal symmetry and it defines a topological phase in the sense that certain fundamental properties (such as the quantized value of the Hall conductance and the number of gapless boundary modes) are insensitive to smooth changes in material parameters and cannot change unless the system passes through a quantum phase transition [62]. A general feature of the theory is the *bulk-boundary correspondence*, which relates the topological structure of the bulk to the presence of gapless boundary modes. More precisely, the boundary topological invariant ΔN characterizing the gapless modes univocally corresponds to the difference in the topological invariant Δn (Chern number), characterizing the bulk on either side of the interface.

3.6.1 Introduction

Work on topological insulators grew out of the idea that the quantum Hall effect that arises in such 2D systems in the presence of a magnetic field could occur even for electrons moving on a lattice in the absence of a macroscopic magnetic field. Instead of being driven by such a magnetic field, it was predicted in the late 1980s that electrons could, in principle, form a quantum Hall state driven by forces that result from their motion through the crystal lattice. Recent developments are based on spin-orbit coupling, a relativistic effect in which the spin and orbital angular momentum degrees of freedom of electrons are coupled; this coupling causes electrons that are moving through a crystal to feel a spin-dependent force,

even in non-magnetic materials. Although spin-orbit coupling does not have the symmetry required to induce the quantum Hall effect (that is, it does not break time-reversal symmetry as an applied magnetic field would), in simplified models introduced in around 2003 it can lead to a quantum spin Hall effect, in which electrons with opposite spin angular momentum (commonly called spin up and spin down) move in opposite directions around the edge of the droplet in the absence of an external magnetic field [63].

Topological insulator is a novel state of matter whose description is to be an insulator that always has a metallic boundary when placed next to a vacuum or an ordinary insulator. I will give a overview of the concept of topological insulator, touching those aspects that have made it such an interesting subject of growing theoretical and experimental investigation and I will focus on the light shone on the Quantum For a deeper understanding of the theoretical expects I refer to very well done review papers as the ones from Hasan and Kane [62] and Qi and Zhang [64]. The first to introduce the concept of topology were mathematicians. They classify different geometrical objects into broad classes of topological invariants. For example, two-dimensional surfaces are classified by the number of holes in them. The surface of a perfect sphere is topologically equivalent to the surface of an ellipsoid, since these two surfaces can be smoothly deformed into each other without creating any holes. Similarly, a coffee cup is topologically equivalent to a donut, since both of them contain a single hole, 3.13. In mathematics, topological classification focuses on the fundamental distinction of shapes ignoring the smaller details [64]. In physics the concept of "smooth deformation" is applied to an Hamiltonian of a many-particle system that is changed without closing the bulk gap between the ground state and the excited state. If we put in contact two quantum states belonging to different topological classes, or put a topologically non-trivial state in

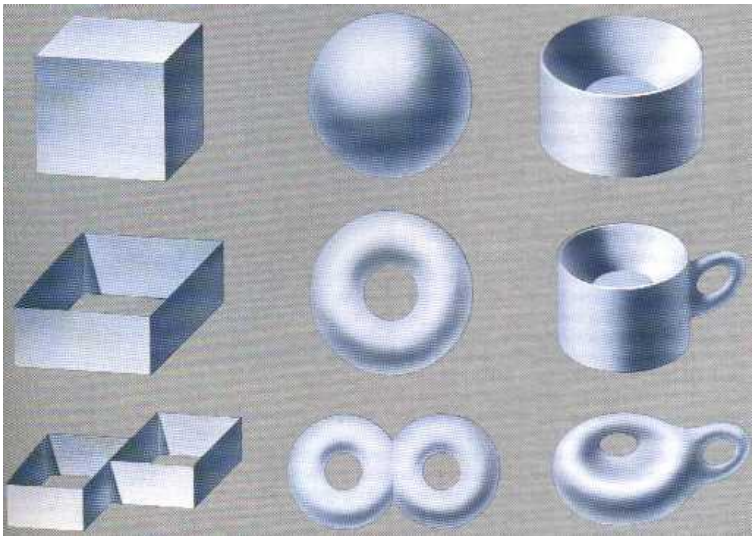

Figure 3.13: Sphere and donut belong to two distinct topological classes, because it is impossible to transition from one to the other without closing or creating an hole, that is a non-trivial topological characteristic [65].

contact with the vacuum, the interface must support gapless states.

3.6.2 Symmetry breaking.

All states of matter that were known until 1980 are connected by the same principle: they spontaneously break some kind of symmetry. For example crystals are periodic arrays of atoms that are not invariant under all translations (only under a small sub-set of translations by a lattice vector). For ferromagnetic materials, the underlying laws are invariant under spatial rotations. Here, the order parameter is the magnetization, which measures the magnetic dipole density. Above the Curie temperature, the order parameter is zero, which is spatially invariant, and there is no symmetry breaking. Below the Curie temperature, however, the magnetization acquires a constant non-vanishing value, which points in a certain direction (in the idealized situation where we have full equilibrium; otherwise, translational symmetry gets broken as well). The residual rotational symmetries which leave the orientation of this vector invariant remain unbroken, unlike the other rotations which do not and are thus spontaneously broken. In addition to these examples, there are a whole host of other symmetry-breaking phases of matter including nematic phases of liquid crystals, charge- and

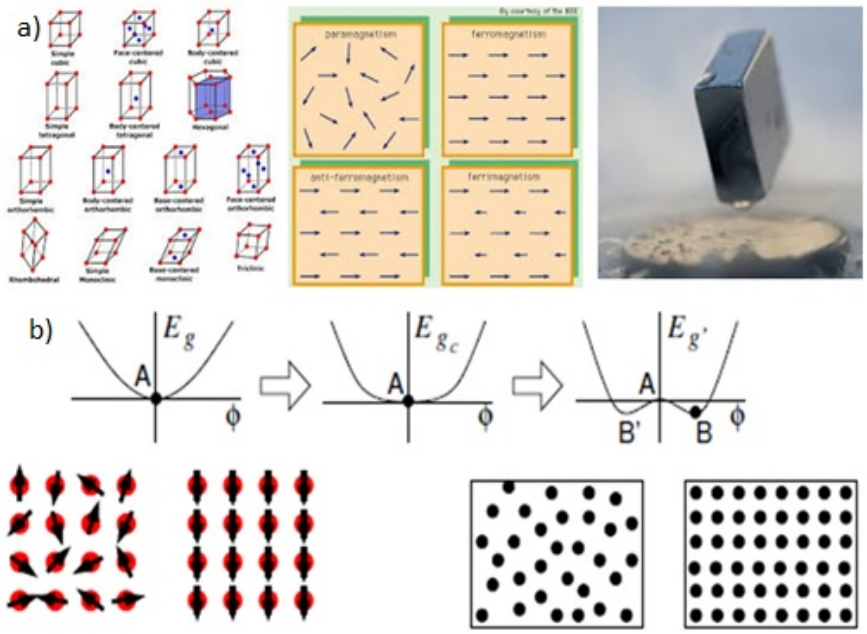

Figure 3.14: a) Some examples of phases of matter that involve symmetry breaking, from left to the right: crystalline solids, magnets and superconductors. b) a schematic of a the Landau-Ginzburg phase transition with ϕ being the order parameter.

spin- density waves, superfluids and many others. In superconductors, there is a condensed-matter collective field Ψ, which acts as the order parameter breaking the electromagnetic gauge symmetry, Fig 3.14. The Landau-Ginzburg theory formalizes this observation stating that a symmetry breaking leads to a unique order parameter, which assumes a non-vanishing expectation value only in the ordered state, and a general effective field theory can be formulated based on the order parameter. These theory gives a universal description of the states of matter based on general properties such as dimensionality and symmetry of the order parameter. But as always happens, in 1980 the exception to the role manifested itself in the form of a new quantum state: the Quantum Hall (QH) state [6]. In the QH state, the bulk of the two-dimensional sample is insulating, and the electric current is carried only through the edge of the sample. The flow of this unidirectional current avoids dissipation and gives rise to a quantized Hall effect. The conductive edges result from the topological

properties of the electronic wavefunctions when the constituent electrons are confined to two dimensions and subject to a strong magnetic field perpendicular to the plane to which the electrons are confined.

3.6.3 Topological band theory

The band theory describes the electronic structure of metals, semiconductors and insulators. The principal argument used for the classification of these states is the periodic translational symmetry of the crystal in terms of their momentum in the Brillouin zone, Block states $|u_m(\mathbf{k})\rangle$. These states are eigenvectors of an Hamiltonian $\mathcal{H}(\mathbf{k})$ whose eigenvalues, $E_m(\mathbf{k})$, define energy bands that collectively form the band structure. For insulators the last occupied band, valence band, is separated from the first empty band, conduction band, by an energy gap definitely greater than the thermal energy. Following the physical definition of topology we can intuitively see how in a certain way semiconductors and insulator belong to the same class. We can tune the Hamiltonian in such a way to go from one state to the other without closing the gap. Also we can assign to the same class the insulator par excellence: the vacuum, whose energy gap is the pair-production energy. All those insulator are part of the same topological class, the one that includes all the topologically trivial insulators. Has been proved that in nature are present topologically non-trivial states of matter. The integer quantum Hall effect (IQHE) is the first of a series of topological non-trivial states of matter. The precise quantization of the Hall conductance is explained by the fact that it is a topological invariant, which can only take integer values in units of e^2/h, independent of the material details [9, 26]. The state responsible for the quantum Hall effect breaks time-reversal symmetry and it defines a topological phase in the sense that certain fundamental properties (such as the quantized value of the Hall conductance and the

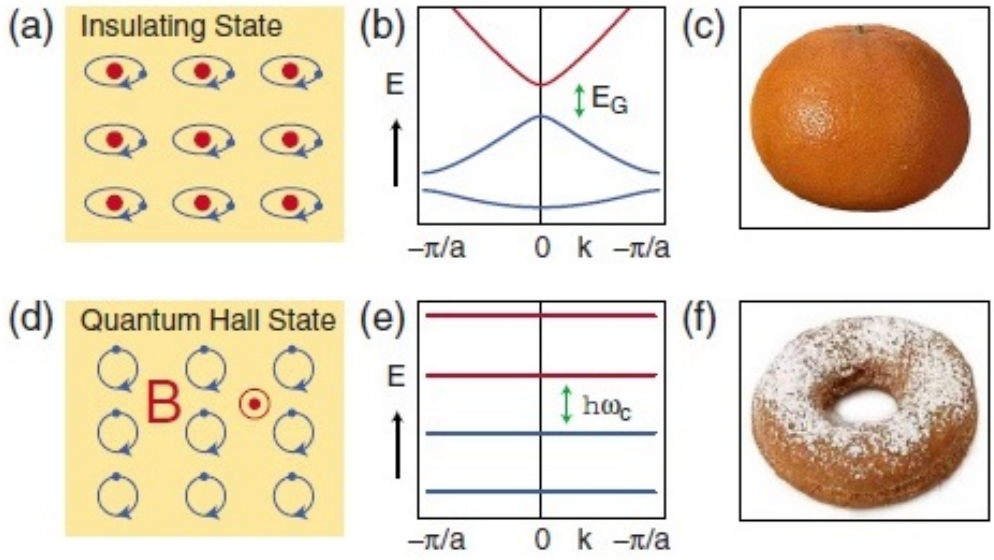

Figure 3.15: (a)-(c) Description of an atomic insulator with a qualitative model of an insulating band structure. (d)-(f) The quantum Hall state represented by the cyclotron motion of electrons. Also the Landau levels, which may be viewed as a band structure. (c) and (f) posses two different topology like atomic insulators and QH state [62].

number of gapless boundary modes) are insensitive to smooth changes in material parameters and cannot change unless the system passes through a quantum phase transition [62]. This state occurs when electrons are placed in a strong magnetic field. Quantization of the electrons circular orbits with cyclotron frequency c leads to quantized Landau levels with energy $E_m = \omega_c(m + 1/2)$. Landau levels can be viewed as a band structure, Fig. 3.15. If N Landau levels are filled and the rest are empty, then an energy gap separates the occupied and empty states just as in an insulator. Unlike an insulator, though, an electric field causes the cyclotron orbits to drift, leading to a Hall current characterized by the quantized Hall conductivity, $\sigma_{xy} = Ne^2/h$. The quantization of σ_{xy} has been measured to 1 part in 10^9 [66]. This precision is a manifestation of the topological nature of σ_{xy}. The difference between an normal insulator and a QH state can be explained through topology by the Thouless, Kohmoto, Nightingale, and den Nijs (TKNN) theory [9]. Gapped band structures can

be classified topologically by considering the equivalence classes of the Hamiltonian $\mathcal{H}(\mathbf{k})$) that can be continuously deformed into one another without closing the energy gap. These classes are distinguished by a topological invariant $n \in Z$ and Z denotes the integers called the Chern invariant. The Chern invariant is the physically connected to the Berry phase associated with $|u_m(\mathbf{k})\rangle$. For every value of $\mathbf{k}$ in the Brillouin zone we get a series of eigenvalues and eigenvectors whose phase in not well defined. Like for gauge transformations in electromagnetism, to a change in phase of the wavefunction corresponds a change in phase of the vector potential. In our case, the vector potential is represented by the Berry connection: $\mathcal{A}_m = i\langle u_m|\nabla_k|u_m\rangle$ and $\mathcal{A} \to \mathcal{A} + \nabla_k\phi(\mathbf{k})$. Physical quantities are invariant with respect to gauge transformations. One of those invariants is the change in phase acquired when we go through a full closed cycle in the momentum space. If we define the Berry curvature as $\mathcal{F} = \nabla_k \times \mathcal{A}$ than we have that the Berry phase is given by the integral of the curvature:

$$n_m = \frac{1}{2\pi}\int_S \mathcal{F}_m d^2\mathbf{k} \tag{3.27}$$

When we sum over all the occupied bands we get n, total Chern number, that is perfectly equivalent to N, the number of filled Landau levels. The Chern number cannot be changed with adiabatic transformations of the Hamiltonian, this means that is an invariant.

3.6.4 Quantum Spin Hall Insulators

Since the discovery of the QH effect, scientists believed that the existence of topological insulator was direct consequence of the breaking of time-reversal (TR) symmetry and two-dimensionality. $\mathcal{TR}$symmetry means that events (and likewise, the conduction channels) in the topological insulator have no preference for a particular direction of time, forwards

or backwards. Thus, any feature of the time-reversal-invariant system is bound to have its time-reversed partner, and this yields pairs of oppositely traveling edge states that always go hand-in-hand. After the discovery of the fractional QHE [7], it was predicted that electrons could form a quantum Hall state driven by forces that result from their motion through the crystal lattice. More than a decade later, has been recognized that electrons moving through a crystal feel a spin-dependent force even in non-magnetic materials. This phenomenon is due to the relativistic effect for which the spin and orbital angular momentum degrees of freedom of electrons are coupled, spin-orbit coupling (SOC). In this case, the $\mathcal{TR}$symmetry is not broken, but the SOC can lead to electrons with opposite spin move in opposite directions around the edge in absence of external magnetic field, quantum Spin Hall effect (QSHE). Moreover, a new degree of freedom is added: the QSHE can manifest in purely 3D systems. Insted of metallic 1D edges, we now have protected metallic surfaces. The first topological insulator was predicted in 2006 to be realized in HgTe/CdTe QWs [67]. The topological state is achieved by band inversion caused by the enhanced SOC due to the presence of heavy element (Hg).

3.6.5 Edge channels and bulk-boundary correspondence

The fact that there is no smooth transformation that can connect two insulators with different topology causes the appearance of low energy electronic states confined at the interface. In the case of the QHE these states are chiral, Fig. 3.16. At the same both spin up and down propagate in the same direction. This states are insensitive to disorder because there are no states available for backscattering. The chiral edge problem has been explicitly solved by Haldane [68]. The solid regions show the bulk conduction and valence bands, which form continuous states and an energy gap. At the boundary there is a single band

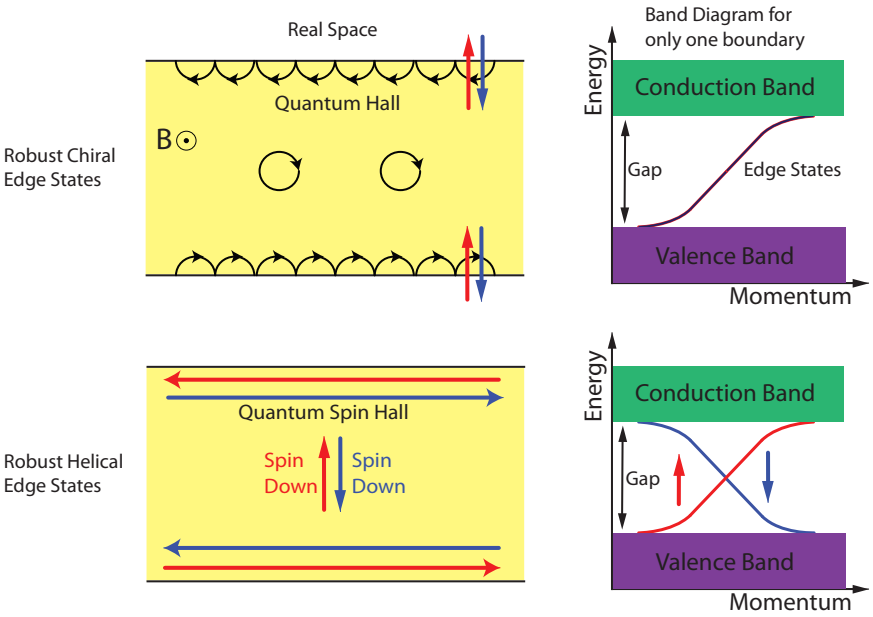

Figure 3.16: The electrons flow through the dissipetionless edge channels, with the rest of the system insulating. When there is a net forward ow of electrons for Hall resistance measurement, (left) those extra electrons occupy only the left edge channels in the quantum Hall system regardless of their spins, (right) opposite-spin electrons occupy opposite sides in the quantum spin Hall system.

that describes the low-energy states at the edge. The single band presents a positive slope, so that the group velocity of the carriers wavefunction is positive. The edge states dispersion is not unique near the interface. The Hamiltonian can be tuned so that the edge state dispersion gets modified and one or more kink can develop. If this happens, the dispersion intersects the Fermi energy, 3, 5, 7 or any other odd number of times. But the difference between the edge states with positive (right-going) and negative (left-going) group velocity is bound to always be: $\Delta N = N_R - N_L = \Delta n$. Where Δn is the difference in the Chern number (bulk invariant) across the interface. This is summarized by the bulk-boundary correspondence. One of the main characteristics of the Hall effect is that the topological states occur only if $\mathcal{TR}$ symmetry is broken. There is a different topological class that is the consequence of the spin-orbit interaction and does not require the breaking of the

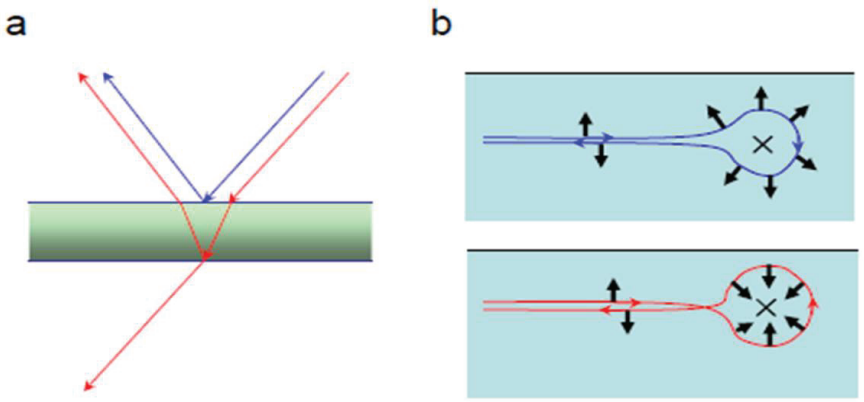

Figure 3.17: (a) Lens with antireflective coating. (b) Two possible paths taken by an electron on a QSH edge when scattered by a nonmagnetic impurity [70]

$\mathcal{TR}$ symmetry. For spin = 1/2 particles time symmetry is a antiunitary operator. In the presence of spin-orbit interaction, the Kramers' theorem, that states that all eigenstates of a $\mathcal{T}$ invariant Hamiltonian are at least twofold degenerate, has non trivial consequences. A 2D spin Hall insulator of this kind has topologically protected edge states. In a quantum spin Hall insulator, inside the same edge states the up spins propagate in one direction, while the down spins propagate in the other. Such edge states were later named helical [69] to emphasize the correlation between spin and momentum of a particle known as helicity. They can be considered as a 1D conductor that is half of an standard 1D conductor and they cannot be localized by disorder. Instead, standard conductors, which have up and down spins propagating in both directions, are fragile because of the localization effect due to weak disorder [35]. While chiral states are insensitive to disorder because there are no states available for backscattering, suppression of backscattering happens in a way similar to how the reflection of photons is suppressed by an antireflective coating. Helical states can be in principle scattered a nonmagnetic impurity via spin-obit interaction. Nonetheless, the different reflection paths interfere quantum-mechanically. As shown in Fig. 3.17, a spin up

forward-moving electron on the topological insulator edge has the choice of making either a clockwise or a counterclockwise turn around the impurity. But, because at the edge the spin down state propagates only backwards, the electron spin has to rotate adiabatically, either by an angle of π or $-\pi$. This two paths differ by a full 2π rotation. The wavefunction of spin-1/2 particles gain a negative sign, so that the two backscattering paths interfere destructively, leaving the particle no choice but to continue forward. This is a semi-classical explanation of how the QSH edges are protected by $\mathcal{TR}$ symmetry [70]. A different situation realizes when the impurity is magnetic. The $\mathcal{TR}$ symmetry is broken and the interference between the two backscattering paths is not destructive anymore.

CHAPTER 4 EXPERIMENTAL DETAILS

Now that we have a strong theoretical background, we can focus to find the best way to approach the *experimental* problem of the complex world of the study of two-dimensional interacting systems. I will describe the system that we are studying and how we built the best configuration to investigate its properties. Then I will talk about the technological tools we use to extract the right information. I will give an outline of the methods and results relative to the projects to which I have actively participated [71, 72] and focus the discussion on my main project: p(carbon)-doped (100) GaAs/AlGaAs quantum well structures with a well width of 20 nm.

4.1 GaAs-base device fabrication

The extremely high-purity wafer is provided by Dr. Loren Pfeiffer and Dr. Ken West from Princeton University, while the fabrication of the device as well as all the experiments are performed at Wayne State University. The charge carries are introduced by symmetric doping achieve through deposition of single layers (δ-doping) of carbons 130 nm away from each side of the quantum well in which the holes are trapped created by the band banding due to the contact between GaAs and $Al_{0.1}Ga_{0.9}As$. The deposition technology steadily improved in the last decades allowing to reach mobility of the order of 2×10^6 cm^2/(V·s). In Figure 4.1 we show the composition of the wafer and the band banding resulting from both doping and work function difference. From the original wafer we engineer the device and fabricate it in the clean-room following this processes:

- Mask Design
- Photolithography
- Metallic contacts deposition

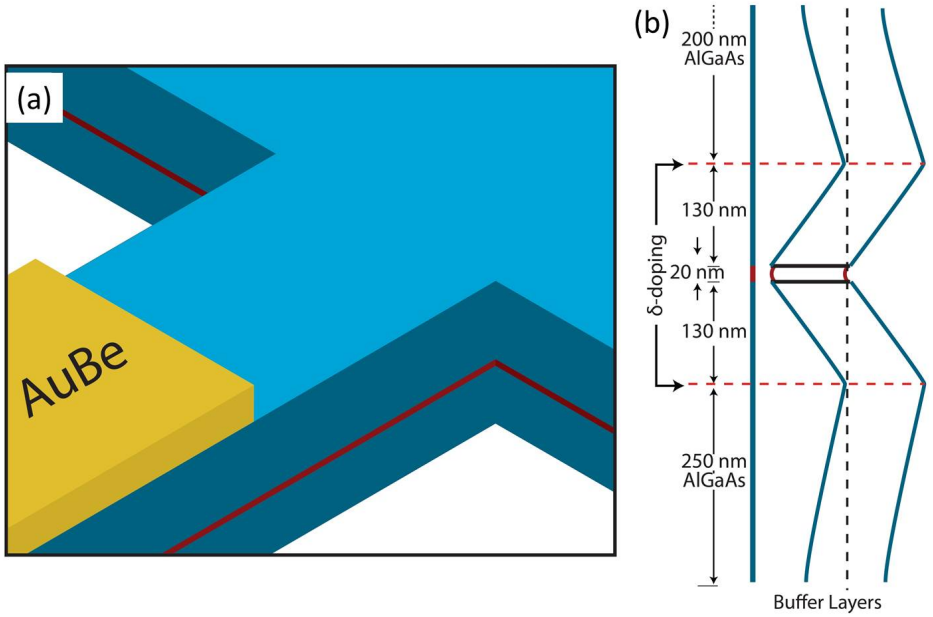

Figure 4.1: (a) 3D particular of the cross section of the sample, in red the 2DHG is shown. (b) Qualitative schematic of the band banding of conduction and valence band in the z-direction. The 20 nm GaAs quantum well sits between 130 nm of AlGaAs. Then the symmetric δ-doping is shown using dashed red lines. The Fermi energy (black dashed line) intersects the valence bans at the quantum well to create the 2DHG.

- Forming Ohmic contacts

To realize each step we have to follow a very well defined procedure that involves the use of different techniques and machines. I will describe them, without dwelling on unnecessary details, each one of them emphasizing the most delicate parts.

4.1.1 Clean-Room

The entire fabrication process takes place in the *Clean Room*.Fig.4.2, that is constantly maintained at a temperature of 68 ° C and at a humidity of 48 % by a conditioning system. The clean room, as the word says it is a room where the air, the water and all the objects are supposed to be as much clean as possible in order not to contaminate the sample. Our specific clean room is a class 100, this definition sets the limit for the quantity of undesired particles allowed in. Fig.4.2. In an adjacent room, connected to the first one, we placed all

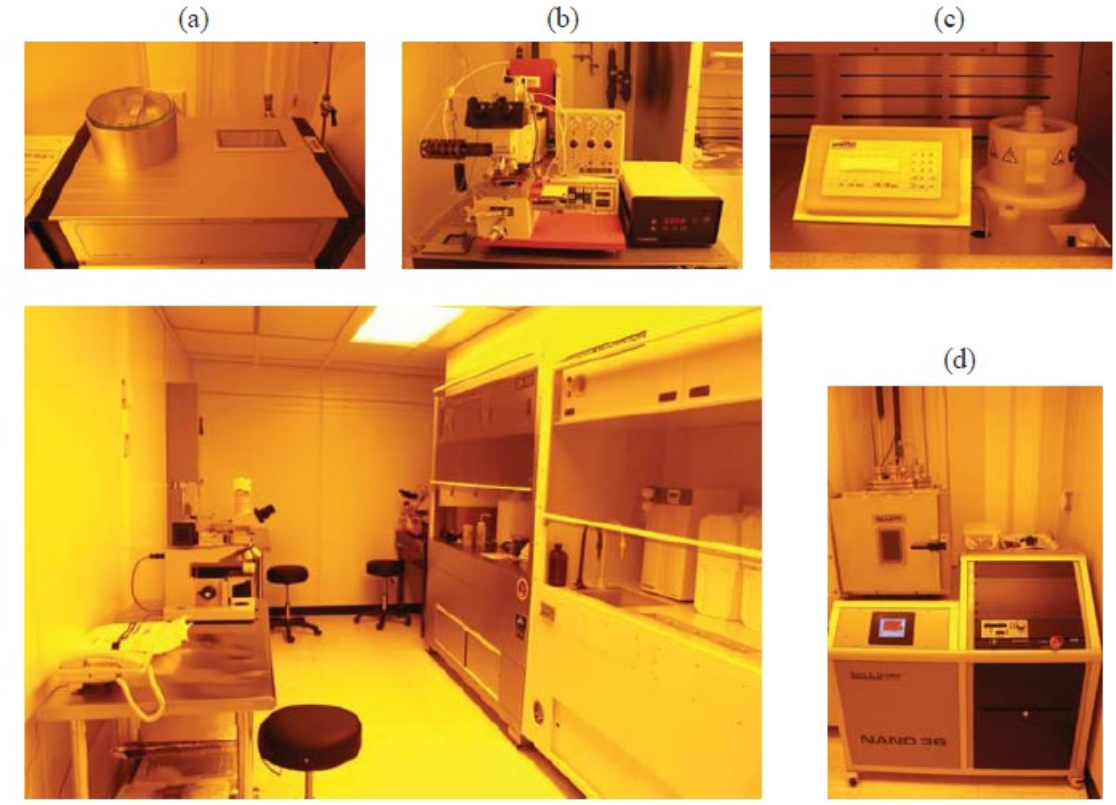

ISO 14644-1 Cleanroom Standards

	Maximum Particles / m³						FED STD 209E Equivalent
	≥0.1 µm	≥0.2 µm	≥0.3 µm	≥0.5 µm	≥1 µm	≥5 µm	
ISO 5	100,000	23,700	10,200	3,520	832	29	Class 100

Figure 4.2: The clean room: (a) thermal annealer AO500, (b) the mask aligner MJB-3, (c) the spinner and (d) the evaporator Nano-36 and on the bottom we can see particle requirements for a class 100 Clean Room.

Figure 4.3: Spinning system.

the supplies of compressed air, nitrogen, foaming gas and DI water.

The first step when we have in our hands the AlGaAs/GaAs wafer is clean it with acetone and IPA and spin-coat it with photoresist S1813 to protect it from damages during the cleaving procedure. The main function of the photoresist is not to protect the sample, but as we will see later on in this chapter it is of vital importance for the photolithography technique.

This procedure is purely mechanical, we use a spinner, Fig.4.3, that is a machine that uses vacuum to hold the sample in place and it makes it spin at a velocity that can reach 10000 rpm, this motion will spread the photoresist that we put on top of the sample creating a thin film, (usually thinner than $1\mu m$) the thickness would depend on the density of the photoresist, the angular velocity of the spinner and the time of spinning. Other important parameters are the temperature and humidity of the clean room because they affect the viscosity of the photoresist. Now we can cleave the sample to a size of a few millimeters square[1] and remove the photoresist with acetone and IPA. It's time to form the Hall bar, we spin photoresist on the sample and we soft-bake it (95 °C) for a less then two minutes on

[1] This is not the size of the Hall bar!!!

the hot plate. If the temperature is to high it will be impossible to develop the photoresist.

4.1.2 Photolithography

The next step is to impress the pattern of the Hall bar on the photoresist, *photolithography*, (writing with light). To do so we use ultraviolet light shining on a mask, with a well defined shape. The mask is made of CuO and presents the patterns of the Hall bar and of the contacts. When the UV light interacts with the photoresist it makes it active to the developer, so only the portion of the sample which was illuminated will develop. The photolithography is a delicate procedure, we use the self-aligned technique operating with SUSS MJB-3,Fig.4.4, that shines light with a wavelength of 365 nm. The exposure time obviously depends on the thickness of the photoresist layer. The next step is the *development* of the

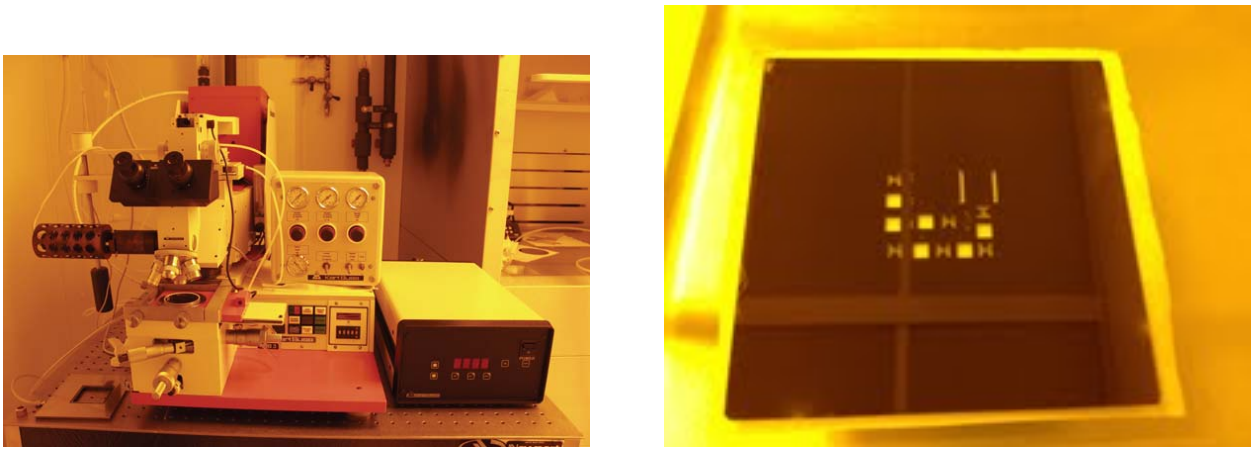

Figure 4.4: On the left we can see MJB-3 and on the right we have the mask that we utilized for contacts deposition on graphene.

exposed photoresist. More precisely the developer 352 will dissolve the activated part of the photoresist living an empty pattern that is the exact copy of the mask. When the pattern is visible we rinse the sample with DI water and proceed to the next step: *Hard baking*. It is necessary to hard bake 105 ° C for 10 minutes the sample because we need the photoresist to be strong enough to protect from the etchant agent the areas still covered. Also we need to

dip for a few seconds the sample into a diluted base so that we can eliminate oxide deposits from the surface that will prevent the etching. Now that we treated the photoresist we can proceed to the *Etching*.

4.1.3 Wet Etching

We want to "dig deep" enough to etch beyond the two-dimensional layer to isolate the hole layer, and we do not want to reach the bottom gate layer. In our case we need to etch about 500 nm deep. After some calibrations about the depth and about the morphology of the etched region, Fig.4.5[2] we found that for our specific etchant, $H_2SO_4 : H_2O_2 : H_2O = 4 : 5 : 80$, and our specific sample the etching time is 60 seconds, the etching rate is strongly dependent on the temperature of the room, so it is extremely important to maintain the room at constant temperature. After rinsing we can go to the next stage. The shape of the device is defined. The dimensions of outer and inner edge are respectively 2.4 × 3.0 mm and 1.4 × 2.0 mm with a distance between the longitudinal contacts of 0.8 mm, Fig.4.6. We now need to *form the contacts*. So we spin-coat the sample, soft bake and expose to UV light with the self-align technique using a mask with the contacts pattern. The just etched sample is very delicate, every second in air lowers is quality, so it is of enormous importance to move as fast as we can to the vacuum chamber of the Evaporator K. J. Lesker Nano 36, Fig.4.7 for the *Thin Film Metal Evaporation*.

4.1.4 Metal Deposition by Thermal Evaporation in High Vacuum

The high vacuum thermal deposition (HVTD) it is a deposition technique that uses the thermal energy supplied by tungsten wires to heat the materials to be evaporated within a crucible. This technique allows you to deposit with high precision, of the order of a

[2] We used a profilometer to measure the etching rate: we etch different samples for different intervals of time and than measured the depth of the etching

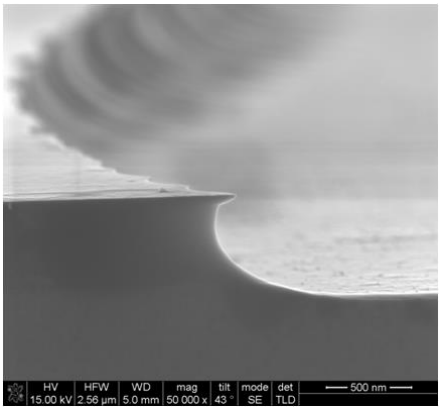

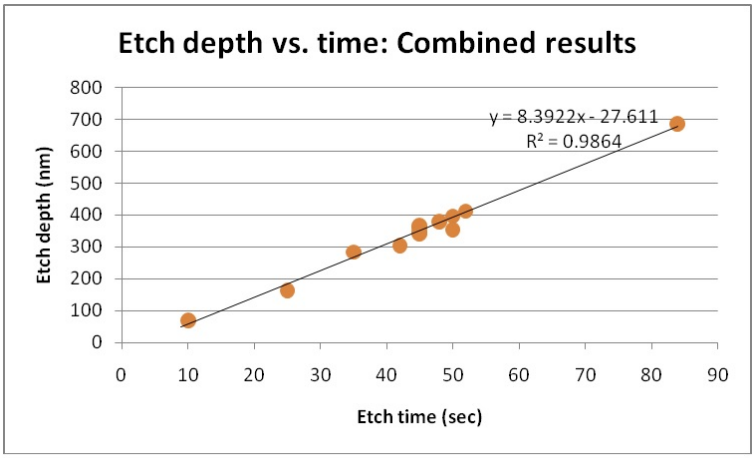

Figure 4.5: On the left we have an SEM image of an etched profile. On the right there is the calibration curve for the etching depth vs the immersion time.

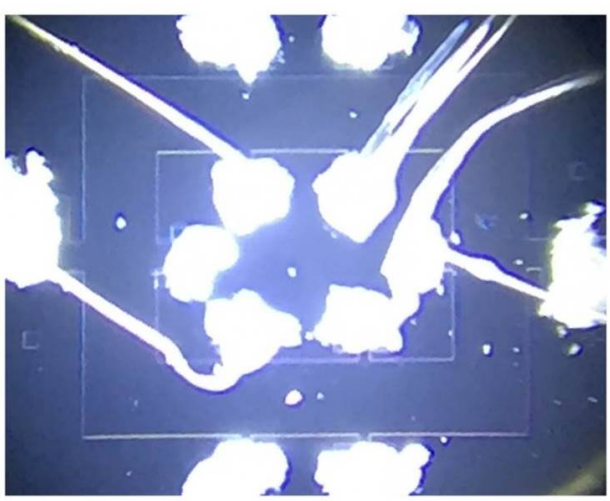

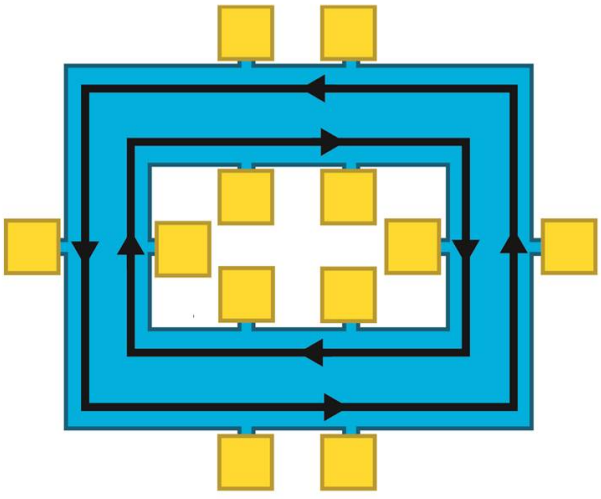

Figure 4.6: On the left we show a picture of one of the actual devices used for the experiment. The metallic contacts are covered by silver paint and connected to the sample holder's pins through gold wires. On the right a schematic of the device.

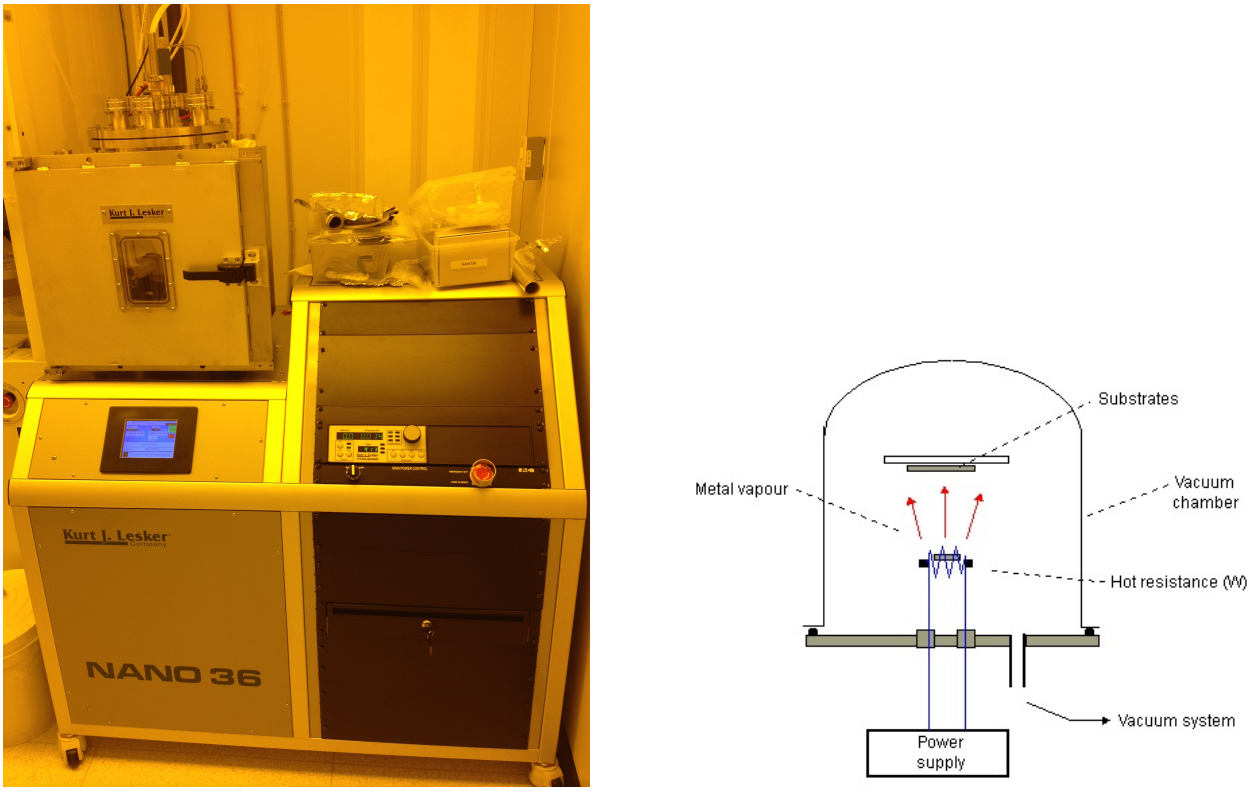

Figure 4.7: Nano36 is used to evaporate metal on the sample, it operates at a pressure of 10^{-7} torr, on the left a schematic representation of the machine.

few angstroms and to work in an environment that minimizes the possibility to deposit impurities and materials other than those desired usually working pressure not exceeding 10^{-7} Torr during deposition. The crucibles are located at the base of the evaporation vacuum chamber, while the sample is in the upper zone, the material is evaporated and deposited by condensation on the sample. The rate is controlled by the amount of thermal energy supplied to the crucibles and can be measured through a quartz balance that gives as output the value of the equivalent layer of deposited material, ie the scale measures the mass of the deposited material and using a preset density value, calculates what would be the the thickness of the deposition as if it would be uniformly distributed. More in particular we deposited a film of 60 nm of Gold-Beryllium (AuBe) (1% in weight) followed by a film of 10

nm of Gold (Au) for the contacts. An important factor during this process is the evaporation rate, evaporating to fast would lead to a non perfect arrangement of the metallic atoms on the sample; we tuned the rate to $1\mathring{A}/s$. I want to underline how important is the role of the clean room and of the high vacuum chamber in the fabrication process. From the kinetic theory of gasses we can estimate how many particles hit our sample every second, this rate is given by:

$$\dot{n}_s = \frac{1}{4} N_g \bar{v} \tag{4.1}$$

where N_g is the number of molecules of gas per cm^3 and $\bar{v}$ is their average thermal velocity. From (4.1) follows that:

$$\dot{n}_s = N_g \sqrt{\frac{RT}{2\pi M}} \approx 2.7 \times 10^{22} \frac{p}{\sqrt{MT}} (cm^{-2} s^{-1}) \tag{4.2}$$

being R the gas constant, T the absolute temperature, M the molecular mass and p the gas pressure in mbar. If we think that one layer is composed of approximately 10^{14} particles/cm^2, with an average molecular mass $M = 28$ and at a room temperature $T = 300$K, from (4.2) we get:

$$\dot{n}_s \approx 10^6 \times p(layers/s) \tag{4.3}$$

. It is for this reason that we want to work as fast as we can and store the sample under vacuum and well protected from impurities. At this point we need to proceed to the *lift off*.

4.1.5 Lift-off

After the evaporation, the sample is completely covered by metal, but we need only the contacts to be covered, so recalling that the contacts are the only region where the

photoresist was removed by the developer, we will dip the sample in acetone. In that way all the photoresist will dissolve and living the overlying layer of metal floating in acetone. In this way we will be left with Gold-Beryllium and Gold only on the contacts. Now a question arises: is the physical contact enough to have Ohmic contact? First of all, what is an Ohmic contact?

4.1.6 Ohmic Contacts

Every time we have a junction between two materials we will that their Fermi Level or chemical potential as to align at the thermal equilibrium. Now in the special case of a semiconductor and a metal two situations can take place:

- we have a rectifying junction (Schottky diode)
- we have a non-rectifying junction (Ohmic contact)

at first approximation to see if our contacts are Ohmic we can plot their current-voltage (I-V) curve and if it is linear and symmetric we will have a good contact if it non-linear and asymmetric we are observing a Schottky diode.

The origin of this behaviour of the metal-semiconductor junction is that when the chemical potential of the two materials aligns bending the valence and conduction bands. For a metal and a semiconductor the difference between the Fermi energy and the vacuum level is the work function respectively ϕ_m and ϕ_s, moreover for a semiconductor the difference between the conduction band and the vacuum level is the electronic affinity χ_s. When the Fermi levels align we will have that the material with lower work function will get a small positive charge while the other will be slightly negatively charged, so an electrostatic potential will form at the junction V_{bi}, *built-in potential*.Fig.4.8. This potential is the cause of the rectification phenomenon in diodes. Without going into even more detail we can qual-

itatively say the Ohmic contact come from the tunneling of that barrier, so that is more probable to have Ohmic contacts if the electronic affinity of the semiconductor and the work function of the metal have very close values[3]. Also very often to make better contacts the region is heavily doped, as for our gate contact.

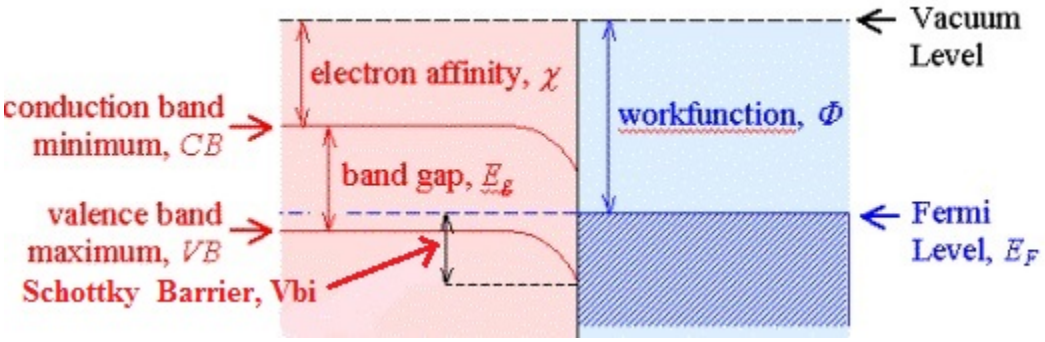

Figure 4.8: Formation of a Schottky barrier in a metal-semiconductor junction.

4.1.7 Annealing

The answer is no, at least not always. So to make sure that we have a real good contact between the metal and our two-dimensional layer we will have to make the metal diffuse into the sample. The easiest way to do it is to thermally activate the diffusion through annealing. The diffusion process is very sensible to the temperature, in fact as we can see from the Fick's Law:

$$\frac{\partial \mathcal{C}}{\partial t} = D\frac{\partial^2 \mathcal{C}}{\partial x^2} \tag{4.4}$$

where $\mathcal{C}$ is the concentration and D is the diffusion coefficient with a temperature dependency:

$$D(T) = D_0 e^{-\frac{E_d}{kT}} \tag{4.5}$$

[3] Metals with high work functions form the best contacts with p-type semiconductors and those with low work function form the best with n-type

with E_d the activation energy. So by changing temperature we will be able to tune the diffusion rate and we can control the diffusion depth by regulating the time of annealing. Obviously each material has a peculiar diffusion coefficient. We annealed our sample at 420 °C using the Compact Rapid Thermal Annealing System AO 500 (RTA), Fig.4.9, this machine permits to control the temperature very accurately and because of its small dimension allows a pretty quick annealing. The annealing process has to be performed while continuously flushing forming gas to reduce the oxides on the metal surface. Right before the annealing we always check the all the contacts under optical microscope to make sure they are clean.

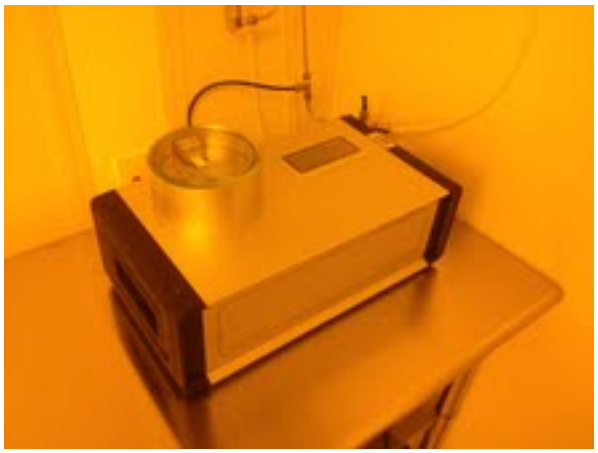

Figure 4.9: Thermal annealing system used to achieve ohmic contacts.

The scheme below summarizes all the passages of the fabrication:

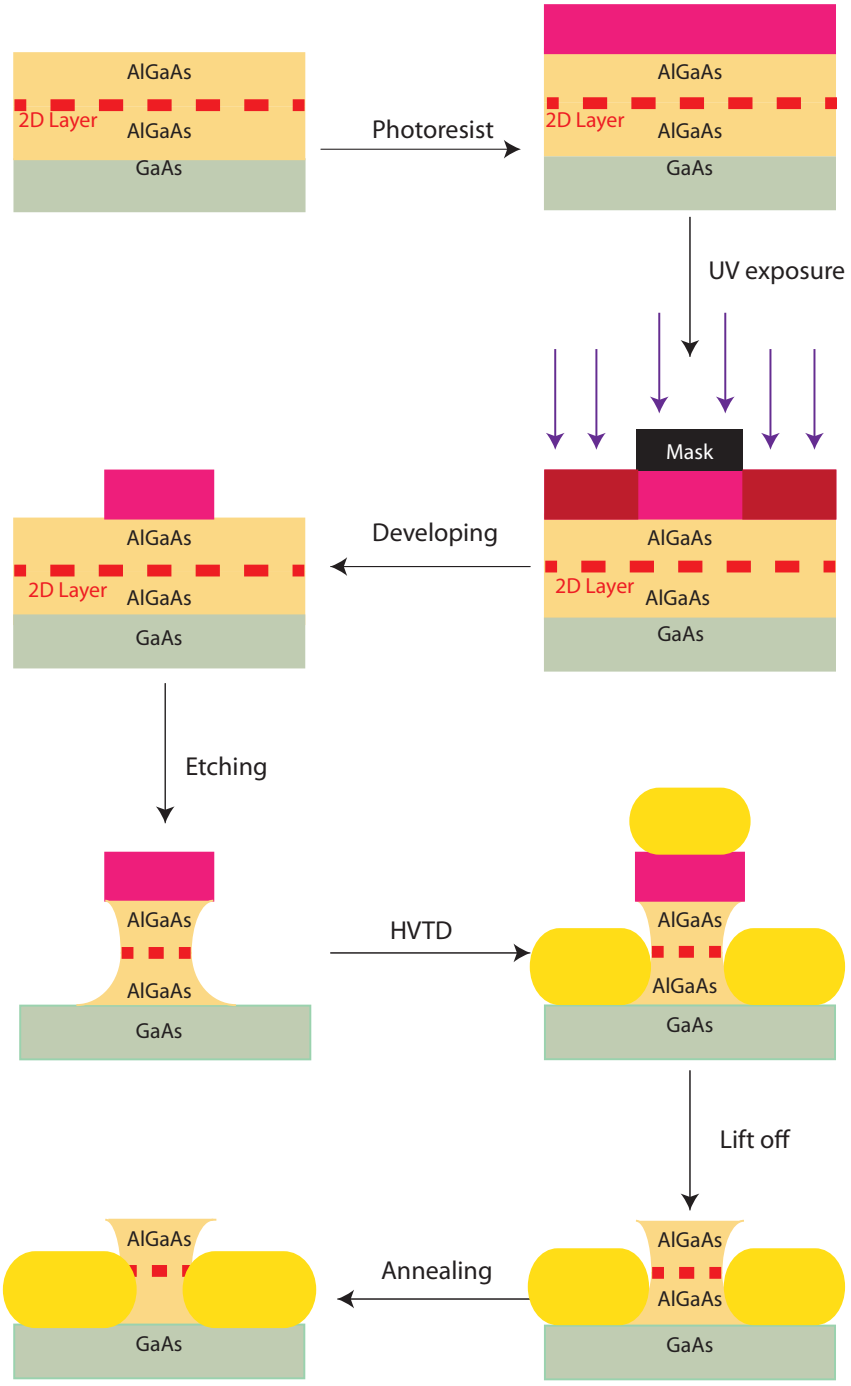

Figure 4.10: General summary of the main fabrication steps.

4.2 Graphene-based device fabrication

I will give a brief introduction to graphene, focusing my attention on its electric properties.

4.2.1 What is Graphene?

Graphene represents a conceptually new class of materials only one atom thick, two-dimensional materials[73], it presents exceptional electrical and mechanical properties. Graphene

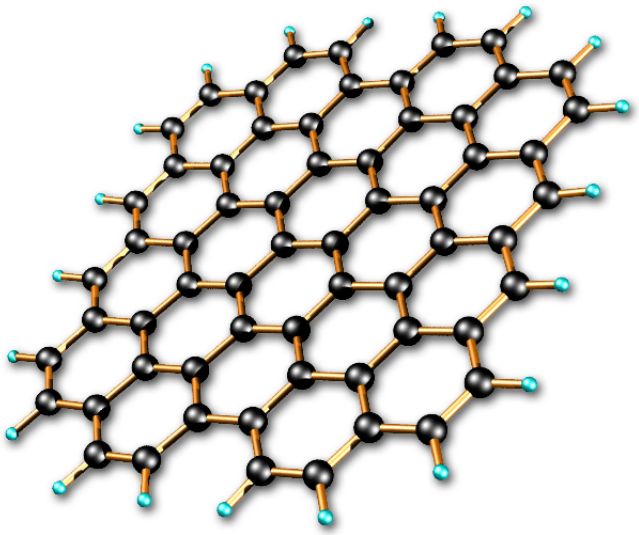

Figure 4.11: Model of a graphene sheet [74].

is an allotrope of carbon whose structure is a single planar sheet of sp^2 bounded carbon atom that are packed in a honeycomb crystal lattice. The characteristic length of the covalent bond C-C is 1.42 Å. A superposition of many layers of graphene bonded by weak Van der Waals forces forms graphite with an inter-planar spacing of 3.35 Å.

4.2.2 Main Properties of Graphene

The existence in the free state of a two-dimensional material was considered thermodynamically impossible until the last decade: thermal fluctuations in the crystal lattices should lead to a displacement of the atom comparable to the inter-atomic distances at any not zero

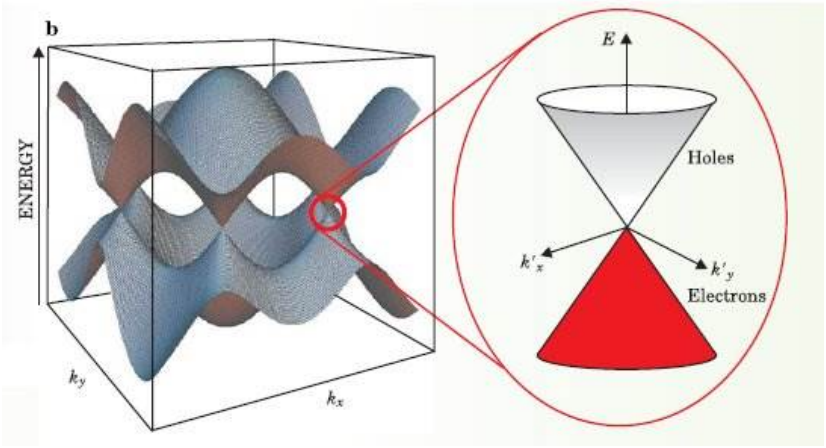

Figure 4.12: Electron band structure in graphene, we can see that in K and K' the dispersion relation is linear[76].

temperature.

First of all we need to define when we can talk about two-dimensional material: the screening length in graphite is only 5 Å, less than two layers, so we should consider almost 3D even films of 5 layers. But we can produce many 2D-like materials, why the graphene is so interesting? The answer is that it presents *exceptional electronic properties*. Graphene is a semimetal: it presents a very small overlap between the bottom of the conduction band and the top of the valence band, it has no band gap and a negligible density of states at the Fermi level. The dispersion relation is linear at the corners of the hexagonal Brillouin cell, this leads to a relativistic behavior of charge carriers Fig. 4.12 [75]. This implies that the electrons and holes should be treated with the Dirac Equation and no more with the Schrödinger's: This situation brings to the fact that electrons and holes mobility is still incredibly high even

$$i\hbar\frac{\partial}{\partial t}\Psi(\mathbf{r},t) = \left[\frac{-\hbar^2}{2m}\nabla^2 + V(\mathbf{r},t)\right]\Psi(\mathbf{r},t) \Rightarrow \left(\beta mc^2 + \sum_{k=1}^{3}\alpha_k p_k c\right)\psi(\mathbf{x},t) = i\hbar\frac{\partial\psi(\mathbf{x},t)}{\partial t}$$

Figure 4.13: We must pass from the Schrödinger Equation to the Dirac

at room temperature and with doping up to 10^{12}. This shows that the mobility is limited

only by impurities and defects and could reach extremely high values of the order of 100,000 $cm^2V^{-1}s^{-1}$ which translates into ballistic transport on the submicrometric scale (up to 0.3 μm at 300 K) and to a resistivity of $10^{-6}\Omega \cdot cm$.

Other important peculiarities are the excellent thermal conductivity, also is one of the strongest materials: measurement have shown that graphene has a breaking strength 200 times greater than steel. Before going further we must underline that the graphene band structure varies very rapidly with the number of layers: only graphene and its bilayer can be considered semimetals or zero-gap semiconductors, for three or more layers the electronic spectrum becomes increasingly complicated. The conduction and valence band start notably overlapping. This allows single, double and few (3 to <10) layers of graphene to be distinguished as three different types of 2D crystals[73]. The applications of graphene are almost infinite and the great part of them is still under development: Lightweight, thin, flexible, yet durable display screens, electric circuits, Solar cells, Single-molecule gas detection, various medical, chemical, and industrial processes enhanced or enabled by the use of new graphene materials, photodetectors, etc...

4.2.3 Production of Graphene

There are many different ways to produce graphene, each of them has its own advantages and disadvantages, the principal are:

- Exfoliation: an adhesive tape its used to repeatedly split bulk graphite crystals into increasingly thinner pieces, but the sheets produced are small,
- Epitaxial growth on SiC: the substrate is heated at temperatures higher than 1100 $^\circ C$ and it reduces to graphene,
- Epitaxial growth on metals: a source of carbon brings the atoms in contact with the metal

making them organize according to the atomic structure of the metal. But usually the bonding between the bottom graphene layer and the substrate affect the properties of the graphene,

- Graphite oxide reduction: the graphite is heated and the result is a highly dispersed carbon powder with a few percent of graphene flakes, but the quality of these flakes is very low.
- From graphite by sonication: graphite is put in a proper liquid and sonicated. After its separated from the graphene by centrifugation.

In our research we produced the graphene in two ways: exfoliation from natural graphite and Chemical Vapor Deposition on SiO_2.

4.2.4 Exfoliation from natural graphite

Graphite occurs naturally in metamorphic rocks as a result of the reduction of sedimentary carbon compounds during metamorphism, it also occurs in igneous rocks and meteorites[77]. We want to get a single sheet from the rock and because the bound between the sheets is very weak (Van der Waals force) we can easily peal off layers of graphene simply using an adhesive tape. The problem with this procedure is that if we use a too adhesive tape we will have a lot a glue residuals on our substrate and it will also be more difficult to transfer the graphene from the tape to the substrate. Our substrate is silicon with 290 nm of silicon dioxide on top, we expressly chose the thickness of the oxide so that for thin film interference it would be easier to detect under purple light the graphene sheet, otherwise almost completely transparent.

After trying many different approaches to the problem of the graphene transfer we found that using a less adhesive and heating up the substrate to almost 200 $^{\circ}C$, would lead to the production of bigger and cleaner graphene sheets. The reason is simple: heating the

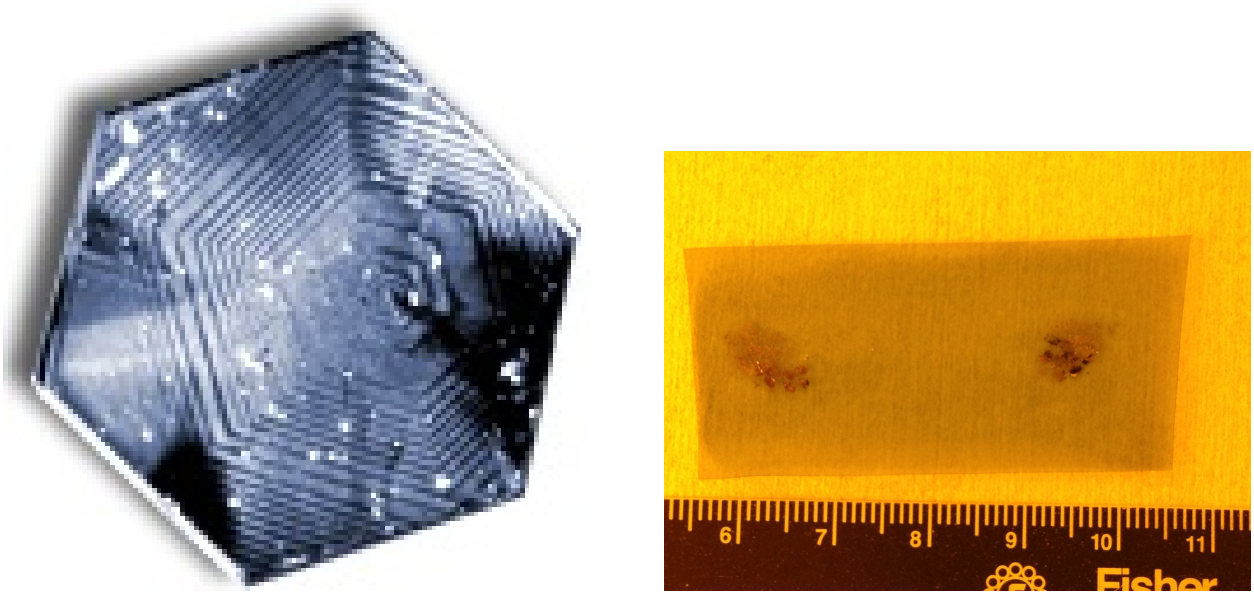

Figure 4.14: Natural graphite and adhesive tape used for exfoliation.

substrate means to heat the graphene when it comes to contact with the substrate, weakening at the same time the bounds between the sheets and the bound between the tape and the graphene. In this way we went from an average $20\times10\mu$m sheets to $60\times40\mu$m.Fig. 4.15. For the natural graphene the optical microscope is not sufficient to determine whether or not we produced a monolayer. From the contrast between the sheet and the substrate, using thin film interference, we can make a rough estimate of the thickness but it is very hard to distinguish between a monolayer and a four layers sheet. So one we think to have produced a very thin film we need to use techniques like AFM or Raman spectroscopy[4].

4.2.5 CVD graphene growth and transfer process

The synthetic graphene used in this work was grown on copper (Cu) foils by chemical vapor deposition (CVD) at ambient pressure. At first the Cu foil was loaded in the CVD furnace and heated the furnace unto 1050 $^{\circ}C$ with continuous flow of argon and hydrogen. The Cu foils are annealed for 20 minutes. Graphene growth was carried out at 1050 $^{\circ}C$ for

[4] I will describe the AFM technique and its results in the section dedicated to the sample characterization.

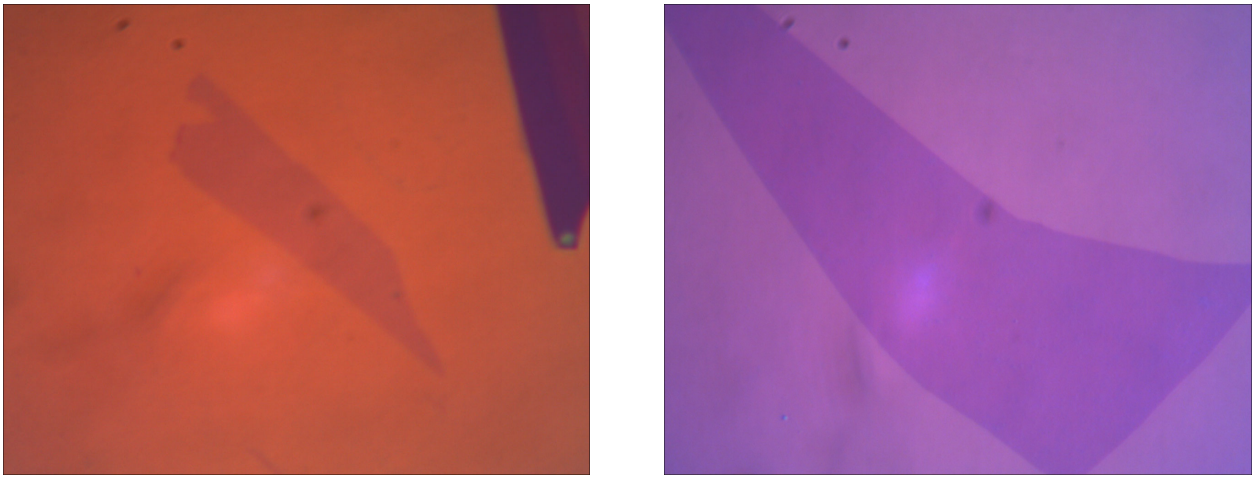

Figure 4.15: On the left we have an image taken at the optical microscope of a graphene sheet of 50x20 μm, on the right we have a picture of a thin graphite sheet composed of eight layers of graphene of 200x30 μm.

two hours under a gas mixture of argon, hydrogen and CH_4. After that CH_4 gas flow was stopped and the furnace was cooled down to room temperature. Then the Cu foil covered with graphene was taken out from the furnace. Finally, the graphene samples are transferred by PMMA assistant process in a Cu etchant (iron nitrate) onto Si substrate (1 mm x 1 mm) covered with SiO_2 of 280 nm, Fig4.16. After the initial step of exfoliation we will treat the two kinds of graphene at the same way, but always remembering that the natural one has extremely high purity and quality [5] but is difficult to handle because of its limited size, while the synthetic one is big enough to be used to built commercial devices. We used the same self-align photolithography technique performed during the construction of the HIGFET. To start we deposited only two current leads on the opposite sides of the sample, in this way we will be able to proceed to the basic characterization of the sample[6]. In the near future we will produce Hall bar shaped graphene using the mask on the right of Fig.4.17, in this way we are going to able to characterize the sample more accurately and to perform Quantum

[5] good for fundamental physics studies

[6] This configuration will be used in the project in which we will built the High-Gain photodetector.

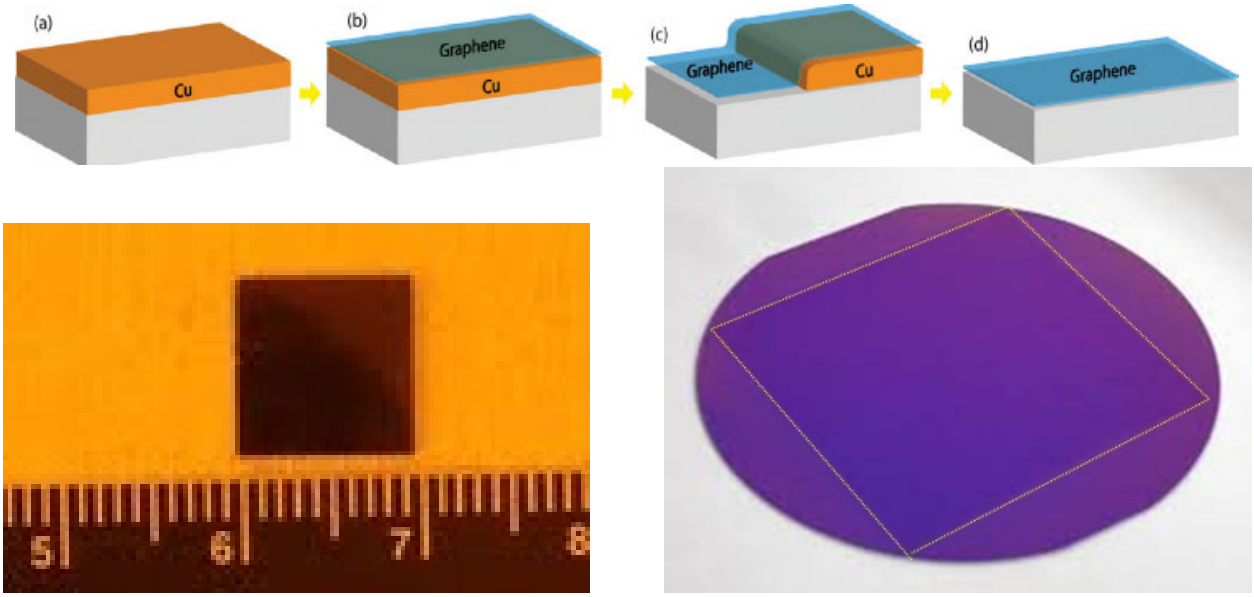

Figure 4.16: Schematic of the CVD process and the 1x1 cm silicon chip covered by a graphene sheet.

Hall Effect measurements.

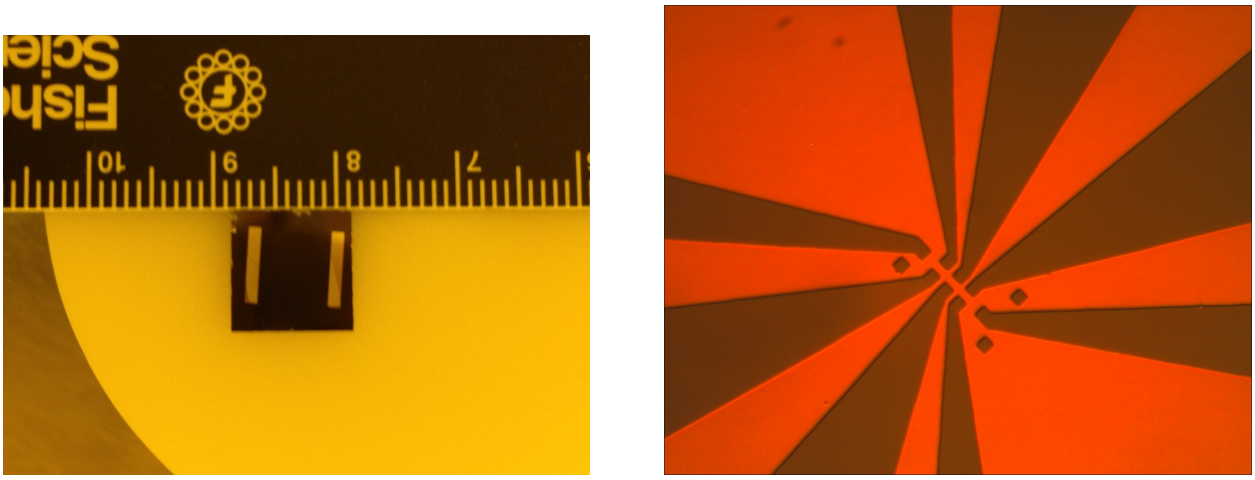

Figure 4.17: Two leads configuration for CVD graphene and one of the Hall bars of different sizes, that we designed to perform QHE and FQHE effects on the natural graphene samples, the one in the picture has dimensions of 50x15 μm.

4.2.6 Graphene morphological characterization

The first kind of characterization that we need to perform when we are dealing with graphene is to determine as accurately as possible its thickness. We already talked about

how sensitive is the electronic band structure to the thickness: a one layer behaves in a drastically different way than a three layers. So it is indispensable to use AFM microscopy and Raman spectroscopy.

4.2.7 AFM

We often used Atomic Force Microscopy to characterize the thickness and the morphology of our sample, Fig.4.19. The AFM consists of a cantilever with a sharp tip (probe) at its

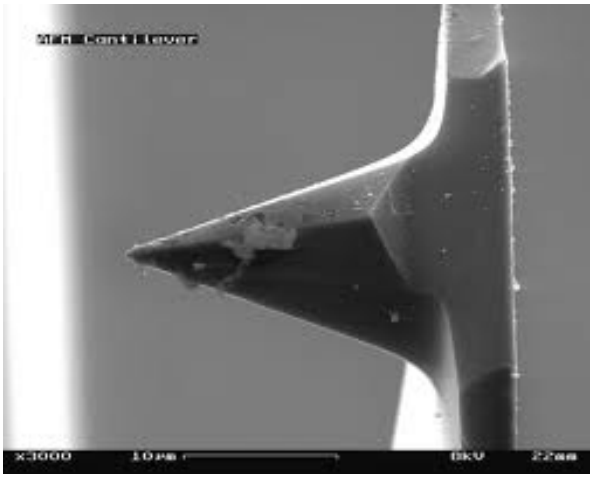

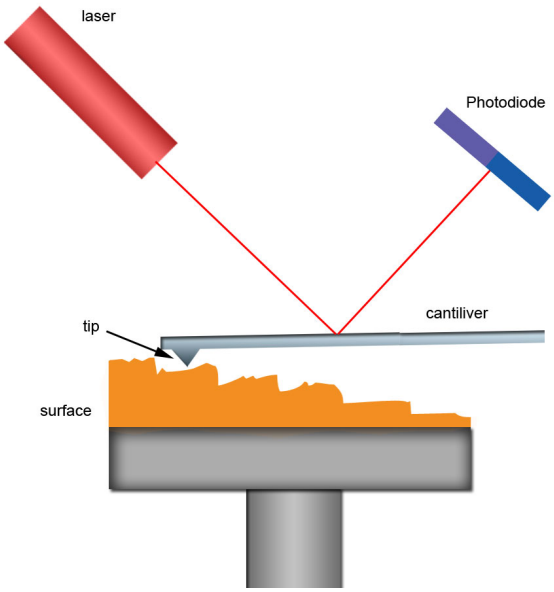

Figure 4.18: A typical AFM tip and the operational scheme of a non-contact AFM [78].

end. The cantilever is typically silicon or silicon nitride with a tip radius of curvature on the order of nanometers. When the tip is brought into proximity of a sample surface, forces between the tip and the sample lead to a deflection of the cantilever according to Hooke's law. Depending on the situation, forces that are measured in AFM include mechanical contact force, van der Waals forces, capillary forces, chemical bonding, electrostatic forces, magnetic forces. We used the AFM in non-contact mode: the tip of the cantilever does not touch the sample surface. The cantilever is instead oscillated at either its resonant frequency or just

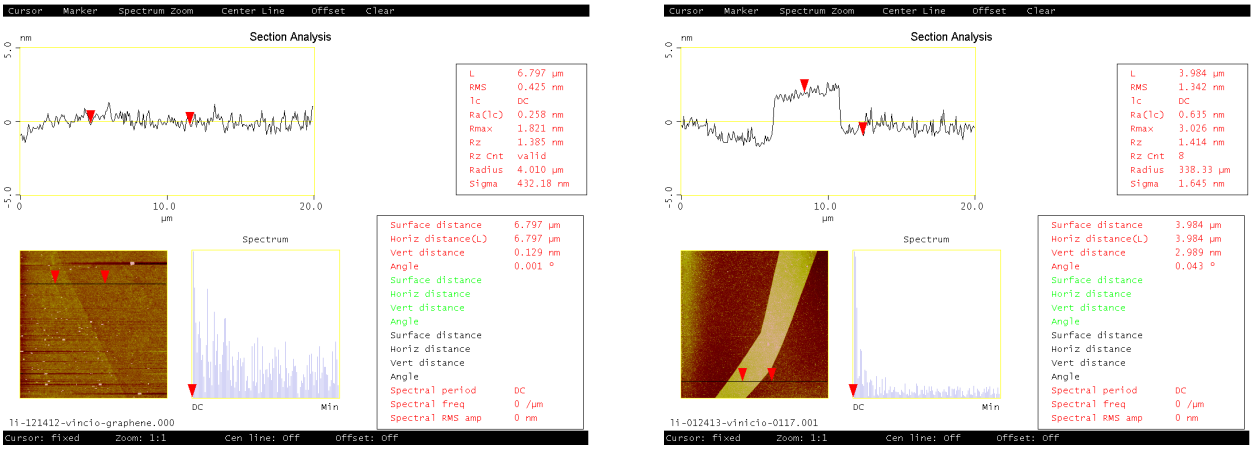

Figure 4.19: A graphene sheet and a eight or nine layers sheet of graphite.

above. The van der Waals forces, which are strongest from 1 nm to 10 nm above the surface, or any other long range force which extends above the surface acts to decrease the resonance frequency of the cantilever. This decrease in resonant frequency combined with the feedback loop system maintains a constant oscillation amplitude or frequency by adjusting the average tip-to-sample distance. Measuring the tip-to-sample distance at each (x,y) data point allows the scanning software to construct a topographic image of the sample surface.Fig.4.18.

4.2.8 Raman spectroscopy

In a few words, a Raman spectroscope works as follows. The light is irradiated on the molecules in the sample and successively gets scattered. Most of the photon experience elastic scattering, no wavelength change, while a small portion of the light is scattered anelastically because of the interaction with the molecules vibrating at their own resonant frequency. This phenomenon is called Raman scattering, and because the resulting shift is different for each molecule and hybridization it is possible to analyze the composition of a sample by analyzing the Raman spectrum. The region of the sample analyzed depends on the cross section of the light beam incident on the sample. A schematic of the Raman

spectroscope is reported in Figure 4.20. Differently for the AFM, Raman spectroscopy is a

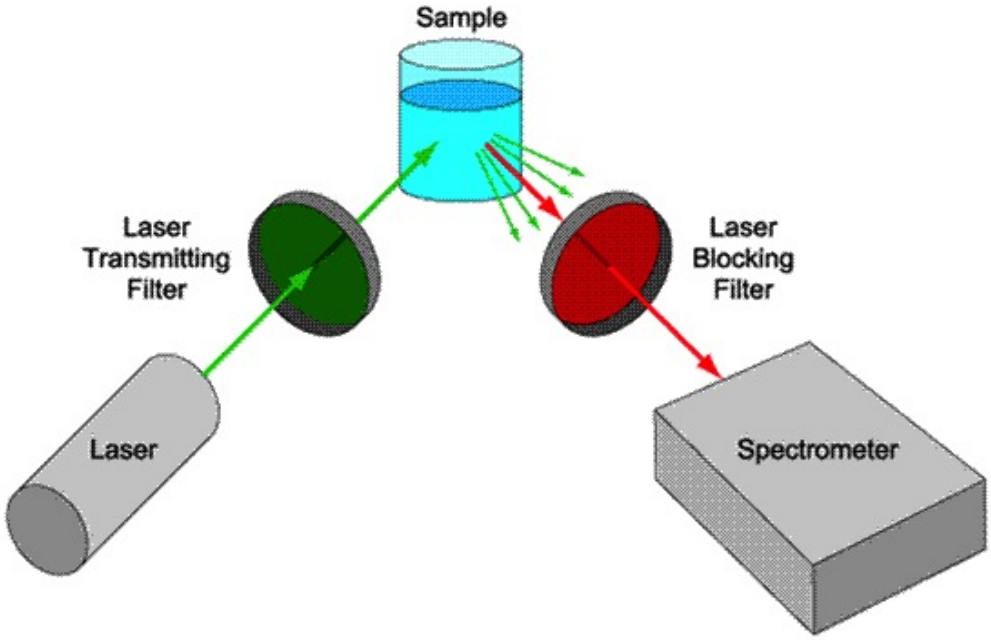

Figure 4.20: Schematic representation of a Raman spectroscope [79].

simple tool that requires little sample preparation. It simultaneously provides information about the number of layers, the hybridization of the carbon atoms with hydrogen, nitrogen or others and about the structure of graphene. In particular, when exfoliating graphite to obtain graphene, an optical microscope is used to discriminate between "few layers" and "many layers" using the color of the sample as a discriminant. Once a promising sample is individuated, Raman spectroscopy is performed to determine if we have produced a monolayer, bylayer or multilayer. The outcome of the spectroscopy will look like one of the spectra shown in Figure 4.21 The difference in these spectra consists in the intensity of the G and G' peaks, also known as G and 2D peaks. The G peak is located at about 1583 cm^{-1}, and is due to E2g mode at the -point. It is representative of the vertical stretching of the carbon-carbon bond in graphitic materials. Its intensity is extremely sensitive to verticala strains

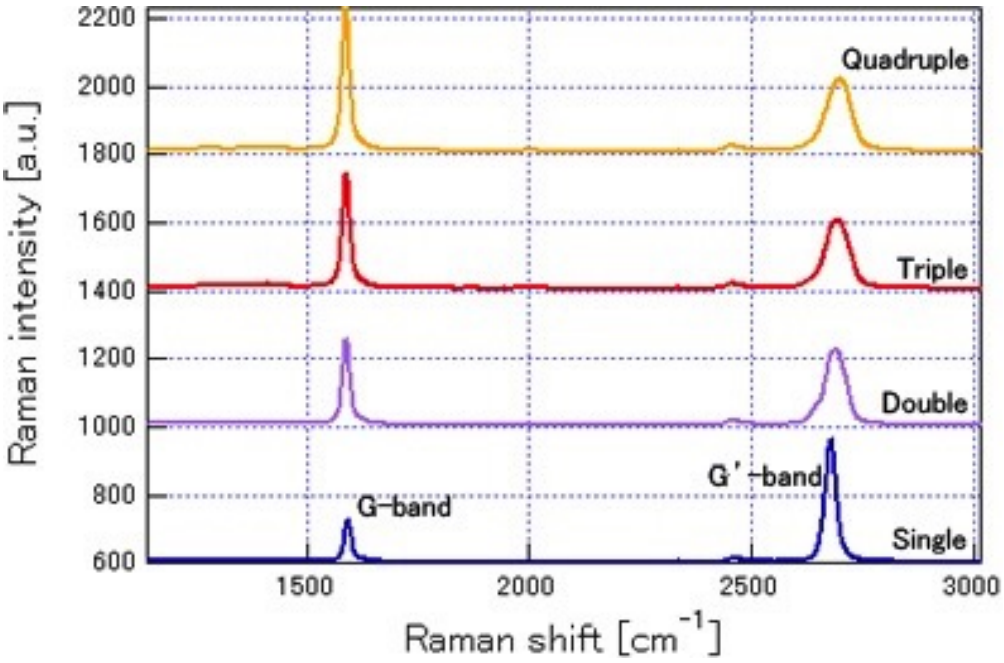

Figure 4.21: Raman spectra for multilayer, bylayer and monolayer [80].

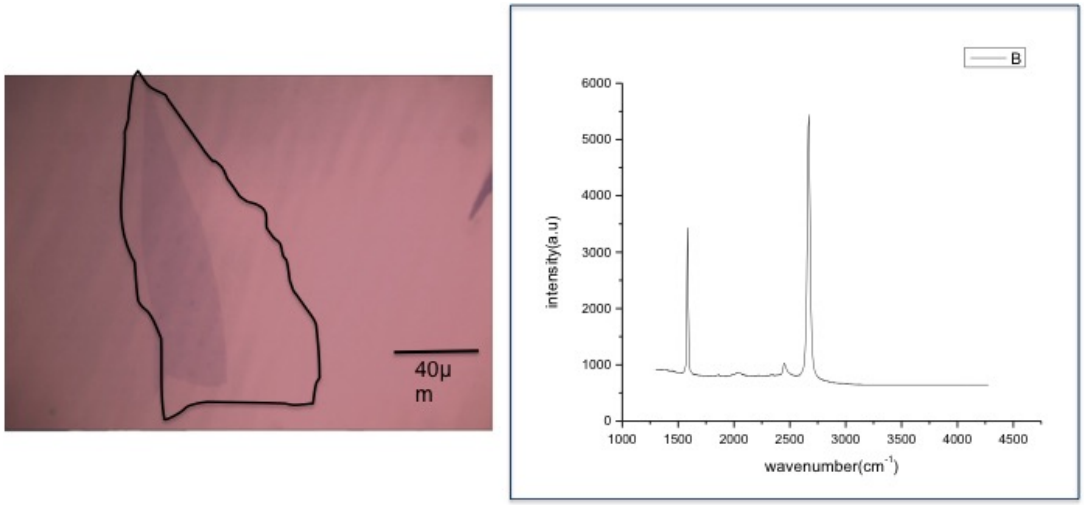

Figure 4.22: Left: Optical microscope image of the sample with a 40 μm bar as a reference. Right: Raman spectrum.

of the sp^2 system. The more intense the peak, the more three-dimensional is the sample. A residual G peak is still present in monolayers because of the surface states between graphene and the substrate and also because of the ripples in the graphene sheet. The 2D band is used to determine the number of layer of graphene. The peak is much more intense of the

G-peak only in monolayers. For bylayers G and 2D have approximately the same intensity and for multilayers the 2D peak becomes smoother and less intense. In Figure 4.22 we report the Raman spectrum obtained for the graphene sample we produced. The 2D peak is much more intense than the G peak, meaning that we have obtained a good quality graphene sheet. At this point we perform a similar fabrication procedure illustrated for the GaAs-based samples and photolithographically deposit metallic contacts on the graphene, in a Hall bar configuration, to investigate the electronic transport.

4.3 Low Temperature Transport Measurement

Ones the fabrication is completed we must transfer our samples to the Low temperature lab to perform the characterization and the electronic transport tests.

The first step is to create the connections between the sample to test and the instruments the we will use to measure its characteristics. We have to complete this procedure in the shortest time possible because we are working in a "non-clean" environment. Before wiring up the sample, we should clean the surface with NH_4OH again to etch away the oxide layer that continuously form on the sample. Then the sample is positioned in mounting station.Fig 4.23. To create the connection between all our measuring technology and the sample we dip the tip of a gold wire in high purity silver paint and attach it on the contacts formed by photolithography. The last step before mounting the sample on the sample holder of the cryostat is to check manually with a digital multimeter if there is any short contact or if we unawareness grounded on of the contacts. Once everything has been checked we can start the measure of the electric characteristics of the sample.

The great part of our measurements is performed at low temperature. We use a *top loading dry dilution refrigerator*, Fig. 4.24. The dilution refrigerator is a very complex and

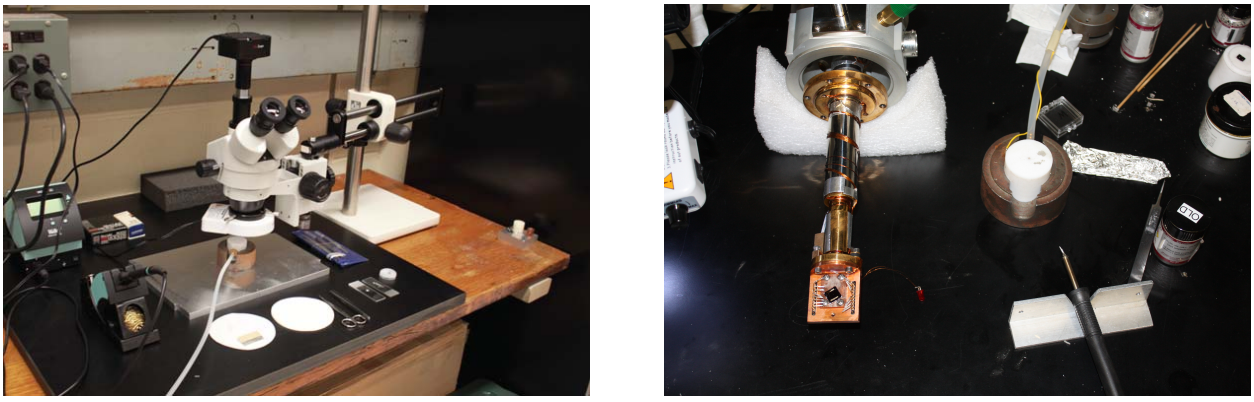

Figure 4.23: The mounting station consists of a microscope, a solder, a mounting chuck connected to a vacuum pump, and some tools for wiring and mounting the sample and the flow cryostat sample holder.

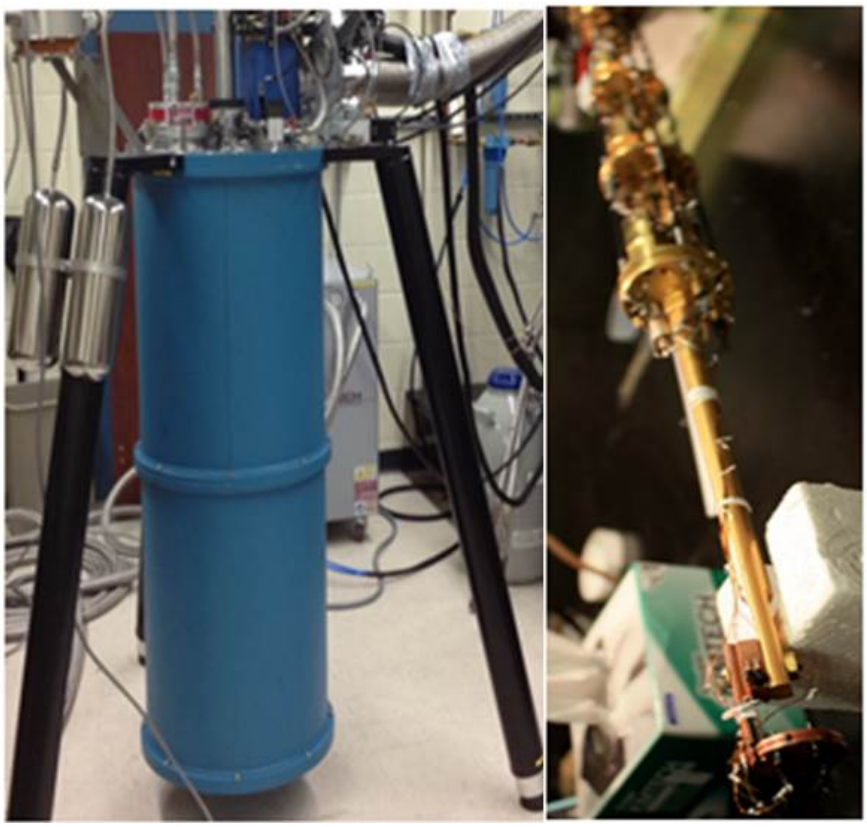

Figure 4.24: On the left we show the dry dilution refrigerator used for the experiments. On the left side a particular of the probe with the sample holder mounted at the bottom.

delicate machine and it usually takes two days to reach the desired temperature. The enormous advantage that this experimental apparatus offers is that it makes possible to go to temperature of a few millikelvin where thermal excitations almost disappear. Also our refrigerator is equipped with a superconductive magnet that can produce magnetic fields up to 9T. The refrigerator is composed of different stages with the temperature that decreases towards the bottom, the superconductive magnet is connected to the still plate at a working temperature of approximately 800 mK, and surrounds the sample. A dilution refrigerator's main feature is also the coldest: the mixing chamber, Fig. 4.25. In this chamber, two phases

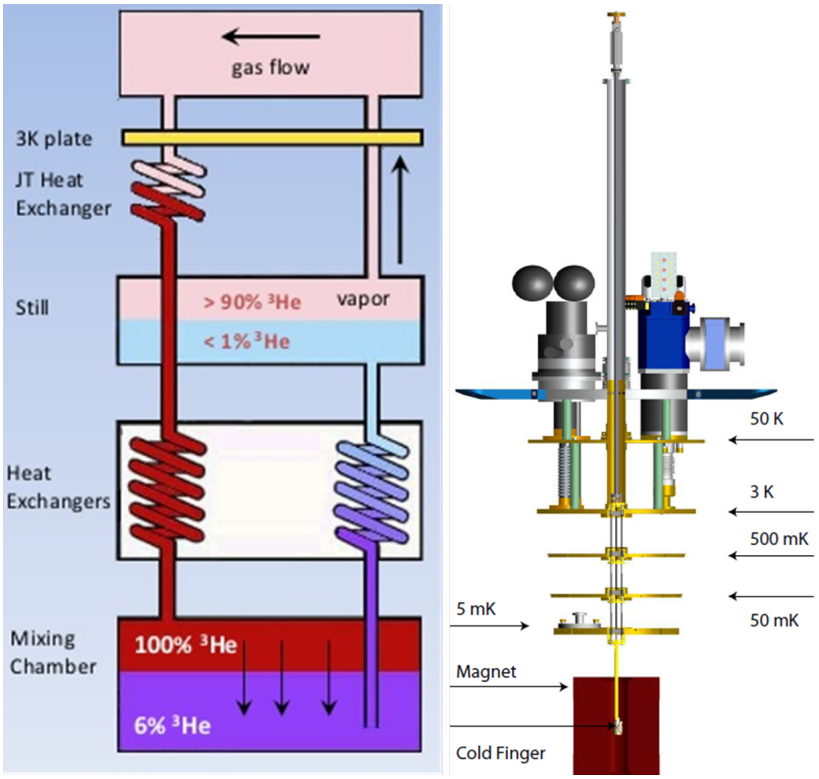

Figure 4.25: Inside structure of the dilution refrigerator with the different temperature stages and a particular of the cooling cycle [81].

of the ^{3}He ^{4}He mixture, the concentrated phase (practically 100% ^{3}He) and the dilute phase (about 6.6% ^{3}He and 93.4% ^{4}He), are in equilibrium and separated by a phase boundary.

Inside the chamber, the ^{3}He is diluted as it flows from the concentrated phase through the phase boundary into the dilute phase. The heat necessary for the dilution is the available cooling power of the refrigerator. The ^{3}He then leaves the mixing chamber in the dilute phase. On its way up, the cold, dilute ^{3}He cools the downward flowing ^{3}He via the heat exchangers until it enters the still. There, the ^{3}He flows through superfluid ^{4}He which is at rest. The pressure in the still is kept low (10^{-2}-10^{-1} mbar) by the turbo-pumps at room temperature. The vapor in the still is practically pure ^{3}He, which has a much higher partial pressure than ^{4}He at 700-800 mK. The pump therefore creates an osmotic pressure difference, which drives more ^{3}He up from the mixing chamber to the still. Heat can be supplied to the still to maintain a steady flow of ^{3}He. The pumps compress the ^{3}He to a pressure of a few hundred millibar and feed it back into the cryostat, completing the cycle. With the sample thermally anchored to a cold finger effectively so that no significant Kapitza resistance occurs down to 20 mK. Our system is equipped with an red LED that can be used to equilibrate the population of the 2DHG. Also, we installed a thermometer and an heater on the copper sample holder so that is possible to precisely vary the temperature of the system to perform temperature-dependent measurements.

The numerous electronic devices available in our low temperature laboratory allows us to carry out a wide spectrum of transport measurements. We built a low-pass filters array to shield the sample and the coldest region of the fridge in general from any kind of high frequency noise deriving from the environment and the instruments themselves. The magnetoresistance (ρ_{xx}) and the Hall resistance (ρ_{xy}) are obtained with a four-probe AC lock-in technique with a 10 nA excitation at low-frequencies 7 and 13 Hz. DC and DC+AC techniques are also employed for the differential resistance measurement across the inner

and outer edges to investigate the breakdown of the QHE. The transport techniques will be examined more in depth during the discussion of the experimental results.

Figure 4.26: PPMS used for the graphene characterization.

Graphene electronic characterization is performed using a PPMS (Physical Property Measurement System) cryostat [Fig. 4.26] that allows us to continuously probe the electronic properties of the sample from room temperature, 292 K, to liquid Helium temperature, 4 K. The PPMS is equipped with a superconductive magnet, that we will utilize to perform quantum Hall effect measurements on graphene up to 7 T.

CHAPTER 5 RESULTS AND DISCUSSION

This chapter discusses our experimental results on the study of low-density 2D systems in the QHE. The first section is dedicated to the characterization of the system. The degeneracy and effective mass in the Valence Band of 2D GaAs Quantum Well Systems are investigated; these results have been published by our group on Applied Physics Letters in 2014 [82]. The second section investigates deeper in the subject of the correspondence between edge states and bulk, discussing a novel Hall potential distribution and asymmetric breakdown process, (the results are soon to be submitted for publication). The third is dedicated to QHE and applications in graphene-based devices performed in collaboration with other members of the Quantum Transport Group. The electronic transport measurements have been performed using lock-in amplifiers as current-voltage source as well as meter. Coaxial wires and proper low-pass filtering have been used to decrease the noise from the environment. Pre-tests at T≈3 K have been performed to study the quality of the ohmic to the 2DHG. Both AC and DC+AC have been performed at base temperature as shown in Figure 5.1.

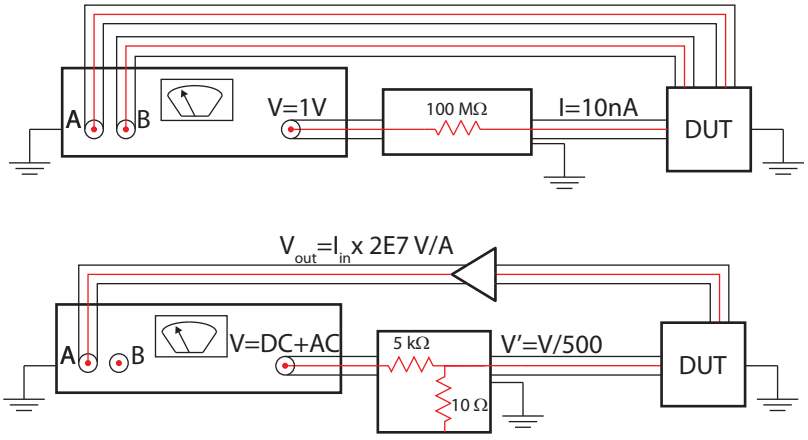

Figure 5.1: Schematic of the measurement configuration for (top) AC four-probe measurement using current drive and (bottom) DC bias superimposed to AC perturbation to explore the energy excitations of the system.

5.1 Degeneracy and Effective Mass in the Valence Band of GaAs QW

The 2DHG we utilized in our study are characterized by high purity and very low carrier density. This systems can be used as laboratories for the investigation of strongly correlated phenomena [1–3] as well as for spintronics [4] and device applications. The carriers in this systems (holes) are are characterized by a much larger effective mass (m^*) than electrons which leads to an enhanced interaction effect as shown through the interaction parameter $r_s = (m^*e^2)/(4\pi\hbar^2\epsilon)(p\pi)^{-1/2}$, the ratio of Coulomb and Fermi energy [3]. To determine the exact values for m^* is difficult, especially in the low density, strongly-correlated regime where splitting and mixing of the bands and interaction effects yield a complex band structure with non-parabolic dispersion [5]. Also the shape and the relative position of the sub-bands depend on parameters that are inherent to individual samples: depth, width, direction and symmetry of the QW.

We have realized a high purity 2DH system that allows us to maintain very high carrier mobility, $\mu \sim 2{\times}10^6$ cm^2/(V·s), while reaching a low density range: $4.3{\times}10^{10}$ cm^{-2} $\leq p \leq 4.8{\times}10^{10}$ cm^{-2}. This makes it possible to analyze the low-field Shubnikov-de Haas (SdH) oscillations and directly obtain information on m^* and the band structure. The results complement previous studies of low density m^* measured via cyclotron resonance method in magnetic fields around $\sim$ 0.5 T [83].

The samples used are 20 nm wide p-GaAs quantum wells grown in the (100) direction. The wells sit 360 nm below the surface with a double-sided carbon doping. The devices are 3x1 mm Hall bars defined by photolithography and the Ohmic contacts are made with a thin film deposition of 160 nm of AuBe (1%) annealed at 420 ^{o}C. The contact resistance

for all leads is consistently ∼400 Ω at 10 mK. We performed the measurement in a dilution refrigerator where the sample is thermally anchored to a cold finger. The magnetoresistance (ρ_{xx}) and the Hall resistance (ρ_{xy}) are obtained with a four-probe AC lock-in technique with a low-frequency ($\leq$ 13 Hz) excitation $\leq$ 10 nA. The mobility is $\mu = 2.0 \times 10^6$ cm^2/(V·s) for a density $p = 4.3{\times}10^{10}$ cm^{-2} for sample A and $\mu = 1.9{\times}10^6$ cm^2/(V·s) for $p = 4.8{\times}10^{10}$ cm^{-2} for sample B. μ and p are calculated using $\mu = 1/(\rho_{xx} pe)$ and $p = 1/|e|\,(\partial R_{xy}/\partial B)^{-1}$.

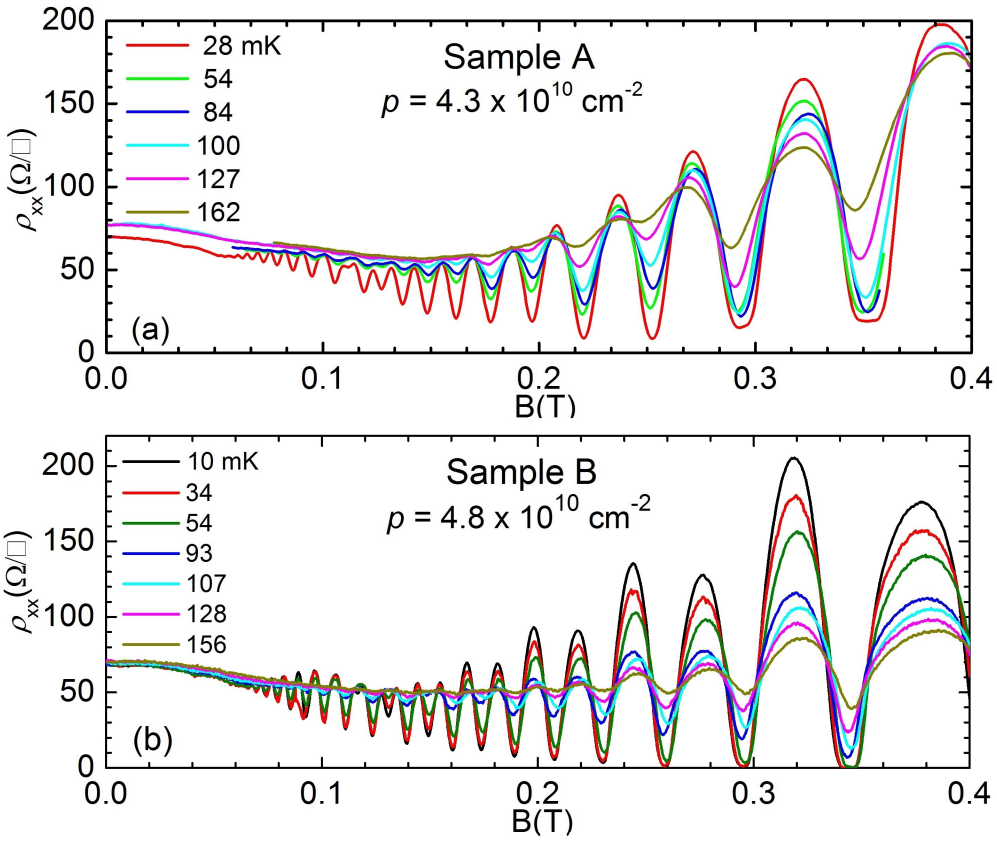

Figure 5.2: T-dependence of SdH oscillations for sample A and B respectively with p=4.3×10^{10} cm^{-2} and p=4.8×10^{10} cm^{-2} [82].

Figure 5.2 shows the SdH oscillations for both samples at various T between 10 and 160 mK. The oscillations are well defined even in the low field starting from 0.06 T, indicating the high quality of both samples. SdH oscillations are periodic vs. $1/B$ with a period of $\Delta\,(1/B) = e/h \cdot (g_s/p)$ being g_s the spin degeneracy. Fig. 5.3, where the longitudinal

resistance ρ_{xx} is plotted against $1/B$, shows a distinctive periodic pattern between 0.06 T and 0.3 T. The Fourier analysis is performed for each curve in the region where $B < 0.11$ T, field beyond which the Zeeman splitting becomes observable. The spectra are shown in the insets of Fig. 5.3. The spectra reveal single peaks located at f=0.94 T and f=1.03 T

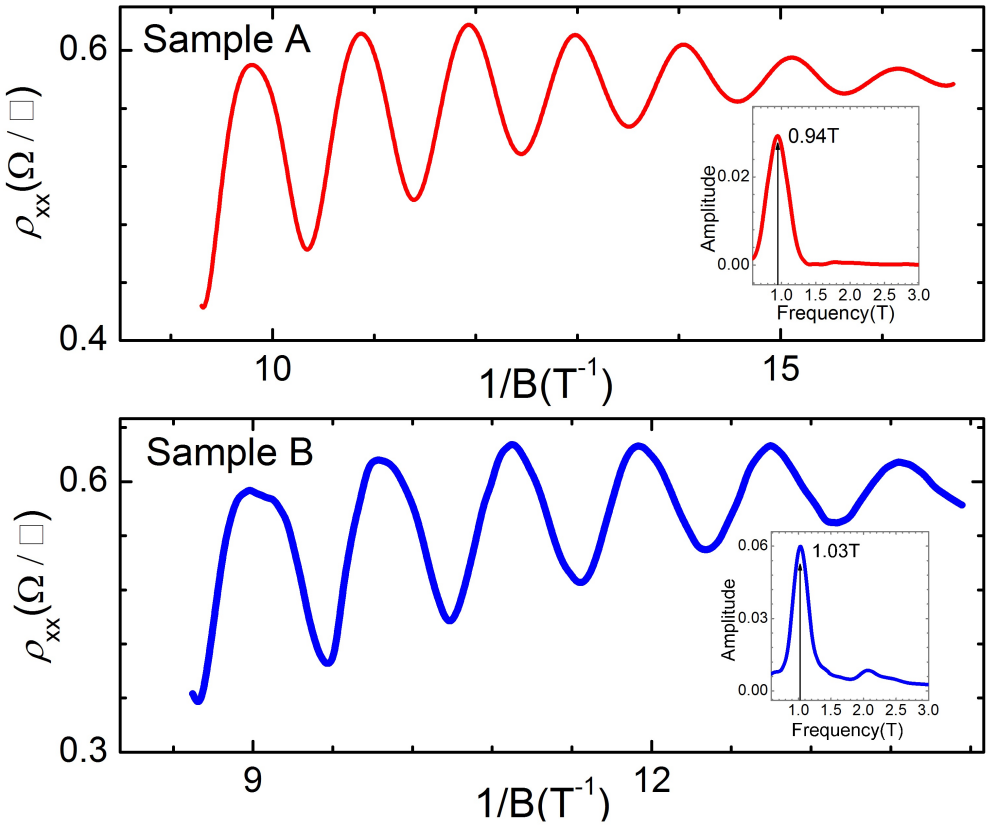

Figure 5.3: Observed SdH oscillations for the two samples, A and B, in the range between 8.5 T^{-1} and 15 T^{-1}. In the insets are shown the Fourier spectra of the oscillations, the dominant peaks and their frequencies values [82].

respectively for samples A and B. To interpret these results, it is important to discuss the structure of the valence band. It is well known that in GaAs/AlGaAs heterostructures the lack of inversion symmetry of the underlying zinc-blende structure of the GaAs gives rise to Spin-Orbit interaction (Bulk Inversion Asymmetry, BIA) so that the holes populate the higher valence band with total angular momentum $j = 3/2$ [84]. As discussed in previous

theoretical [85] and experimental papers [86–88], the confinement potential unfolds the degenerate $j = 3/2$ band into Heavy (HH) and Light hole (LH) subbands respectively with z component of the total angular momentum $j_z = \pm 3/2$ and $j_z = \pm 1/2$; the terms heavy and light refer to values of m^*. The interaction between the spin of the carriers and electric field created by the asymmetry of the confinement potential further lifts the spin degeneracy and creates the HHh (heavier HH) and HHl (lighter) sub-bands. This effect, called structural inversion asymmetry (SIA), increases with increasing hole density and the asymmetry of the confinement potential [84], [89]. The interplay of these energies creates the band structure schematically represented in Figure 5.4 . The extensive study of heterostructures and quan-

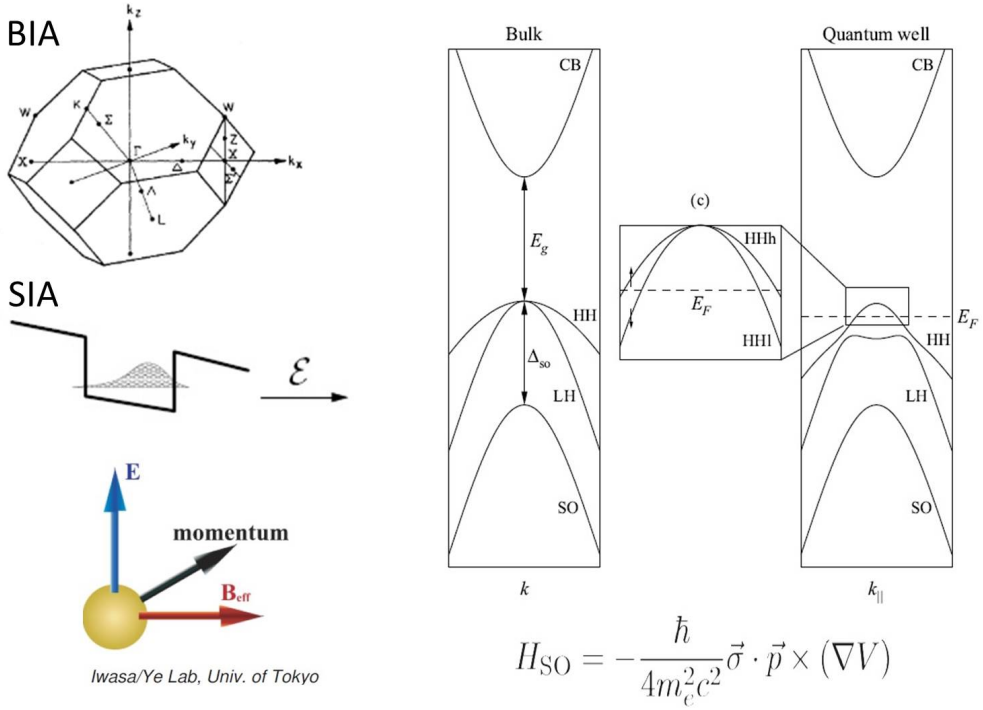

Figure 5.4: Schematic representation of the effects of the BIA and the SIA on the band structure of the 2DHG inside the quantum well. [84].

tum wells grown on (311)-GaAs demonstrated that, because of the lack of symmetry, the SIA effect is strong enough to produce an observable HHh-HHl splitting for p$\gtrsim$7$\times$10^{10} cm^{-2} [90].

The lift of the degeneracy is deduced from the Fourier spectra of ρ_{xx}-$1/B$ which shows four distinct peaks: the two main frequencies f_+, f_- and their average and sum, f_{ave}, f_{sum}. f_+ and f_- correspond to the densities p_+ and p_- that are the populations of the HHh and HHl [87]. The SOI-induced spin splitting is reduced if the confinement potential becomes more symmetric as confirmed by previous studies [91] of 2DHS in nearly symmetric (100) QWs, reporting an onset of the splitting at much higher carrier densities $\sim 2\times10^{11}$ cm^{-2}. In the density range that we are exploring, a degenerate scenario is expected. This anticipation is confirmed by the Fourier analysis shown in Fig. 5.3. The characteristic frequency f for each curve corresponds to a carrier density through the formula $p = (g_s e/h)f$. Consistently for both samples, the densities calculated, 4.5×10^{10} cm^{-2} and 4.9×10^{10} cm^{-2}, agree very well to the ones measured through the Quantum Hall method assuming g_s=2. So, the HH band is still two-fold degenerate, indicating that the nearly symmetric confinement potential in this low p range, provided through symmetrical double-sided doping, further weakens the effects of the SOI. This result addresses the lack of documentation for the (100) case for the low p QW systems which was technologically challenging due to the sample quality. These SdH results also complements well the cyclotron method, which was used to measure m* for dilute 2DHs, in terms of providing both m* and the band information.

m* can be obtained by studying the T-dependence of the SdH oscillations. In Fig. 5.2, the T-dependence is clear even at small fields and the systems have a metallic behavior at zero field, ρ_{xx} $\sim$70$\Omega/\square$. Ando's formula defines the relation between the variation of ρ_{xx} and T [92]:

$$\rho_{xx}(B) = \rho_{xx}(0)\left[1 - 4\cos\left(\frac{E_F}{\hbar\omega_c}\right)\cdot D(m^*,T)\cdot E(m^*,\tau_q)\right] \tag{5.1}$$

where $\rho_{xx}(0)$ is the longitudinal resistivity at zero field; E(m^*,τ_q) - an exponential term that depends on the quantum scattering time τ_q and the cyclotron frequency ω_c=eB/m^*, E(m^*,τ_q)=exp($-\pi/\omega_c\tau_q$); and D(m^*,T) - the Dingle factor that in the low magnetic field limit D(m^*,T)=ξ/sinh ξ with ξ=$2\pi^2$k$_B$T/$\hbar\omega_c$ [93]. In the temperature region that we are exploring, it is possible to make the approximation for which ln(sinh ξ) $\sim$ ξ, allowing simplification to Eq. (5.1). Now, m^* can be extrapolated from the linear relation between the logarithm of the ratio of low field oscillation amplitude and T itself:

$$\ln\left(\frac{\Delta\rho_{xx}}{T}\right) = C - \frac{2\pi^2 k_B}{\hbar e B} m^* T \tag{5.2}$$

The data are fitted using Eq. (5.1) with an R^2 $\geq$ 0.995. m^* is calculated from the slope of

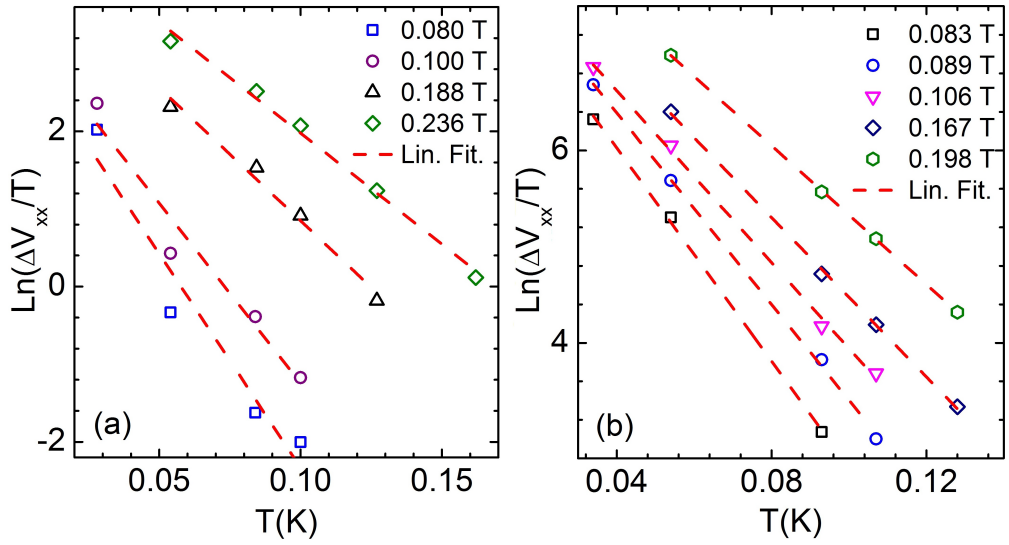

Figure 5.5: Variation of the logarithm of the longitudinal resistance with the temperature and its fit with the Dingle factor for different magnetic fields for respectively sample A (a) and sample B (b) [82].

the lines in Fig. 5.5 for each value B. We note that the calculation is performed by using the approximation to Eq. (5.1) for T from 25 mK up to 200 mK beyond which the SdH

oscillation are smeared by the thermal energy. Fig. 5.5 shows that the linear relationship in Eq. (5.2) have slightly different slopes at different magnetic fields, demonstrating that the strength of the field affects the value of m^* as shown in Fig. 5.6. The causes of this effect,

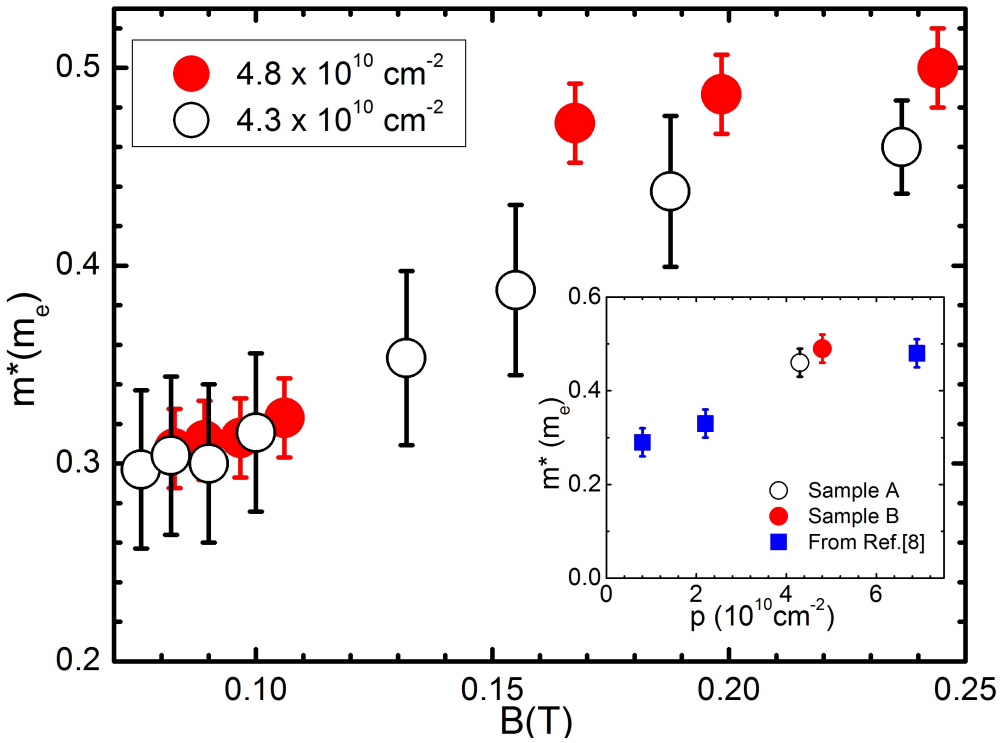

Figure 5.6: In the graph are reported the values of m^* in units of m_e in the range 0.080 T$\leq$ $B \leq$ 0.236 T for both samples. In the inset, our results are compared to previous data obtained through cyclotron resonance measurements [83], using the m^* values corresponding to B=0.25 T, that is the closest to the field applied in the cited experiment [82].

already observed previously [87], [94], arise from the complex relation between B, kinetic energy, and many body interaction in the HH band that we do not intend to address in this work. The values of m^* for $B > 0.107$ T are also affected by the Zeeman effect, that can be better studied in parallel fields. For sample A we found that m^* varies from a value of 0.30m_e at B=0.076 T to 0.47m_e at B=0.250 T and for sample B the mass ranges from 0.31 to 0.50 m_e. The observation of a single set of m^* for each sample confirms that the HH band is still degenerate in our range of densities. It is evident that m* in sample A (lower

density) is constantly smaller than the one measured for sample B. The increase of m^* with increasing density has already been observed using the cyclotron resonance method and our results are in good agreement with the previous findings [83], in the inset. The dependence of m^* on p can be explained by considering that in our range of densities the $e-e$ repulsion (Hartree potential) does not contribute much to the Hamiltonian. So we can safely say that the change in density only shifts the position of the Fermi energy of the 2DHS while the magnitude of the spin-orbit splitting stays nearly constant. For in-plane motion, the HH band presents a smaller m^* than LH band. This demonstrates that the density decrease causes the Fermi energy to move away from the anti-crossing point, consequently making m^* decrease [83]. These findings agree with the m^* values calculated in earlier papers [5], [83].

5.2 Bulk-edge dynamics and step-like breakdown of the QHE

At this point we know that the valence band is still degenerate for the density range considered in this work. Also we estimated the effective mass of the holes. This information will be useful for the investigation of Hall system presented below.

The integer and the fractional quantum Hall effects (IQHE [6] and FQHE [7]) play essential roles in exploring quantum matters characterized by topological phases. The one-dimensional (1D) chiral edge channels of a quantum Hall (QH) system are maintained dissipationless via the broken time reversal symmetry and, as a defining requirement of topological insulator (TI), they are in 1-1 correspondence to the gapped incompressible bulk states characterized by non-trivial topology (or Chern number) [9]. Understanding this correspondence in real systems, especially its robustness in terms of the limit of breakdown, is important both fundamentally and practically (i.e. in relation to spintronics [4]). However, the breakdown mechanism, especially in light of the edge-bulk correlation, is still an open question.

Experimental probes to the breakdowns usually rely on the onset of the non-zero magnetoresistance (MR) and distorted Hall resistance [10], measured via electrical probes located on the same physical edge, when a Hall bar system is subjected to sufficiently large bias. However, the results are inconsistent with the theoretical models based on mixing of the Landau levels (LLs), i.e. through Umklapp scatterings either via phonons or impurities [11–18]. These criteria may not be rigorous since the complete picture requires also the dynamical information of the bulk. The edge dynamics, including the important edge reconstruction [19, 20], has been extensively studied through experiments on edge-edge equilibration [21, 22], scattering in quantum point contact [23], and edge channel reflection [24, 25]. On the other hand, the bulk dynamics studies, such as with the Corbino geometries [26, 27], have not yet succeeded providing a clear edge-bulk correlation, especially to the point of breakdown [28, 29].

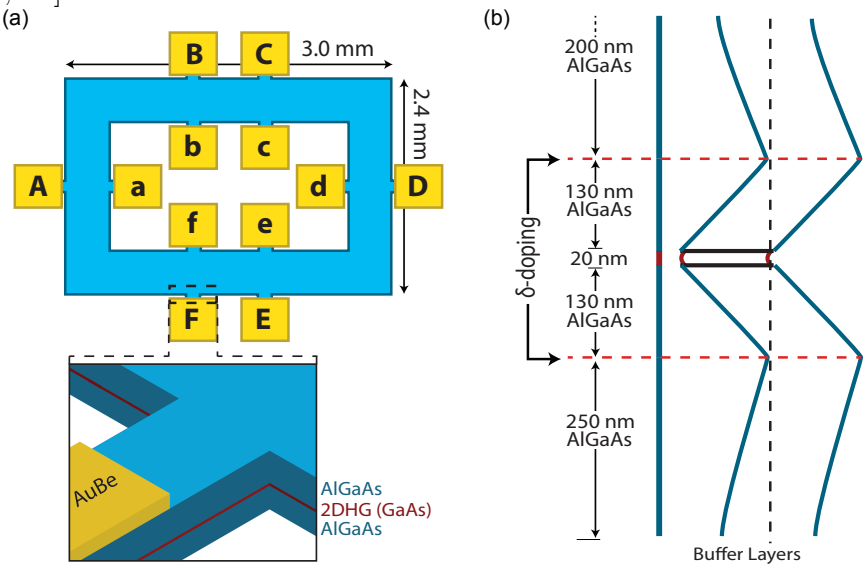

Figure 5.7: (a) Anti-Hall bar schematics with a 2 mm×1.5 mm window in the center with labeled electrical contacts. A 3D cross section of the GaAs/AlGaAs quantum well is also shown. (b) The band diagram showing symmetric δ-doping.

We adopt an ultrahigh quality 2D holes systems patterned into an anti-Hall bar geometry

illustrated in Fig. 5.7(a) where, analogous to the Corbino geometry, an extra set of edge, referred to as inner edge, is formed. The bulk dynamics is then measured between the inner and the outer edge simultaneously with the measurement of the MR ρ_{xx} and the Hall resistance ρ_{xy}. This modification preserves the topological invariant precisely as to a regular Hall bar for the same filling factor (ν). The onset of the breakdown probed by voltage biasing the inner edge relative to the outer edges reveals an extremely sharp threshold beyond which a series of discontinuous steps, spaced at exactly the LL spacing $\hbar\omega_c$, manifest. It suggests a resonant-like tunneling mechanism across the dynamically varying incompressible edge strips when the alignment of the edge LLs to the bulk LLs takes place. In addition, the formation of the chiral edge channels proceeds the fully gapped bulk which occurs only within a small window. The rising and falling of the gapped bulk states leads to a novel 0-1 Hall voltage distribution: approximately zero voltage drops across one arm and the whole Hall voltage ($h/(\nu e^2 I)$) drops across the other arm.

The samples are p-doped (100) GaAs/AlGaAs quantum well structures with a well width of 20 nm. The anti-Hall bar configuration, shown in Fig. 5.7(a), is photolithographically defined with shown dimensions. Ohmic contacts are realized via AuBe alloy deposited on both inner and outer edges (as current and voltage leads) and annealed at 420 ^{o}C. The contact resistance is determined to be $\sim$400 Ω consistently for all leads at low T. The measurement is performed in a dilution refrigerator where the sample is thermally anchored to a cold finger so that no significant Kapitza resistance occurs down to 30 mK. The magnetoresistance (ρ_{xx}) and the Hall resistance (ρ_{xy}) are obtained with a four-probe AC lock-in technique with a 10 nA excitation at frequencies around 7 Hz. The carrier density determined by the Hall measurement is $p \sim 4.2\times10^{10}$ cm^{-2} with a carrier mobility of $\mu = 2.3\times10^6$ cm^2/(V·s). Elec-

trometer level DC and DC+AC techniques are also employed for the differential resistance measurement of the gapped bulk states between the inner and outer edges.

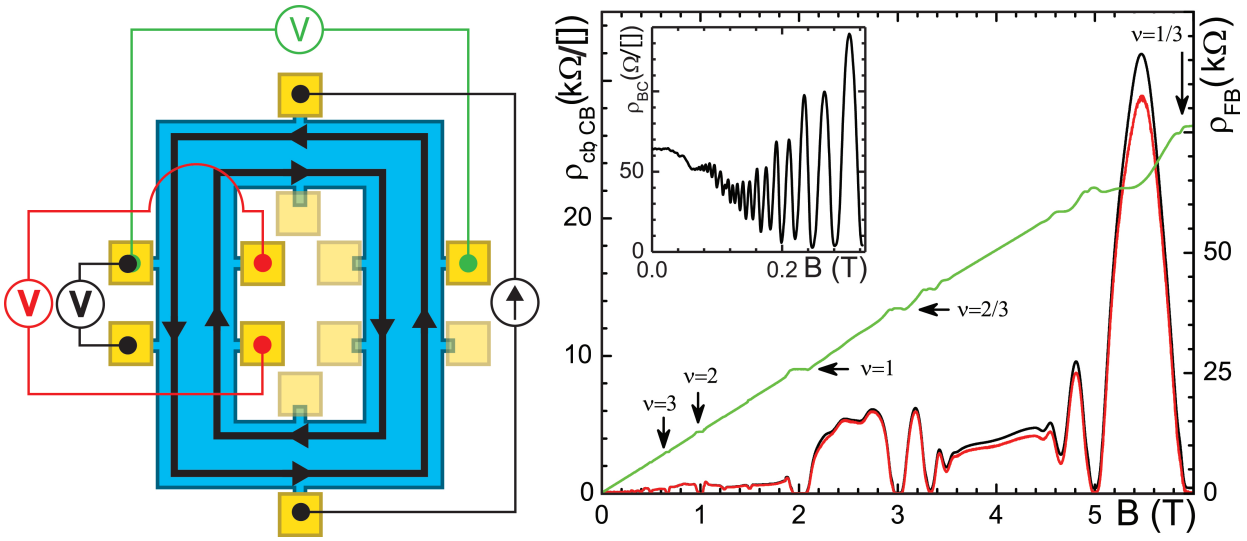

Figure 5.8: Hall measurement performed on the p-type sample, where the green line represents the Hall resistance across the Hall bar using the contacts F-B and the black and red lines are respectively the magnetoresistance in the Hall bar and anti-Hall bar measured at C-B and c-b. The B-field is ranging between 0 and 6 T. The source of the current is D and A is grounded. The inset shows Shubnikov-de Haas oscillations of the magnetoresistance. The early inset of the oscillations highlights the high quality of the hole system characterized by an effective mass of approximately 0.5 m_e [82].

First, Hall measurement is performed to obtain the MR for both outer and inner edges. The measurement setup is shown as the inset of Fig. 5.8 where the current is driven from outer current leads (D→A) while measuring the ρ_{xx} along the outer and the inner edges. Also in the inset are the high quality Shubnikov-de Haas oscillations (SdH), starting around 0.05 T. The overall MRs measured along outer and inner edges (B-C and b-c) are identical and they bear no variation compared to a regular Hall bar situation. So it is with the Hall resistance $\rho_{xy} = \nu^{-1}h/e^2$ via C-E [Fig. 5.8]. The inner edge is found to be at equal-potential within the QH plateau as long as the current is driven from the outer edge. Reciprocally, when driving a current along the inner edge, the outer edge becomes equal-potential and ρ_{xy}

between c-e bears the regular Hall resistance. Fig. 5.9 shows the resistivity across the outer

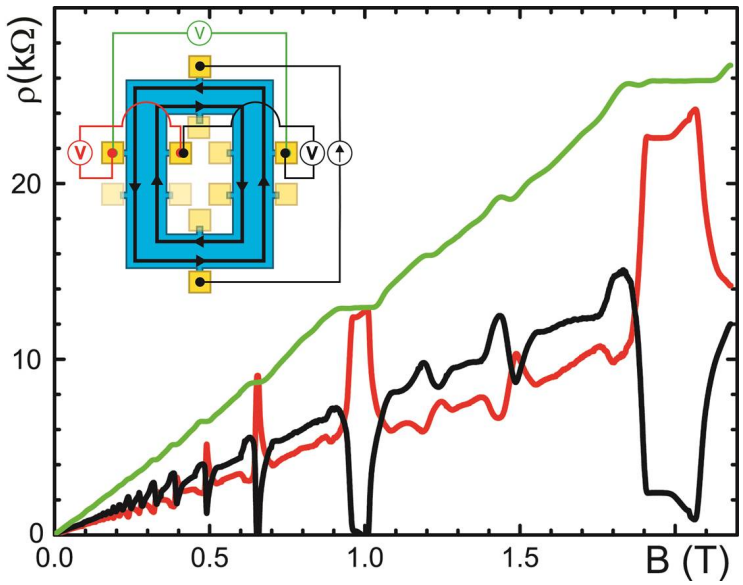

Figure 5.9: (a) Potential drop in the direction perpendicular to the current drive across the device. The color coding is blue for the Hall potential ρ_{EC}, black for ρ_{cC} and red for ρ_{Ec}. In the inset we show the experimental configuration.

and the inner edges measured during the Hall sweep (with a current driven from the outer edge) for both upper (ρ_{Cc}) and lower arms (ρ_{eE}) and the results are shown in comparison to the Hall resistivity. Outside the Hall plateaus, the bulk voltage drop is roughly evenly divided between the upper and lower arms since $V_{Cc} \sim V_{eE}$. However, as the system approaches the center of a Hall plateau, V_{Cc} and V_{eE} undergo dynamical changes that results in a drastic imbalance: $V_{Cc} \to 0$ and $V_{eE} \to \nu^{-1} Ih/e^2 = I\rho_{Hall}$. The inner edge becomes approximately equipotential with the upper outer edge which is grounded, while nearly the whole Hall voltage drop is now only across the lower arm. Thus, the net current in the upper arm is approximately zero and the I_{drive} is then the net current in the lower arm. This imbalanced potential distribution can be figuratively described as a 0-1 distribution with 0 for the upper arm and 1 for the lower arm. We demonstrate that the 0-1 imbalance can be inverted into

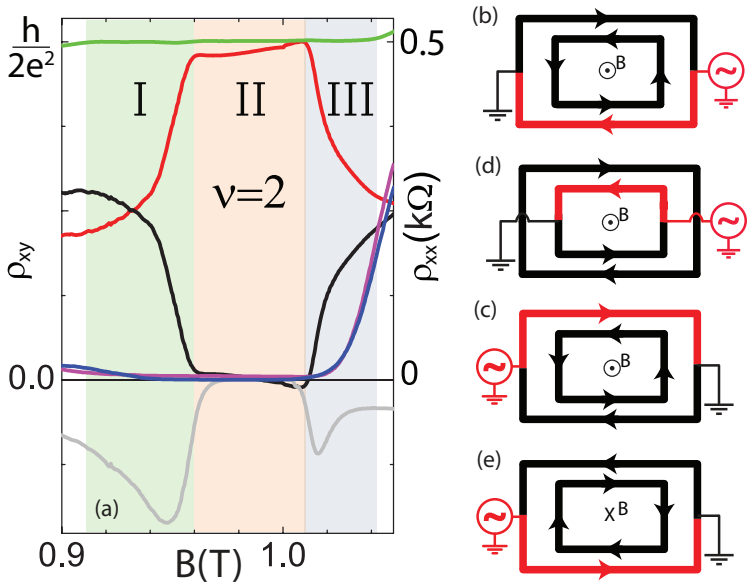

Figure 5.10: (a) Detailed results around $\nu = 2$, divided in three regions, where the transverse resistivity across the upper and lower arms are plotted together with the MRs and the Hall resistance. (b-e) Situation at the center of the plateaus for different source-drain configurations and B-field direction. Black represents the ground potential while red the driven one. Arrows show the direction of the skipping orbits. From b) to e) D→A, A→D, d→a and A→D with flipped B-field.

1-0 by simply switching the source and drain (grounded) or by inverting the direction of the B-field. Fig. 5.10(c) shows the situation with D grounded and A as the source. The measured potential is completely inverted: the Hall potential is now bore by the upper arm and the inner edge is at equal-potential with the lower outer edge. Flipping the direction of the B-field results in reversed chirality of the edge channels which causes the upper outer edge to be grounded. The voltage distribution is also inverted as shown in Fig. 5.10(e). In addition, with current driven through the inner edge from d to a (grounded), the outer edge becomes equipotential and aligns to the grounded lower inner edge [Fig. 5.10(d)].

The 0-1 (or 1-0) distribution of the transverse voltage though the bulk is qualitatively understood through the dynamical rising and falling of the gapped bulk states, from mixed to fully gapped, as a function of the B-field (or ν) which we divide into three segments. As

shown in Fig. 5.10(a) for the $\nu = 2$ plateau, stabilized $\rho_{xx} = 0$ and $\rho_{xy} = h/2e^2$ indicate that the chiral edge channels are first developed. Starting from B=0.9 T in segment 1, the bulk resistance in the upper and lower arms are still approximately even, $\rho_{Cc} \sim \rho_{eE}$, indicating a bulk that is not (at least not rigorously) gapped. With B increased towards 0.95 T, $\rho_{Cc}(B)$ and $\rho_{eE}(B)$ vary rapidly in opposite trends and settle at $\rho_{Cc}(B) \to 0$ and $\rho_{eE}(B) \to h/2e^2$. Note that terminal A is grounded, the upper edge potential is then zero due to the dissipationless chiral edge (following Buttiker's picture [54]). As the driven AC current populates/depopulates the lower outer edge by raising and lowering the E_F within, the inner edge potential follows as long as the bulk is not fully gapped. Such a non-fully gapped liquid can not sustain significant voltage drop. Instead, the Hall voltage is mainly distributed in the incompressible strips along the edges. This could help to explain some of the STM [95] results showing major Hall voltage drop at the edges, Figure 5.11.

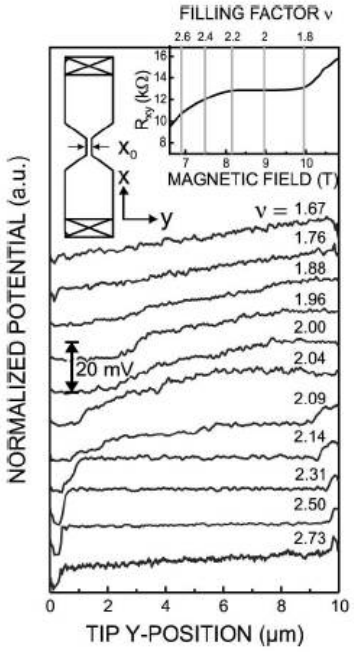

Figure 5.11: STM scanning of the quantum Hall voltage profile across a 10 μm wide Hall bar. [95].

However, as more rigorous gapped bulk is developed, the inner edge become more and more capacitively coupled to the lower outer edge as the bulk becomes increasingly insulating. Since the capacitance is negligible due to the large arm width, the two edges are then completely decoupled when the bulk is fully gapped. The changing V_{Cc} and V_{eE} captured this dynamical process which results in a progressive decoupling of the inner and outer edge and the eventual settlement of the inner edge potential in the proximity of the ground. The lower arm then bears the whole Hall voltage.

In segment II, the 90° out-of-phase signal, $Y\rho_{cC}$, confirms a capacitor-like behaviour and peaks right where the bulk of the system starts transitioning into fully insulating (or gapped) states. Increasing B from 0.95 T to 1.0 T does not affect the 0-1 distribution except for a small variation likely related some excess charges accompanying the change in ν. The inner edge remains completely isolated (except capacitively via an extremely small capacitance) from the outer edge AC disturbance. As B goes beyond 1 T (into segment III), the incompressible gapped bulk starts to dissolve together with the chiral edges and $\rho_{Cc}(B)$ and $\rho_{eE}(B)$ again start to vary in opposite fashions until they become approximately even. With established decoupled inner and outer edges, we present the results on the QHE breakdown centered around the fully gapped region.

Considering the tremendous bulk resistance between the inner and the outer edges, electrometer level DC and DC+AC setups are adopted with a 100 μV rms AC voltage signal swept at f=3.78 Hz superposed to a variable DC bias from -15 mV to 15 mV raised by 100 μV steps. Fig. 5.12(k) shows a typical DC I-V result, obtained near the center of the plateau, showing a sharp threshold around $V_c \sim 10$ mV. More detailed results are obtained with the DC+AC technique measuring the differential resistance $r_d = dI/dV$ as a function

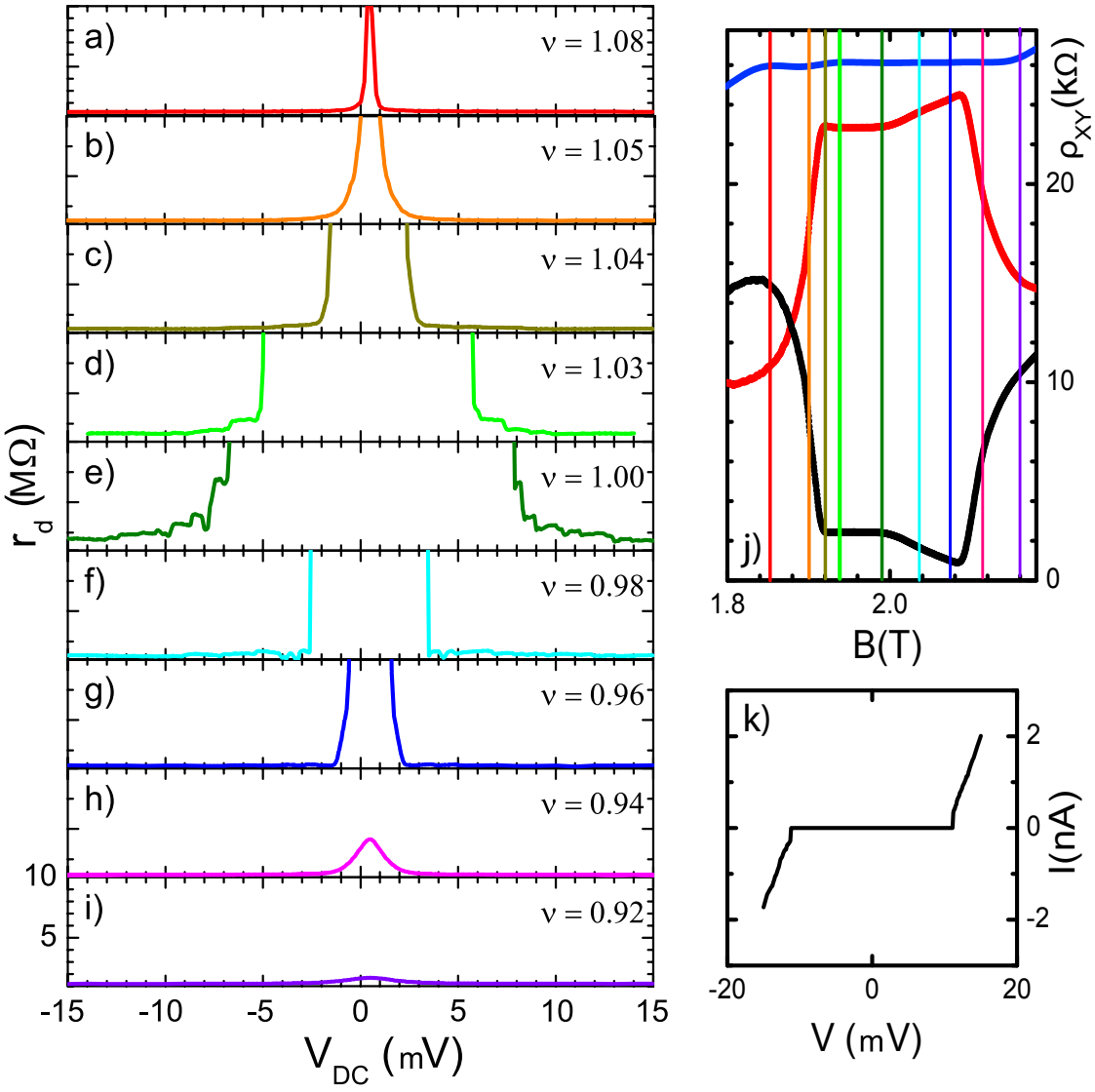

Figure 5.12: (a-i) Differential resistance as a function of the DC voltage bias between the inner and outer edge of the sample near ν=1. The whole range for which ρ_{EC} is quantized is covered, $1.08 > \nu > 0.92$. The plots show a threshold behaviour. r_d drastically increases from the MΩ range to value greater than 50 GΩ once the gap is opened. The colors of the plots on the left correspond to the lines in (j). (k) I-V curve from DC measurement at $\nu = 1$.

of V_{DC} for $1.08 > \nu > 0.92$.

Panels (a) through (i) in Fig. 5.12 record $r_d(V_{DC})$ for a series of B values from 1.85 T to 2.18 T with the locations marked by colored grid-lines shown in (j). A recognizable gap in V_{DC} starts around $\nu = 1.05$ where the critical voltage V_c reaches ∼0.5 mV. The r_d-V_{DC} is symmetric for positive and negative biases with no hysteresis. We consider $V_c(B)$ as the onset of QHE breakdown in terms both of the bulk current and dissipative edge current. However, the breakdown drastically depends on ν. For $\nu = 1.03$, the V_c is ∼5 mV followed by discontinuous steps. For $\nu = 1.00$, a remarkably sharp breakdown occurs at V_c ∼7.6 mV. For $\nu = 0.98$ and 0.96, the gap drops rapidly. Clearly, the most rigorous gap occurs at $\nu = 1.00$ for which the bulk is fully gaped with a measured resistance beyond 50 GΩ.

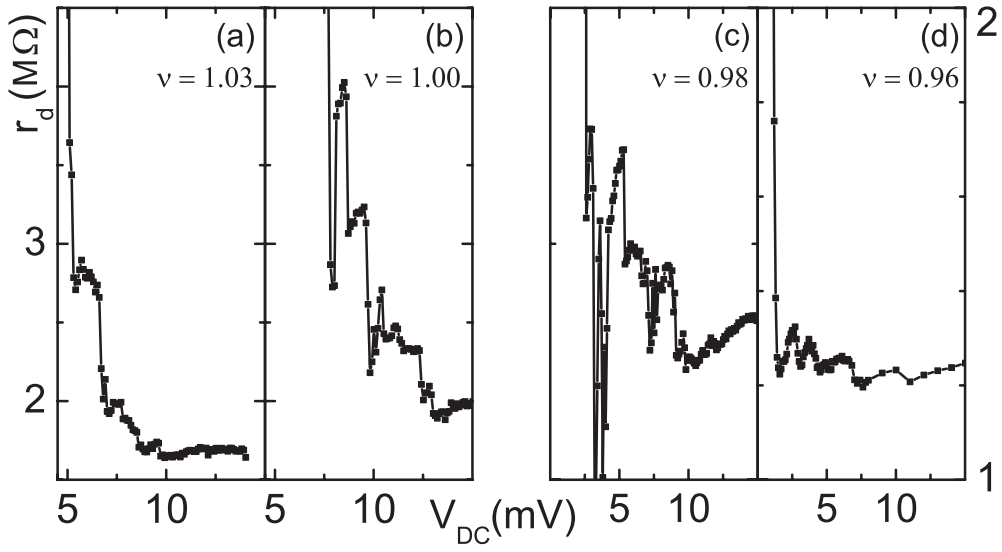

Figure 5.13: Step-like features respectively at (a) $\nu = 1.03$, (b) $\nu = 1.00$, (c) $\nu = 0.98$ and (d) $\nu = 0.96$.

The breakdown of the most stable states are shown in Fig. 5.13. It is evident that step-like features evolve from being very well defined $\nu = 1.03$ and $\nu = 1.00$ to disappear in ripples, $\nu = 0.96$. It is important to notice that even at high bias the dissipating state is

still very resistive, $r_d \sim$2 MΩ.

We will now focus on the well defined discontinuous steps for $\nu = 1.00$ shown in Fig. 5.15(a). A first sharp drop occurs at $V_{DC} = 7.6$ mV where r_d decreases drastically from > 50 GΩ down to 4 MΩ. r_d retains an approximately constant step while V_{DC} is increased from 7.6 mV to 8.2 mV where the second sudden drop occurs with r_d decreased to 3.2 MΩ. Constant r_d persists for another ∼0.6 mV increase in V_{DC} followed by another drop. Remarkably, the 0.6±0.1 mV steps in V_{DC} is exactly the LL spacing $\hbar\omega_c \sim 0.58$ meV. This results are indication that carrier excitations across the LLs via (resonant) voltage activation take place. The following is the proposed breakdown mechanism involving resonant-like tunnelings across the incompressible edge strips when the LLs of the edge channels are being lifted.

Before the detailed presentation of our proposed breakdown model it is useful to describe how in general, the Landau energy bands react to an applied voltage bias, Figure 5.14. In the general case of half-filled LL, $\nu = 2.5$, Fig. 5.14(a) the Fermi energy intersects the LL characterized by n=3 and the bulk is a compressible (metallic) electron liquid. n=2 and n=3 LLs are completely filled and two edge channels are formed at the edges. Note that these channels are not dissipationless, scattering is possible because they not strongly protected by topology (integer bulk filling is needed). At $\nu = 2.0$, Fig. 5.14(b), E_F is between LLs n=3 and n=2. In this situation a fully incompressible bulk state (no delocalized states available for conduction) is established and the two edge channels are chiral and dissipationless. When we apply a voltage bias, V_{DC} in Fig. 5.14(c), the E_F is shifted and at the equilibrium the LLs bend to minimize the electrostatic energy. Because of the bias an excess of charges flows in the system and populates the edges. The metallic, compressible in yellow, channels widen causing the incompressible strips to narrow. The separation between LLs stays constant at

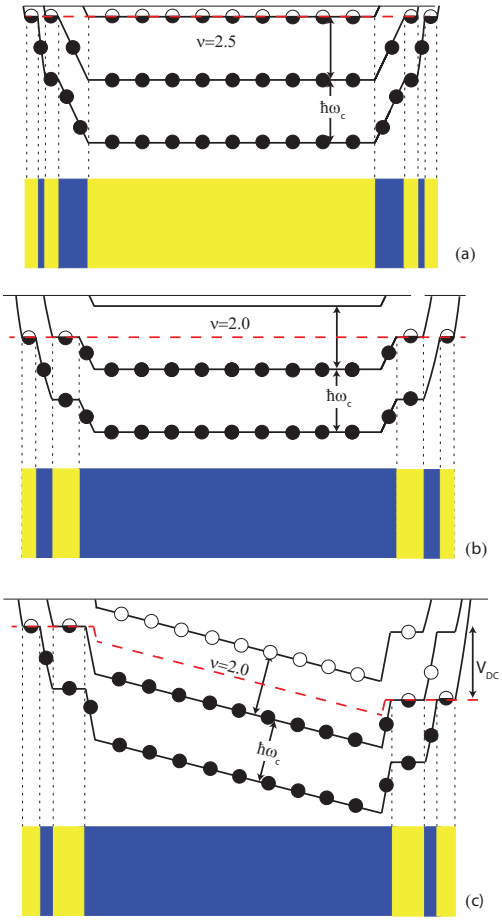

Figure 5.14: (a) LLs at $\nu = 2.5$, (b) at $\nu = 2.0$ and (c) $\nu = 2.0$ with an applied bias $V_{DC} > 0$. Yellow and blue regions correspond respectively to compressible and incompressible electron liquid.

$\hbar\omega_c$.

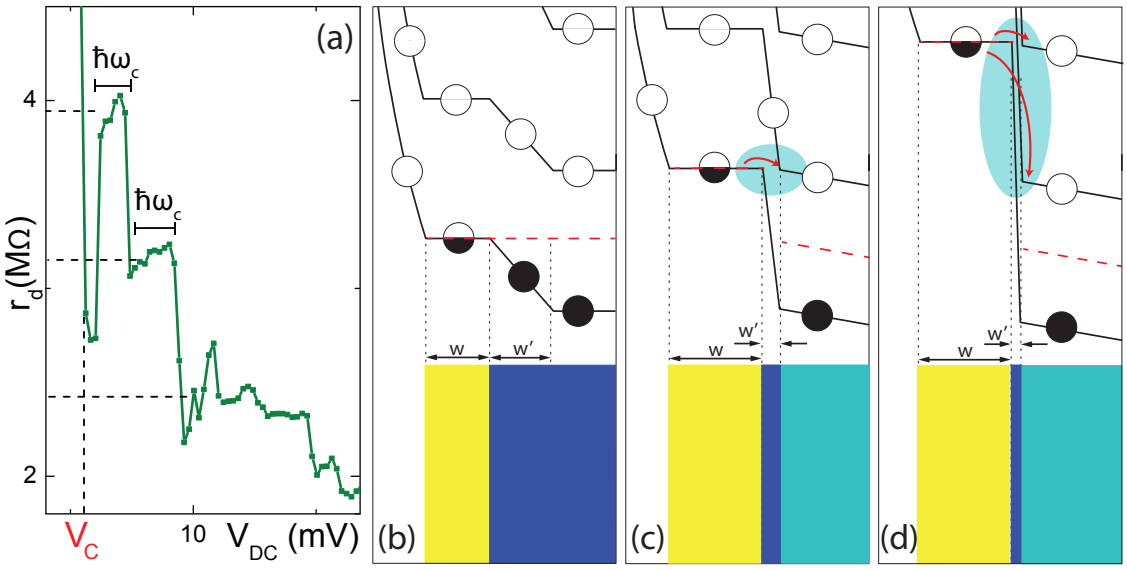

Figure 5.15: (a) Focus on the r_d steps recorded, at ν =1.00. Only one branch at positive bias is taken in consideration. The threshold is V_c ∼7.6 mV, and the width of the steps is comparable with $\hbar\omega_c$. On the right we show a schematic of the proposed breakdown process for (a) $V_{DC} = 0$, (b) $V_{DC} \sim V_c$ and (c) $V_{DC} \sim V_c + \hbar\omega_c$. The yellow region is for compressible edge state, blue for incompressible and cyan for excited bulk.

The details of the discontinuous steps for $\nu = 1.0$ are shown in Fig. 5.15(a). The first sharp drop at $V_{DC} = 7.6$ mV captures a drastic decrease in r_d from > 50 GΩ down to 4 MΩ. r_d retains an approximately constant step while V_{DC} is increased from 7.6 mV to 8.2 mV where the second drop occurs with r_d decreased to 3.2 MΩ. Constant r_d persists for another ∼0.6 mV increase in V_{DC} followed by another drop. Remarkably, the 0.6±0.1 mV steps in V_{DC} is exactly the LL spacing $\hbar\omega_c \sim 0.58$ meV.

The finite conductance in the bulk is due to the presence of mobile carriers. First, the possibility of LLs mixing caused by Umklapp scatterings mediated by phonons, when the carrier drift velocity v_D matches the sound speed v_s, is ruled out due to the following. At $\nu = 1$, $v_D = j/(pe)$ where p is the density and if we consider the current to flow through

the dissipationless edge channels of width w we have $j = I/w$ with $I = V_c/\rho_{xy}$. So, $v_D = V_c/(wpe\rho_{xy})$, with V_c=7.6 mV, yields $v_D \sim 4.4 \times 10^{-3}/w(m)$. Because of screening effects $w \gg l_B = \sqrt{\hbar/(eB)}$ and it has been estimated to range 50 nm and 200 nm [19, 96]. Thus, $22 < v_D < 88$ km/s is significantly larger than v_s ~5 km/s [97]

Thus, the mobile carriers in the bulk must come from the edge channels that are connected to the electrode reservoirs. The resistivity drops in sync with the energy rise at exactly $\hbar\omega_c$ steps indicates a resonant tunneling mechanism existing between the edge and bulk. The key is to explain why such a large $V_c \sim 7.6m$V$\sim 12\hbar\omega_c$ before the discontinuous steps take place.

The edge-bulk tunneling at $V_{DC} = 0$ is prohibited because, as shown in Fig. 5.15(b) for $\nu = 1.00$, the first LL is completely filled and the tunneling to the second LL in the bulk requires energy excitation of $1/2\ \hbar\omega_c \gg k_BT$ (since the edge channel energy $E_F = \pi\hbar p/m^*$ ~0.3 meV sits in the middle of the 1st and 2nd bulk LLs).

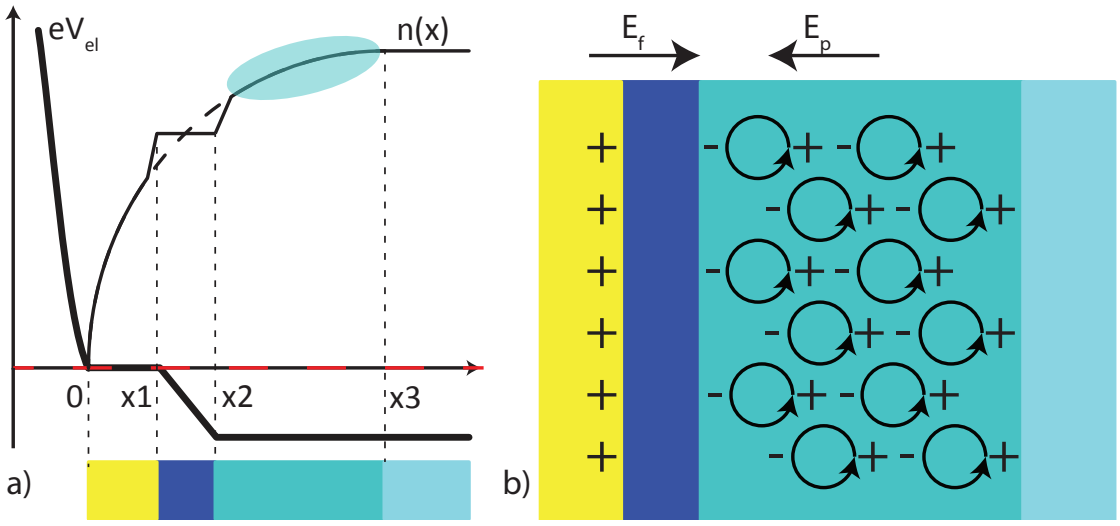

Figure 5.16: (a) Energy band and charge density as a function of the distance from the edge of the sample. Between x_2 and x_3 we have the polarized region. The dashed curve is the density without B-field. (b) Polarization model.

The energy band and the charge density as a function of distance x are illustrated in Fig. 5.16 where the edge reconstruction due to the screening effect results in bound charges, in both the incompressible strip and the crossover region, that can be polarized with a dipole moment ranging from zero to $q \cdot l_B = q\sqrt{\hbar/eB}$ depending the external field. l_B is the magnetic length. The effect of increasing V_{DC} (or electrical field), from the outer edge to the (grounded) inner edge, is countered by a rising polarization field up to a limit of $P = p \cdot el_B$ (P is the polarization). Setting $P = \chi\epsilon_0 E$ produces an upper limit of the polarization field of 10^5 V/m, which corresponds to ~ 10 mV, very close to V_c. As for the our results, this limit corresponds to $V_{DC} \sim 7.3$mV beyond which the E_F in the edge channel starts to rise and the bulk LL starts to tilt. The charge populations in the edge channel grows considerably. As a result, the width (w) of the chiral gapless channel increases and the width (w') of incompressible insulating strip inevitably narrows. With V_{DC} approaching V_c, E_F of the edge channel lines up with the 2nd LL in the bulk and the narrowed w' facilitates a resonant tunneling between the edge and the bulk so that a small amount of carriers above the mobility edge are now present in the bulk (cyan). This corresponds to the first drastic dip in the resistivity (with a slight over shooting shown in the data). Now, further increasing V_{DC} lifts edge E_F above the center of the 2nd LL in the bulk and the tunneling is moderately decreased as shown in the slight rise of r_d within a step. As V_{edge} is increased to $V_c + 1.5\hbar\omega_c$, the edge channel lines up with the 3rd LL and another resonant tunneling occurs [Fig. 5.15(d)]. As the whole system gets more conducting, increasing V_{DC} can no longer raise the band energy accordingly except by increasing the overall current flow. Then, the discontinuous features eventually diminish.

The robustness of the QHE, according to these results, originates from the polarization

of the bound cyclotron orbits limited by the magnetic length l_B. The edge reconstruction, which is inevitable when the charge density varies from the bulk value to zero (at the edge), dictates the bound charge distribution. The breakdown is achieved via resonant edge-bulk tunneling when energy bands are aligned. This mechanism helps explain other findings such as the STM [95] results showing major Hall voltage drop at the edges.

5.3 Quantum Hall effect in graphene

A four-terminal lock-in amplifier technique is utilized to characterize both CVD and natural graphene samples. The current excitation is 10 nA at a 13.7 Hz frequency. The gate voltage, V_g, is applied to the doped silicon separated from the graphene by 290 nm of SiO_2 using a low-noise battery to tune the Fermi level of the graphene. The influence of this gate potential on the charge carrier can be described by the parallel-plates capacitor model, so the induced carrier density as a function of the gate voltage can be estimated to be:

$$n(V_g) = V_g \frac{\epsilon_0 \epsilon_{ox}}{de} \approx 7.2 \times 10^{10} (cm^{-2}) V_g \tag{5.3}$$

The result of this measurement was at first very disappointing, because as you can see from

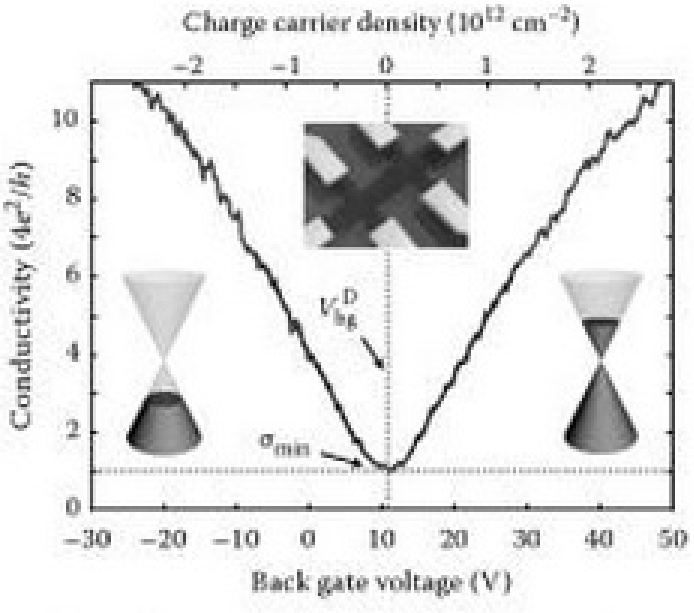

Figure 5.17: Conductivity as a function of the back gate voltage. The transport can be tuned from hole (left) to electron (right) regime by crossing the Dirac point. This sample was unintentionally p-doped, the minimum of the conductance is 10V shifted.[98]

Fig. 5.18, the change in the resistance with the gate voltage is very small and asymmetric

respect to the one expected, but after further thoughts we recognised that our curve is the almost exact copy of the end of the left branch of the reference one. In fact if we compare the values of the resistance and the values of the gate voltage we can see that our curve is shifted of 70 V. Now this shift could be due to an unintentional p-doping during the production of the CVD graphene and we will try to cover a larger range of gate voltage to see if we can entirely reproduce the curve at the top right of Fig.5.18.

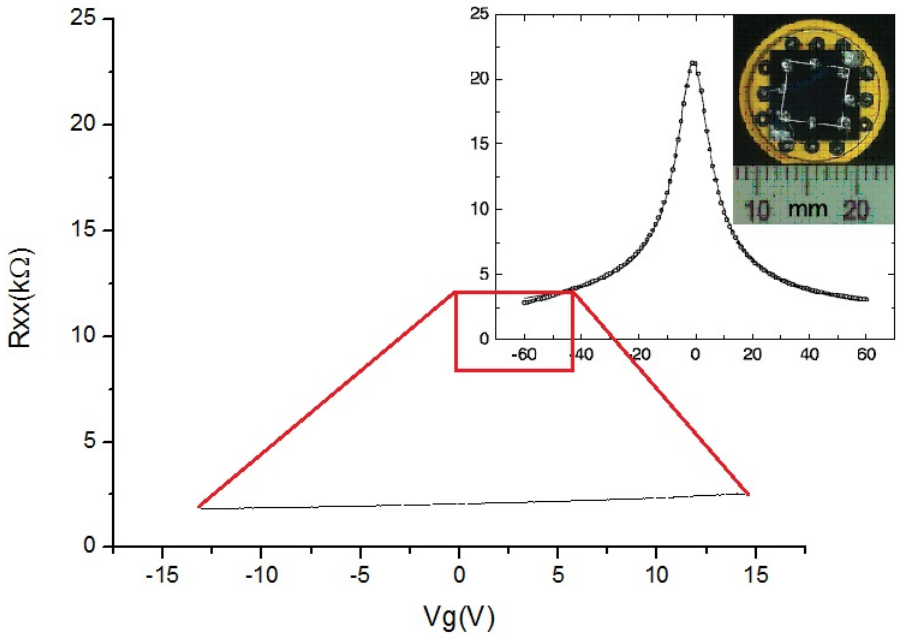

Figure 5.18: Source-Drain resistance vs gate potential, on the top right we have an experimental curve that shows the behaviour of the resistance for a gate voltage range of over 140 V[99]

We can estimate the mobility of the charge carriers using the field effect method, knowing the rate of change of the conductance, the back gate voltage, the capacitance and the linear dimensions of the sample:

$$\mu = \frac{L_{inner}}{W}\frac{1}{C_{bg}}\frac{\partial G_{xx}}{\partial V_g} \tag{5.4}$$

being W the distance between source and drain, L_{inner} the distance between the contact that

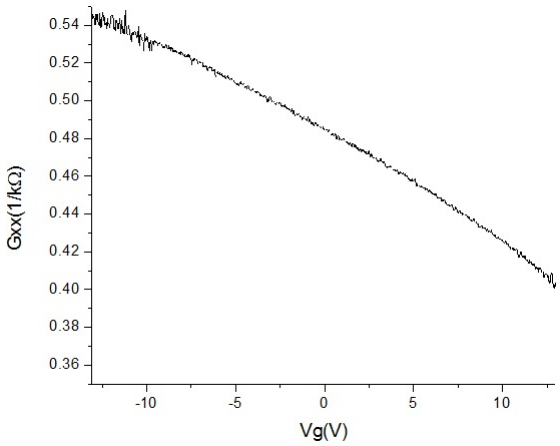

Figure 5.19: Plot of the conductance G_{xx} vs V_g.

we used to measure the drop of voltage, C_{bg} the capacitance per cm^2 and G_{xx} simply the conductance i.e. the inverse of the resistance.

The capacitance per cm^2 is a characteristic of the dielectric, SiO_2:

$$C_{bg} = \frac{\epsilon_0 \epsilon_r}{d} \tag{5.5}$$

where ϵ_r =3.9 and d=2.9$\times$ 10^{-5} cm, so we get C_{bg}=1.19$\times 10^{-8}$ F/cm^2. Averaging the values of $\partial G_{xx}/\partial V_g$ between -5 V and 5 V, Fig.5.19, we got that the mobility in that range is $\mu \approx 0.000053/(1.19 \times 10^{-8}) = 445 cm^2/(s \cdot V)$

We decided to test another sample of CVD graphene, but this time we increased the range for the gate voltage to be -85 V,+85 V and we increased the current trough the sample from 10 nA to 1 μA to reduce the noise. In this way could have the chance to see the passage between the hole to electron regime, and so it happened.Fig.5.20. We can see how this sample is p-doped and for this reason the position of the Delta-point results shifted of approximately 34 V, this point corresponds to the crossover between the two

regimes. Now from the derivative of the conductance we can find how the mobility of

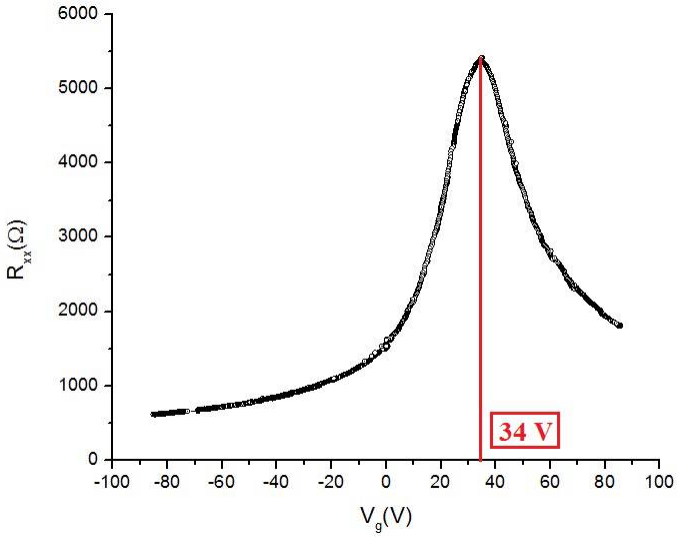

Figure 5.20: The resistance between source and drain as a function of the gate voltage, in red is the position of the Delta-point, 34 V.

holes and electrons varies with the gate voltage, Fig.5.21. We see that at the Delta-point the conductance has a maximum so the mobility is zero. Furthermore the mobility of the holes reaches the value of $\mu_h \approx 800\ cm^2/(s \cdot V)$ while the maximum for the electrons is $\mu_e \approx 400\ cm^2/(s \cdot V)$. Such values of mobility are expected for CVD graphene and are mostly due to the inhomogeneities introduced by the fabrication process. This is the reason for which, to investigate fundamental physics and for future applications, natural graphene is preferable.

We show that the mobility increases of a factor 10 for natural graphene on SiO_2, Figure 5.22. The relatively high-mobility of the sample, μ ~6000 $cm^2/(s \cdot V)$, allows us to investigate the QHE. Since low-density, high mobility, two-dimensional electronic systems exhibit quantum Hall effect, it is not a surprise that graphene exhibits the phenomenon too. The striking fact is that graphene presents a very unusual half-integer quantum Hall effect

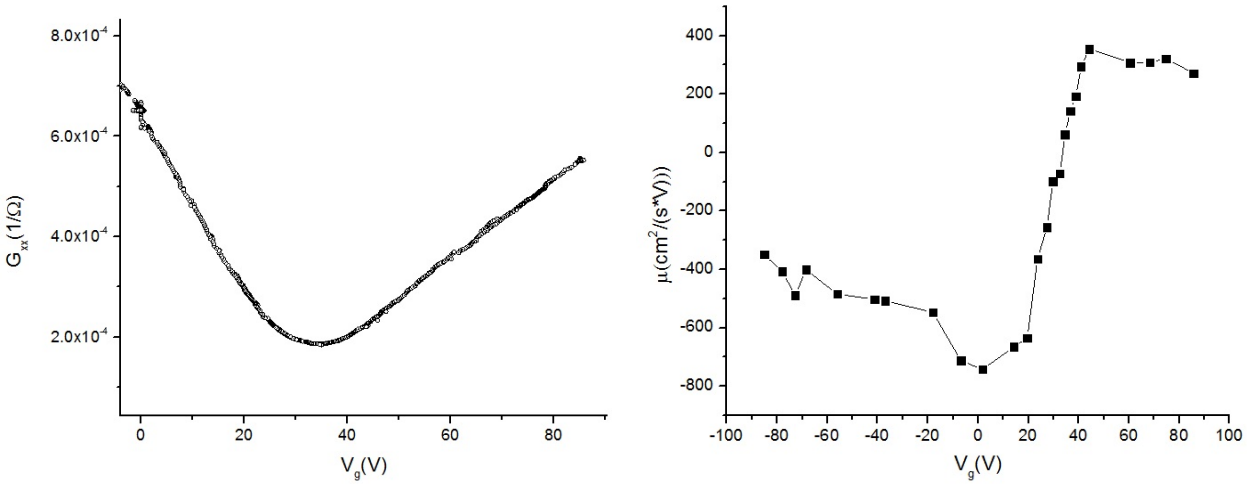

Figure 5.21: On the right we can see the conductance, G, I made the range symmetric around the Delta-point to show that the density of states for holes and electrons in asymmetric; on the left we can see the mobility going from negative (holes) to positive (electrons).

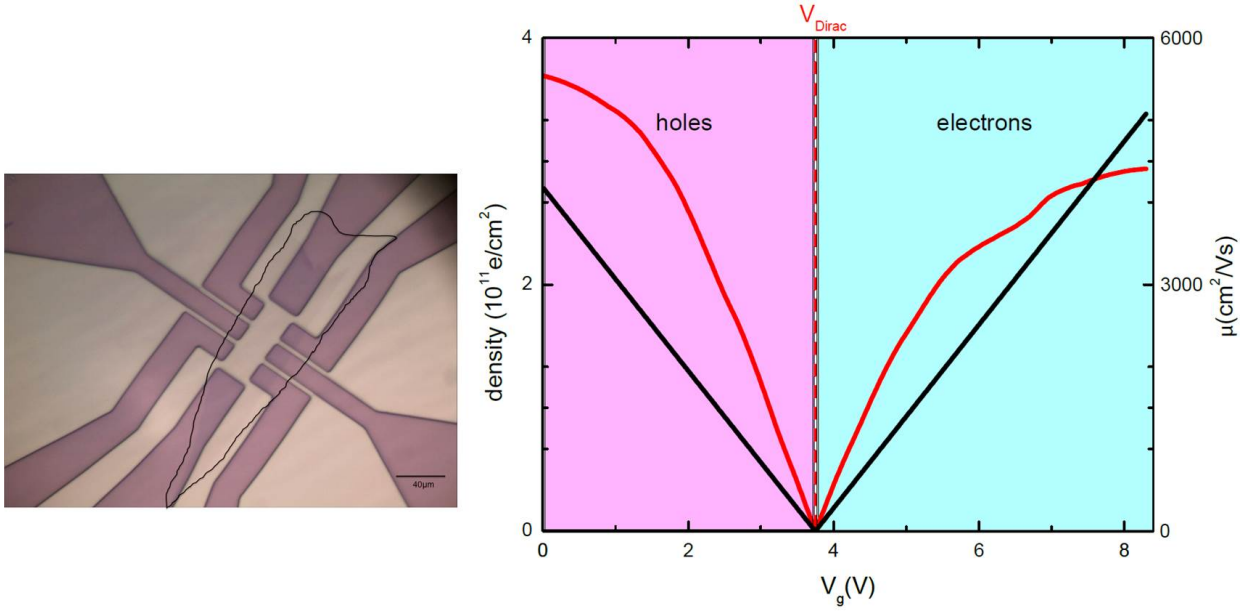

Figure 5.22: Left: optical image of the actual device, note the 40 μm scale bar, Right: measured density (black) and mobility (red) for the natural graphene sample.

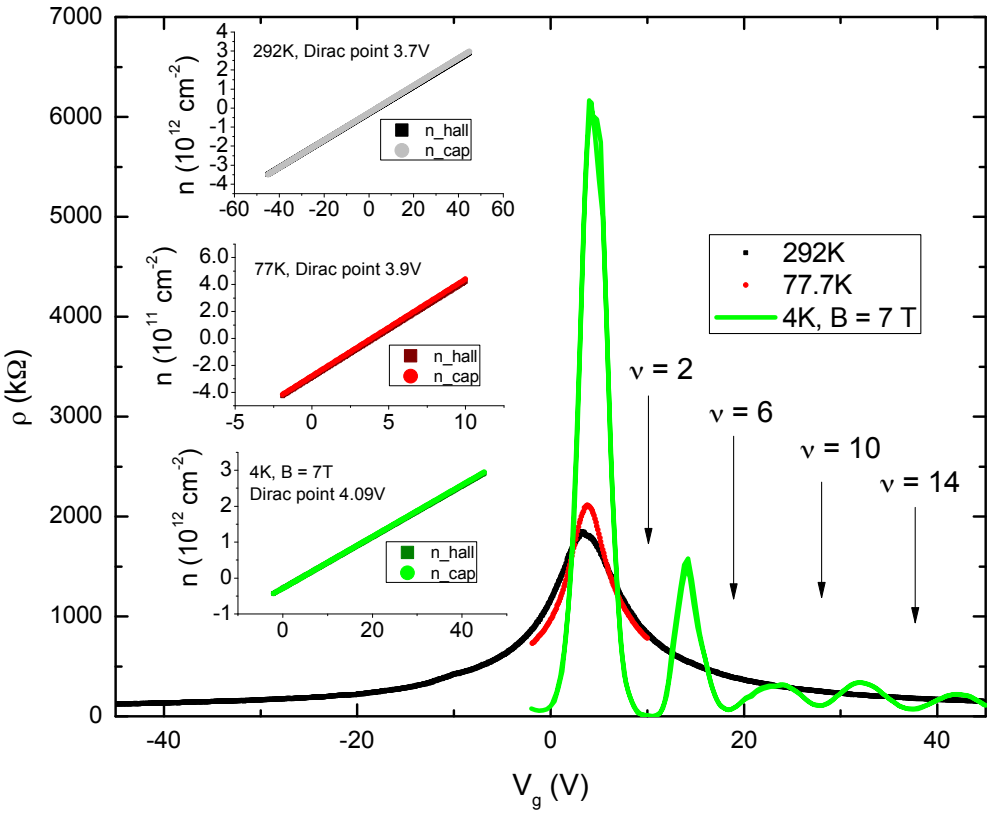

Figure 5.23: Magnetoresistance in quantum Hall effect regime. In the insets we show the density and Dirac point at 292 K, 77 K and 4 K.

(QHE) and a non-zero Berrys phase [100].

Up to this point we performed QHE measurement varying the B-field and recording the change in magnetoresistance and Hall resistance. In the case of graphene, the presence of a gate makes possible to keep the field constant and linearly vary the charge density. Doing so, we will shift the position of the Fermi energy instead of varying the spacing between LLs. We first notice that the mobility does not change dramatically from 300 K to 4 K. In Fig. 5.23, we observe the magnetoresistance going to zero, meaning that the Fermi energy is located between LLs. Our sample presents the anomaly characteristic of graphene systems first reported by Novoselov et al. in 2005 [100]. This anomaly consists in the fact that the

filling factor is quantized in terms of standard quantum Hall effect as:

$$\nu = 4\left(n + \frac{1}{2}\right) \tag{5.6}$$

In fact we distinctly observe ν =2, 6, 10 and 14, the closest to the $V_g = V_{Dirac}$ ∼4 V being ν=2. This anomaly, called half-integer quantum Hall effect, is unique. Various theories have predicted the anomaly [101–103] connecting the relativistic nature of the LLs and the electron-hole symmetry of graphene. As we already introduced, charge carriers in graphene have an approximately zero mass, that translates into a linear relativistic dispersion (Dirac fermions). Under this conditions, the LL spacing increases drastically and the quantization in magnetic field is described by:

$$E_N = v_F\sqrt{2e\hbar BN} \tag{5.7}$$

A schematic of the LLs is reported in Figure 5.24. With a Fermi velocity $v_F \sim 10^6$ m/s

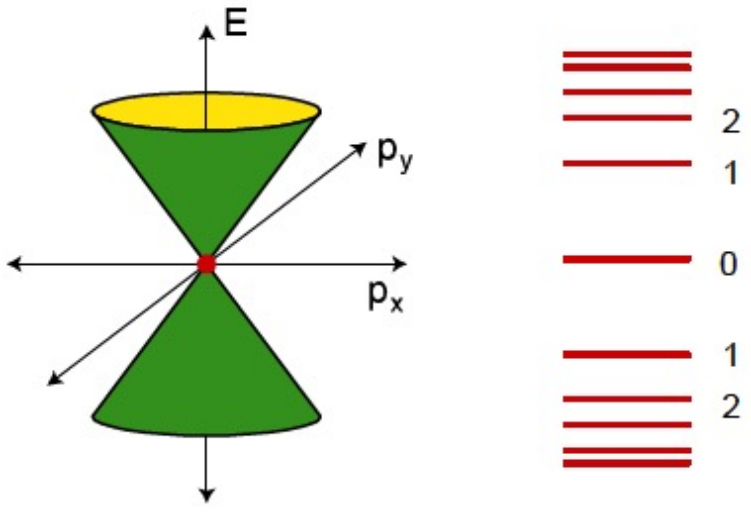

Figure 5.24: Band diagram and LLs in graphene [104].

we would get a LL spacing ΔE$\sim$2800 K at B=45 T. Note that at room temperature, the thermal energy $k_BT = 300$ K is a factor of 10 smaller. Also the mobility of the charge carriers does not change drastically between 300 K and 4 K. Quantum Hall effect has been observed in graphene at room temperature at 30 T [105] and it is expected that improving sample inhomogeneities will allows to achieve higher mobilities and to observe the room temperature quantum Hall effect at much lower B-fields.

The zero-energy LL (n=0) where electrons and holes are degenerate, is the symbol of the uniqueness of the graphene system. In Eq. 5.7 we assume that the separation between LL (E_N) is much larger than the Zeeman splitting. So each LL in 4-folds degenerate, due to both the spin and the sublattice degeneracy. This assumption is true for our experimental settings, where B=7 T, but the degeneracy is lifted for fields B>25 T.

5.3.1 Hybrid ultra-high gain and quantum efficiency graphene-quantum dots phototransistors

Let's first introduce the quantum dots. Quantum Dots (QDs) are semiconductor nanoparticles in which excitons are completely confined in all the three dimensions. Excitons are bound state of an electron and hole which are attracted to each other by the electrostatic Coulomb force. Because of their size 2-50 nm and their electrical characteristics they can be considered as artificial atoms. The basic principle of quantum dots is that once the exciton is created, the electron and hole will be trapped inside the insulating shield built around the core, and it will behave as a particle in a quantum well.Fig.5.25.

$$E_{conf} = \frac{\hbar^2\pi^2}{2a}\left(\frac{1}{m_e} + \frac{1}{m_h}\right) \tag{5.8}$$

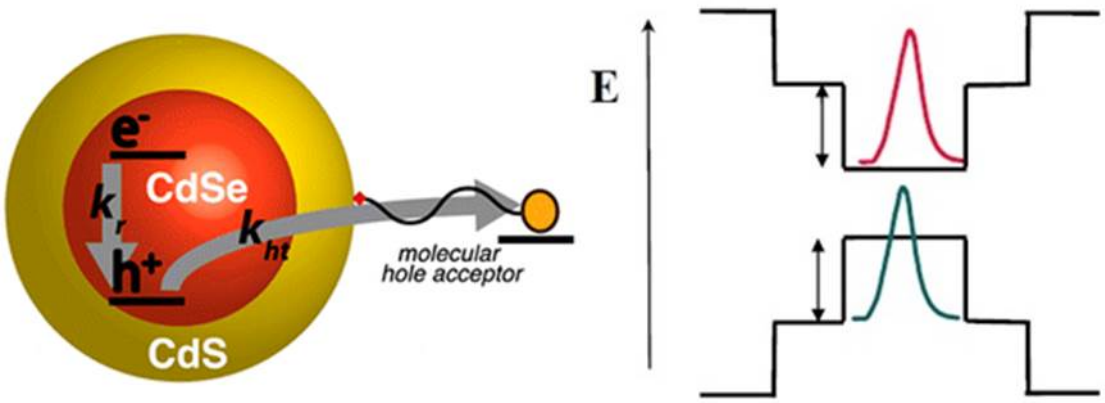

Figure 5.25: We can see a schematic reproduction of a CdSe quantum dot with the insulating shell surrounding the semiconductor core and on the left an electron (red) and an hole (blue) in a schematic representation of the square well in a quantum dot [106].

Because of this situation the Quantum Dot energy gap is strongly specified by its size. The *confinement energy* dominates when the size of the quantum dot becomes smaller than the excitons Bohr radius $a_{ex} = (m/\mu)\epsilon_r a_B$ and electronic and optical properties are strongly determined by the size of the well. So band gap is related to the process in which an electron is excited by the light and stabilized. Band gap width is related inversely to the QD diameter: compared to large QDs, smaller QDs have wider band gaps, absorb shorter wavelengths, and fluoresce at shorter wavelengths. Fig.5.26.

Depending on the QD core/shell structure they can be classified in QD type-I and QD type-II. In type-I QDs, the energy band gap of the shell material is larger than that of the core material so the electron-hole pair is confined within the core, so type-I QDs are used to get higher photoluminescence (PL) efficiency. In type-II QDs, the energy levels of the valence band and the conduction band of core and shell cross each other so some of the electrons are separated from their holes. Because of this characteristic, type-II QDs can be

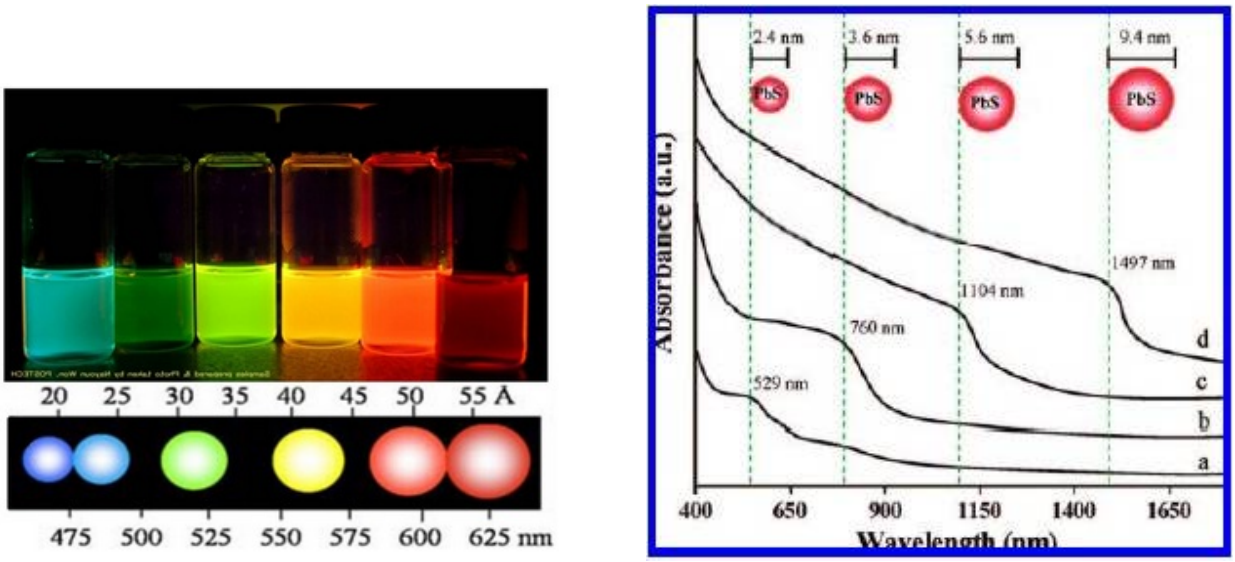

Figure 5.26: Absorbed and emitted wavelengths for different sizes of QD [107].

used as an energy-conversion material in solar cells. Changes in the energy levels of the valence band and the conduction band of core and shell affect the charge density of electrons and holes in space. The change in energy levels also causes an effective band gap which has quite irrelevant with composing materials, so the wavelength of absorption and the PL are controllable. In our device we will use type-II QDs.Fig.5.27

The most common QDs are II-IV type such as CdS, CdSe, PbSe, PbS and PbTe. But because Cadmium can be toxic and electron and hole radii are longer in Pb compounds making easier to access to strong confinement regime, PbS, PbSe, PbTe are preferred. This kind of materials are usually produced by colloidal synthesis.

The very peculiar energy band structure of the type-II QDs makes possible to separate the excitons: the electron remains trapped while the hole is free to leave the dot and contribute to the current, this makes it possible to improve photocatalytic activity. Also in QDs has been demonstrated the Multiple Excitons Generation (MGE) [109]. This will lead to break the Schokley-Queisser limit [110]. The MGE involves the generation of multiple electron-

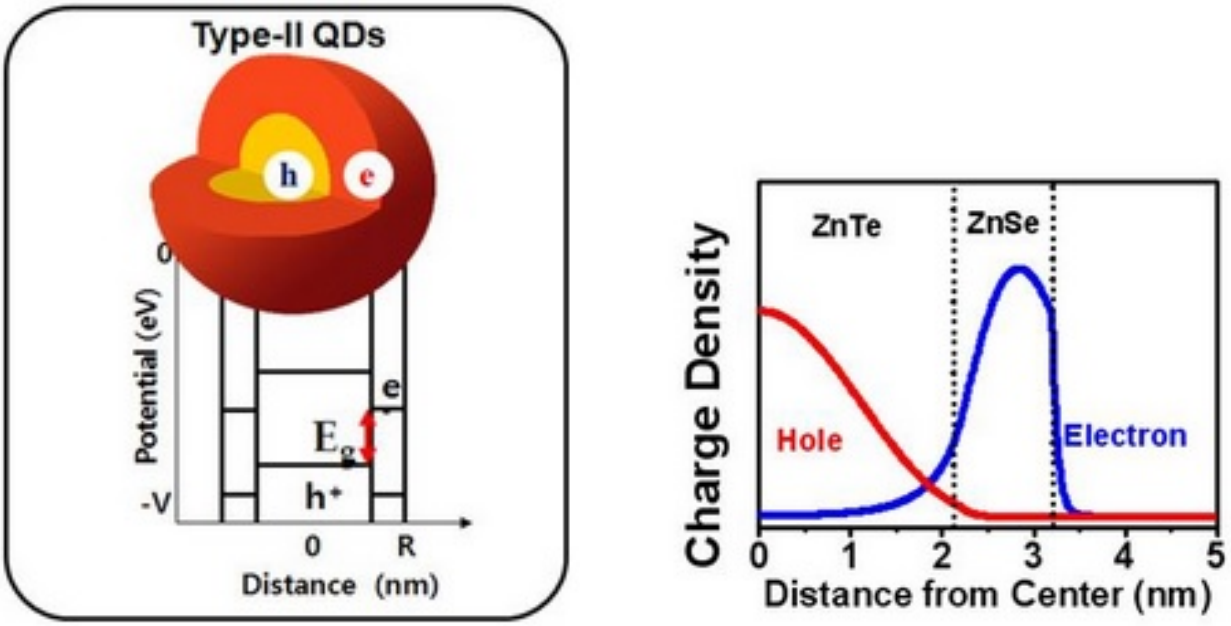

Figure 5.27: Spatial distribution of the electronic bands in type-II and carrier densities [108].

hole pairs from the absorption of a single photon, the origin of this phenomenon is still very debated. Furthermore, the long Exciton range prevents the electron-hole recombination.

Quantum Dots can be used to improve the performances of graphene-based optical devises because graphene has an incredibly fast response due to its very high carrier mobility but it is almost transparent to light and lacks of a gain mechanism that can generate multiple charge carriers from one incident photon. So a graphene-based photodetector cannot be efficient enough, this problem can be solved by covering the graphene with a thin film of colloidal Quantum Dots. They are good light absorbers and we can easily tune their absorption spectrum. Also the photogenerated charges in the QDs can transfer to graphene, while oppositely charged carriers remain trapped in the quantum-dot layer, Fig. 5.28. There is a further advantage of using a layer of QDs on graphene: trapped carriers lead to a photogating effect, where the presence of these charges changes the graphene sheet resistance through capacitive coupling.

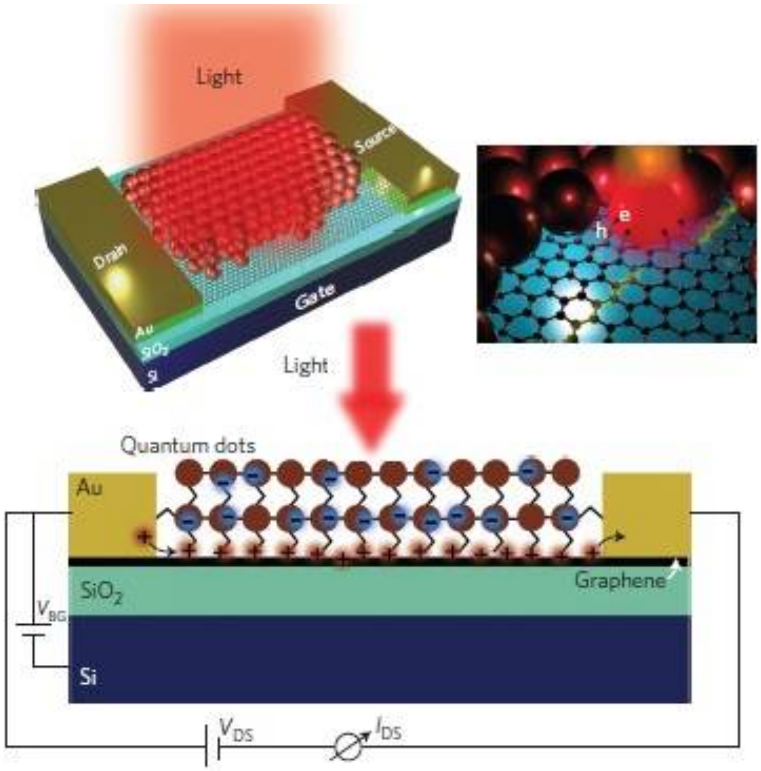

Figure 5.28: Representation of an hybrid graphene quantum dots photodetector [111].

So coating the graphene with a thin film of QDs we can reach a theoretically calculated gain of 10^8 electrons per photon absorbed[111]. This huge gain can be interpreted as the ratio between the time that the electron remains trapped in the QD (τ_{life}) and the time that takes to the holes to reach the contact ($\tau_{transit}$). In our case, we are using graphene that has an extreme high mobility and QDs with a very high trapping power, so the charge carriers recirculate in the graphene during the lifetime of a single trapped charge. Once it is established that it is possible to obtain such a high gain we must consider the problem of production, for example related to the small extension of graphene sheets. A possible design for our photodetector could be the one that implies a *suspended* graphene layer, Fig.5.29, that will allow us to eliminate the interface states that inevitably form when the graphene is in contact with the substrate and will enhance the capacitive coupling between the gate

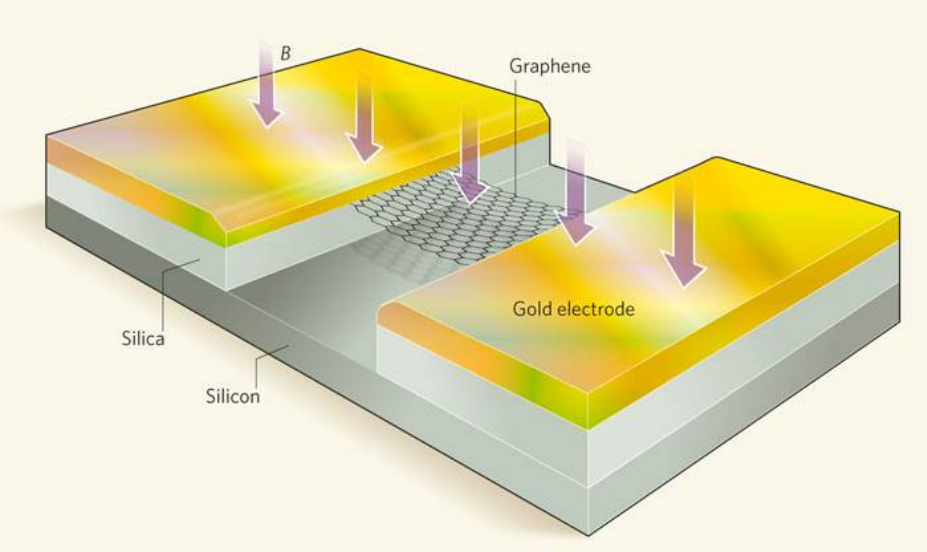

Figure 5.29: Photodetector with suspended graphene sheet between the contacts [112].

and the graphene.

CHAPTER 6 SUMMARY

In our research we have succeeded to fabricate both GaAs-based and graphene-based high purity devices. The superior quality of the sample is crucial for exploring fragile quantum states. During the yeas we have tuned the fabrication techniques to obtain the needed quality in the most efficient way. UV photolithography is fundamental for our object: this technique allows us to minimize the unintentional doping and contamination insuring the high purity of the samples. Extremely low-noise electronic transport measurements have been performed down to millikelvin range. Only if these conditions are respected, quantum Hall measurements are successful and novel phases of matter can be explored.

In summary, the Shubnikov de Haas oscillations of two dilute 2DHS confined in 20 nm wide (100)-GaAs quantum wells have been observed. Through the analysis of the SdH Fourier spectrum has been found that the topmost valence band (HH) of a 2DHS with p =4.3-4.8$\times 10^{10}$cm^{-2} is still degenerate (to our measurement resolution). This finding leads to the conclusion that in such conditions, the SOI are not strong enough to induce an observable band splitting. Furthermore, m^* has been measured for both systems by studying the T-dependence of the SdH oscillations. It has been found to slightly increase with increasing B and p and its value ranges between 0.30-0.50m_e for 0.08$\leq B \leq$0.250 T. These results are essential for the investigation of strongly interacting systems where inter-particle Coulomb energy becomes increasingly important.

Then, we adopted an anti-Hall bar geometry whose remarkable characteristic is to present an extra set of edges. This modification preserves the topological invariant precisely as to a regular Hall bar for the same filling factor (ν). The onset of the breakdown probed by voltage biasing the inner edge relative to the outer edges reveals an extremely sharp threshold beyond

which a series of discontinuous steps, spaced at exactly the LL spacing $\hbar\omega_c$, manifest. It suggests a resonant-like tunneling mechanism across the dynamically varying incompressible edge strips when the alignment of the edge LLs to the bulk LLs takes place. In addition, the formation of the chiral edge channels proceeds the fully gapped bulk which occurs only within a small window. The rising and falling of the gapped bulk states leads to a novel 0-1 Hall voltage distribution: approximately zero voltage drops across one arm and the whole Hall voltage ($h/(\nu e^2 I)$) drops across the other arm.

Our work on graphene-based devices has provided us with important insights on both fabrication techniques and theory. We have confirmed that natural graphene presents better transport properties as mobility (10-fold higher) and delta point closer to zero. Also we have been able to observe the anomalous quantum Hall effect, unique to graphene, symbol of the high quality of the device. We explored the opportunity for applications as ultra-high gain and quantum efficiency hybrid graphene-quantum dots phototransistors.

BIBLIOGRAPHY

[1] A. Isihara, Solid State Physics **42**, 271 (1989).

[2] B. Spivak, S. V. Kravchenko, S. A. Kivelson, and X. P. A. Gao, Rev. Mod. Phys. **82**, 1743 (2010).

[3] J. Huang, L. N. Pfeiffer, and K. W. West, Phys. Rev. B **85**, 041304(R) (2012).

[4] S. A. Wolf et al., Science **294**, 1488 (2001).

[5] H. Zhu et al., Solid State Communications **141**, 510 (2007).

[6] K. v. Klitzing, G. Dorda, and M. Pepper, Phys. Rev. Lett. **45** (1980).

[7] D. C. Tsui, H. L. Stormer, and A. C. Gossard, Phys. Rev. Lett. **48**, 1559 (1982).

[8] T. M. Lu et al., Appl. Phys. Lett. **92** (2008).

[9] D. J. Thouless, M. Kohmoto, M. P. Nightingale, and M. den Nijs, Phys. Rev. Lett. **49**, 405 (1982).

[10] M. E. Cage et al., Phys. Rev. Lett. **51**, 1374 (1983).

[11] O. Heinonen, P. L. Taylor, and S. M. Girvin, Phys. Rev. B **30**, 3016 (1984).

[12] L. Eaves and F. W. Sheard, Semiconductor Science and Technology **1**, 346 (1986).

[13] S. Komiyama, Y. Kawaguchi, T. Osada, and Y. Shiraki, Phys. Rev. Lett. **77**, 558 (1996).

[14] S. Komiyama and Y. Kawaguchi, Phys. Rev. B **61**, 2014 (2000).

[15] S. A. Trugman, Phys. Rev. B **27**, 7539 (1983).

[16] P. Streda and K. von Klitzing, Journal of Physics C: Solid State Physics **17**, L483 (1984).

[17] V. Tsemekhman, K. Tsemekhman, C. Wexler, J. H. Han, and D. J. Thouless, Phys. Rev. B **55**, R10201 (1997).

[18] A. M. Martin, K. A. Benedict, F. W. Sheard, and L. Eaves, Phys. Rev. Lett. **91**, 126803 (2003).

[19] D. B. Chklovskii, B. I. Shklovskii, and L. I. Glazman, Phys. Rev. B **46**, 4026 (1992).

[20] S. W. Hwang, D. C. Tsui, and M. Shayegan, Phys. Rev. B **48**, 8161 (1993).

[21] B. Alphenaar, P. McEuen, R. Wheeler, and R. Sacks, Physical review letters **64**, 677 (1990).

[22] M. Grayson, D. Tsui, L. Pfeiffer, K. West, and A. Chang, Physical review letters **80**, 1062 (1998).

[23] M. A. Topinka et al., Science **289**, 2323 (2000).

[24] R. Haug, A. MacDonald, P. Streda, and K. Von Klitzing, Physical review letters **61**, 2797 (1988).

[25] F. Amet, J. Williams, K. Watanabe, T. Taniguchi, and D. Goldhaber-Gordon, Physical review letters **112**, 196601 (2014).

[26] R. B. Laughlin, Phys. Rev. B **23**, 5632 (1981).

[27] B. I. Halperin, Phys. Rev. B **25**, 2185 (1982).

[28] D. A. Syphers, K. P. Martin, and R. J. Higgins, Applied Physics Letters **48**, 293 (1986).

[29] P. F. Fontein, J. M. Lagemaat, J. Wolter, and J. P. Andre, Semiconductor Science and Technology **3**, 915 (1988).

[30] N. W. Ashcroft and N. D. Mermin, *Solid state physics*, Holt, Rinehart and Winston, 1976.

[31] L. Landau, Soviet Physics Jetp-Ussr **8**, 70 (1959).

[32] V. Dobrosavljevic, N. Trivedi, and J. M. Valles Jr, *Conductor insulator quantum phase transitions*, volume 16, Oxford University Press, 2012.

[33] N. F. Mott, Proceedings of the Physical Society. Section A **62**, 416 (1949).

[34] J. Hubbard, Electron correlations in narrow energy bands, in *Proceedings of the Royal Society of London A: Mathematical, Physical and Engineering Sciences*, volume 276, pages 238–257, The Royal Society, 1963.

[35] P. W. Anderson, Physical Review **115**, 2 (1959).

[36] G. Thomas, M. Capizzi, F. DeRosa, R. Bhatt, and T. Rice, Physical Review B **23**, 5472 (1981).

[37] E. Wigner, Physical Review **46**, 1002 (1934).

[38] Wigner crystal, http://www.tcm.phy.cam.ac.uk/~mdt26/qmc_projects2/wigner_crystals.html.

[39] D. M. Ceperley and B. J. Alder, Phys. Rev. Lett. **45**, 566 (1980).

[40] G. Ortiz, M. Harris, and P. Ballone, Physical review letters **82**, 5317 (1999).

[41] E. P. Wigner and F. Seitz, On the constitution of metallic sodium, in *Part I: Physical Chemistry. Part II: Solid State Physics*, pages 365–371, Springer, 1997.

[42] P. W. Anderson, Physical review **109**, 1492 (1958).

[43] G. Bergmann, Physics Reports **107**, 1 (1984).

[44] A. G. Aronov and Y. V. Sharvin, Rev. Mod. Phys. **59**, 755 (1987).

[45] P. A. Lee and T. Ramakrishnan, Reviews of Modern Physics **57**, 287 (1985).

[46] M. E. Cage et al., *The quantum Hall effect*, Springer Science & Business Media, 2012.

[47] T. Englert and K. Von Klitzing, Surface Science **73**, 70 (1978).

[48] F. Schopfer and W. Poirier, Journal of Applied Physics **102**, 054903 (2007).

[49] H. Wei, D. Tsui, M. Paalanen, and A. Pruisken, Physical review letters **61**, 1294 (1988).

[50] R. Willett et al., Physical review letters **59**, 1776 (1987).

[51] J. R. Hook and H. E. Hall, Solid state physics (the manchester physics series), 2000.

[52] B. Jeckelmann and B. Jeanneret, Measurement Science and Technology **14**, 1229 (2003).

[53] W. van der Wel et al., Journal of applied physics **65**, 3487 (1989).

[54] M. Buttiker, Phys. Rev. B **38**, 9375 (1988).

[55] R. Landauer, IBM Journal of Research and Development **1**, 223 (1957).

[56] S. Washburn, A. Fowler, H. Schmid, and D. Kern, Physical review letters **61**, 2801 (1988).

[57] B. Van Wees et al., Physical Review Letters **62**, 2523 (1989).

[58] R. Landauer, Philosophical Magazine **21**, 863 (1970).

[59] B. Van Wees et al., Physical Review B **39**, 8066 (1989).

[60] C. Beenakker, Physical review letters **64**, 216 (1990).

[61] D. J. Thouless, M. Kohmoto, M. P. Nightingale, and M. den Nij, Phys. Rev. Lett. **49**, 405 (1982).

[62] M. Z. Hasan and C. L. Kane, Rev. Mod. Phys. **82**, 3045 (2010).

[63] J. E. Moore, Nature **464**, 194 (2010).

[64] X.-L. Qi and S.-C. Zhang, Rev. Mod. Phys. **83**, 1057 (2011).

[65] Representation of the topological theory, `http://jiharu.github.io/datt2500/lecture02.html`.

[66] K. Von Klitzing, 25 years of quantum hall effect (qhe) a personal view on the discovery, physics and applications of this quantum effect, in *The Quantum Hall Effect*, pages 1–21, Springer, 2005.

[67] B. A. Bernevig, T. L. Hughes, and S.-C. Zhang, Science **314**, 1757 (2006).

[68] F. D. M. Haldane, Phys. Rev. Lett. **61**, 2015 (1988).

[69] C. Wu, B. A. Bernevig, and S.-C. Zhang, Phys. Rev. Lett. **96**, 106401 (2006).

[70] X. L. Qi and S. C. Zhang, Phys. Today **63** (2010).

[71] T. Knighton et al., Applied Physics Letters **104**, 193109 (2014).

[72] T. Knighton et al., Physical Review B **90**, 165117 (2014).

[73] A. K. Geim and K. S. Novoselov, Nature materials **6**, 183 (2007).

[74] Representation of graphene, `http://craigbanksresearch.com/page3.php`.

[75] M. Wilson, Physics Today **59**, 21 (2006).

[76] B. Partoens and F. Peeters, Physical Review B **74**, 075404 (2006).

[77] J. W. Anthony, R. A. Bideaux, K. W. Bladh, and M. C. Nichols, Handbook of mineralogy, mineralogical society of america, chantilly, va 20151-1110, usa, 2011.

[78] Afm schematics, `http://comp.uark.edu/~jchakhal/AFM20scans.htm`.

[79] Raman spectrometer schematic, `https://www.semrock.com/filter-types-for-raman-spectroscopy-applications.aspx`.

[80] Raman spectra multi, by and monolayer, http://www.eng.nanophoton.jp/applications/img/22_img03.jpg.

[81] Dilution refrigerator schematics, http://image.slidesharecdn.com/smbmay82014-140528100902-phpapp01/95/smb-cafe-8-may-2014-leiden-cryogenics-9-638.jpg?cb=1401272049.

[82] V. Tarquini et al., Applied Physics Letters **104**, 092102 (2014).

[83] T. Lu et al., Applied Physics Letters **92**, 12109 (2008).

[84] R. Winkler, *Spin–Orbit Coupling Effects in Two-Dimensional Electron and Hole Systems*, 2003.

[85] U. Ekenberg and M. Altarelli, Phys. Rev. B **32**, 3712 (1985).

[86] H. L. Stormer et al., Phys. Rev. Lett. **51**, 126 (1983).

[87] B. Habib, M. Shayegan, and R. Winkler, Semiconductor Science and Technology **24**, 064002 (2009).

[88] Y. Yaish et al., Phys. Rev. Lett. **84**, 4954 (2000).

[89] J. P. Lu et al., Phys. Rev. Lett. **81**, 1282 (1998).

[90] Y. Chiu et al., Phys. Rev. B **84**, 155459 (2011).

[91] Z. Yuan, R. Du, M. Manfra, L. Pfeiffer, and K. West, Applied Physics Letters **94**, 052103 (2009).

[92] T. Ando and Y. Uemura, Journal of the Physical Society of Japan **36**, 959 (1974).

[93] R. B. Dingle, Proceedings of the Royal Society of London A: Mathematical, Physical and Engineering Sciences **211**, 517 (1952).

[94] J. P. Eisenstein, H. L. Störmer, V. Narayanamurti, A. C. Gossard, and W. Wiegmann, Phys. Rev. Lett. **53**, 2579 (1984).

[95] E. Ahlswede, P. Weitz, J. Weis, K. von Klitzing, and K. Eberl, Physica B: Condensed Matter **298**, 562 (2001).

[96] K. Lier and R. R. Gerhardts, Phys. Rev. B **50**, 7757 (1994).

[97] J. S. Blakemore, Journal of Applied Physics **53**, R123 (1982).

[98] K. D. Sattler, *Handbook of nanophysics: functional nanomaterials*, CRC Press, 2010.

[99] T. Shen et al., Applied Physics Letters **99**, 232110 (2011).

[100] K. S. Novoselov et al., Nature **438**, 197 (2005).

[101] Y. Zheng and T. Ando, Physical Review B **65**, 245420 (2002).

[102] V. Gusynin and S. Sharapov, Physical Review Letters **95**, 146801 (2005).

[103] N. Peres, F. Guinea, and A. C. Neto, Physical Review B **73**, 125411 (2006).

[104] Quantum theory of graphene, `http://www.physics.upenn.edu/~kane/pedagogical/295lec3.pdf`.

[105] K. S. Novoselov et al., Science **315**, 1379 (2007).

[106] Cdse band structure, `http://www.cchem.berkeley.edu/pagrp/abstractimages/abstract318.gif`.

[107] Absorbed and emitted wavelengths for different sizes of qd, http://www.nanotrio.com/board/list.php?board_num=11.

[108] J. Bang et al., Chemistry of Materials **22**, 233 (2010).

[109] R. Service, Science (New York, NY) **322**, 1784 (2008).

[110] W. Shockley and H. J. Queisser, Journal of applied physics **32**, 510 (1961).

[111] G. Konstantatos et al., Nature nanotechnology **7**, 363 (2012).

[112] A. F. Morpurgo, Nature **462**, 170 (2009).

ABSTRACT

ELECTRONIC TRANSPORT IN TWO-DIMENSIONAL SYSTEMS IN THE QUANTUM HALL REGIME

by

VINICIO TARQUINI

August 2016

Advisor: Dr. Jian Huang

Major: Physics

Degree: Doctor of Philosophy

The integer and the fractional quantum Hall effects are essential to the exploration of quantum matters characterized by topological phases. A quantum Hall system hosts one-dimensional (1D) chiral edge channels that manifest zero magnetoresistance, dissipationless due to the broken time reversal symmetry, and quantized Hall resistance νhe^2 with ν being the topological invariant (or Chern number). The 1-1 correspondence between the conducting gapless edge channels to the gapped incompressible bulk states is a defining character of a topological insulator (TI). Understanding this correspondence in real systems, especially the origin of its robustness (in terms of the limit of breakdown), is important both fundamentally and practically (i.e. in relation to spintronics). However, the breakdown mechanism, especially in light of the edge-bulk correlation, is still an open question. We adopt GaAs two-dimensional (2D) high-mobility hole systems confined in a 20 nm wide (100)-GaAs quantum wells and have perform transport measurement for a range of charge densities between 4 and 5 x 10^{10} cm^{-2} with a carrier mobility of 2 4 x 10^6 $cm^2/V{\cdot}s$ down to millikelvin temperatures. Systematic characterization of the 2D systems through Shubnikov-de Haas (SdH) oscillations yields an effective mass between 0.30 and 0.50 m_e, in good agreement with the cyclotron

resonance results. We then modify a regular Hall bar system into a unique anti-Hall bar geometry that provides an extra set of independent chiral edge channels without altering the topological invariant. We perform systematic measurement of quantum oscillations via chiral edges while simultaneously probing the bulk dynamics, through measuring across independent edges, in respond to the edge excitations. The edge-bulk correspondence reveals a non-equilibrium dynamical development of the incompressible bulk states that leads to a novel asymmetrical 1-0 Hall potential distribution. Moreover, probing the breakdown via inner and outer edges reveals a breakdown in discontinuous steps characterized by exactly the Landau level spacing. These results are the first-time evidence for a resonant quantum tunneling mechanism realized through aligning the edge and bulk energy levels.

We also explored the fundamental physics of graphene-based devices with an eye focused on possible applications as ultra-high gain and quantum efficiency hybrid graphene-quantum dots phototransistors. We have confirmed that natural graphene presents better transport properties as mobility (10-fold higher) and delta point closer to zero. Also we have been able to observe the anomalous quantum Hall effect, unique to graphene, symbol of the high quality of the device. More experimental work is needed to gain more insights on the real efficiency of the devices and a more efficient fabrication.

AUTOBIOGRAPHICAL STATEMENT

Name: Vinicio Tarquini

Education:
B.S. Physics, Universita' dell'Aquila, L'Aquila, Italy, 2009
M.S. Physics, Universita' dell'Aquila, L'Aquila, Italy, 2011
M.S. Physics, Wayne State University, Detroit, Michigan, 2014
Professional Experience:
Graduate Teaching and Research Assistant, Dept. of Physics and Astronomy, Wayne State University, 2012-2016
Publications:

- V. Tarquini, T. Knighton, Z. Wu, J. Huang, L. Pfeiffer and K. West, "Degeneracy and effective mass in the valence band of two-dimensional (100)-GaAs quantum well systems", Applied Physics Letters, 104, 9 (2014): 092102.
- T. Knighton, V. Tarquini, Z. Wu, J. Huang, L. Pfeiffer and K. West, "Large intrinsic inductance in strongly correlated GaAs two-dimensional holes in the integer quantum hall regime", Applied Physics Letters 104, 19 (2014): 193109.
- T. Knighton, Z. Wu, V. Tarquini, J. Huang, L. Pfeiffer and K. West. "Reentrant insulating phases in the integer quantum Hall regime", Physical Review B 90, 16 (2014): 165117.
- Z. Wu, T. Knighton, V. Tarquini, D. Torres, T. Wang, N. Sapulveda and J. Huang, "Polycrystalline VO2 film characterization by quantum capacitance measurement", Applied Physics Letters, 107, 10 (2015): 104101.
- V. Tarquini, T. Knighton, Z. Wu, J. Huang, L. Pfeiffer and K. West, "Bulk-edge dynamics and quantum Hall effect breakdown", in preparation, 2016